Spring 1-1-2017

Development of Low-Cost Sensing Technologies for Measuring Air Quality

Berkeley Almand-Hunter
University of Colorado at Boulder, berkeleyalmandhunter@gmail.com

Development of Low-Cost Sensing Technologies for Measuring Air Quality

by

Berkeley Blair Almand-Hunter

B.S., Colorado School of Mines, 2007

M.S., Colorado School of Mines, 2010

A thesis submitted to the

Faculty of the Graduate School of the

University of Colorado in partial fulfillment

of the requirements for the degree of

Doctor of Philosophy

Department of Mechanical Engineering

2017

This thesis entitled:
Development of Low-Cost Sensing Technologies for Measuring Air Quality
written by Berkeley Blair Almand-Hunter
has been approved for the Department of Mechanical Engineering

Michael Hannigan

Prof. Shelly Miller

Date

The final copy of this thesis has been examined by the signatories, and we find that both the content and the form meet acceptable presentation standards of scholarly work in the above mentioned discipline.

Almand-Hunter, Berkeley Blair (Ph.D., Mechanical Engineering)

Development of Low-Cost Sensing Technologies for Measuring Air Quality

Thesis directed by Prof. Michael Hannigan

In order to protect human health and the environment, it is necessary to measure ozone concentrations in the atmosphere. State and federal regulatory agencies take continuous measurements of ozone concentrations and fluxes at centralized locations, but current monitoring systems are costly, and the number of sites is limited. The work discussed in this dissertation aims to address this challenge through the development of low-cost instruments that measure ozone flux. We developed low-cost flux chambers that accurately measure ozone dry deposition when paired with 2B ozone monitors. While we concluded that the least expensive sensors available, metal-oxide ozone sensors, are not suitable for use with these chambers, the cost of the chambers in combination with 2B ozone monitors ($7000) is much lower than the cost of eddy covariance measurement systems. Additionally, many research groups already own ozone monitors, which can be attached to a flux chamber, which results in an additional cost of only $2000. Also, a complete overhaul of the models we use to calibrate metal-oxide ozone sensors for use in ambient ozone monitors resulted in a 42% improvement in the prediction of high ozone concentrations. The modeling algorithms developed in this work can be applied to all of the sensors used by our group, which will improve results for a number of studies.

Acknowledgements

I would like to thank the members of my committee (Mike Hannigan, Shelly Miller, John Walker, Daven Henze, and Julie Steinbrenner) for taking the time to read this document and listen to my presentation. I also would like to thank the Electric Power Research Institute (EPRI) and NASA for funding my research. I am grateful to my adviser, Mike Hannigan, for all of his help and support. I'd also like to thank to John Walker for going above and beyond to help me with the validation of my chamber. I would like to thank Corey Miller for his help building the flux chambers. Kateryna Lapina, Peter Hamlington, Nick Clements, Peter Harley, Bill Mitchell, and Andrew Turnipseed participated in helpful discussions. This project would not have been possible without equipment borrowed from Christine Wiedinmyer and John Ortega, as well as Joanna Gordon and Ashley Collier. Ricardo Piedrahita and Nick Massons sensor work is the basis for the inexpensive sensor portion of this project, and they have been very helpful in building boards and interpreting data. I'd like to thank Sharon Anderson and Cassie Drew for always going above and beyond, and handling any administrative problems that arise. I'd like to thank the students in the Hannigan group (Kyle Karber, Nick Masson, Didi Muvandimwe, Evan Coffey, Nick Clements, Ashley Collier, Joanna Gordon, Tiffany Duhl, Lauren Hafford, Mingjie Xie, and Ricardo Piedrahita) for being supportive and fun, and making my work days enjoyable. I'd also like to thank my husband, Andy Almand-Hunter, for being generally wonderful, and also for proofreading this long document.

Contents

Chapter

Tables

Table

Figures

Figure

Chapter 1

Introduction

Exposure to high concentrations of ozone and other air pollutants can cause a variety of negative health effects including lung inflammation, increases in respiratory-system-related hospital visits, cardiopulmonary mortality, and alterations in sleep patterns, neurotransmitters, short and long term memory, and motor activity (EPA, 2013; Lippmann, 1989). To protect human health, state and federal regulatory agencies take continuous measurements of ozone concentrations at centralized locations. However, because current ozone monitoring systems are costly and consume large quantities of power, the number of monitoring sites is limited. Additionally, ozone concentrations can vary spatially, and are often lower in the immediate vicinity of roadways due to reactions with NO (EPA, 2013). Concentrations can also be higher in locations downwind of an urban area than in the urban core, due to ozone‘s formation as a secondary pollutant. These local-scale variations can have a sizable impact on the relative magnitude of ozone concentrations in urban areas, and can lead to error in estimates of personal exposure. Additionally, since the ratio of indoor and outdoor ozone concentrations varies based on air-exchange rate and a number of other factors, and the amount of time individuals spend indoors varies from person to person, ratios between personal exposure and ambient outdoor concentration can vary between 0.1 and 0.9 (EPA, 2013). More accurate measurements of personal exposure can be obtained through the use of monitoring networks with high spatial coverage, as well as portable devices. This scale of measurements has historically been prevented by the cost of monitoring devices.

In addition to the negative impacts of ozone on human health, deposition of ozone places

environmental stress on sensitive vegetated landscapes and aquatic ecosystems (Fangmeier et al., 1994; Williams and Tonnessen, 2000). Examples of this stress include increased susceptibility to injury and decreased growth for sensitive plant species, decreased water quality, toxicity to freshwater organisms, eutrophication, change in greenhouse emissions from soil (Fenn et al., 1998), reduction in biodiversity, and interference with a plants uptake of other important cations, such as potassium (Fangmeier et al., 1994). These negative effects can be particularly pronounced at high altitudes, where buffering capacities can be below average (Benedict et al., 2013; Fenn et al., 1998; Williams and Tonnessen, 2000). Understanding deposition and emission rates is also an important piece of estimating atmospheric concentrations in the planetary boundary layer for climate and weather models. Since it is not possible to measure flux everywhere, improving deposition models is a crucial step in determining accurate transfer ratios. Efforts to improve models are ongoing (Brook et al., 1999; Zhang et al., 2001, 2003); models estimate flux well under some conditions, but fluxes determined by different models and observations can vary by a factor of 2 to 3 (Flechard et al., 2011; Schwede et al., 2011; Wu et al., 2011). Direct dry-deposition measurements are needed to improve and validate models for different ecosystems, and under varied environmental conditions, but the current measurement schemes are cost prohibitive. This work addresses the need for low-cost measurement devices through the development and validation of low-cost dynamic flux chambers, which measure dry deposition, as well as improvement of quantification models for inexpensive metal-oxide ozone sensors.

Chapter 2

Literature Review

Deposition of pollutants, including ozone, nitrogen, and acidic compounds (SO_x, NO_y), places environmental stress on sensitive vegetated landscapes and aquatic ecosystems (Ashmore, 2005; EPA, 2011; Fangmeier et al., 1994; Williams and Tonnessen, 2000). Examples of this stress include increased susceptibility to illness and decreased growth for sensitive plant species (EPA, 2011, 2013), decreased water quality, toxicity to freshwater organisms, eutrophication, increased greenhouse emissions from soil (Fenn et al., 1998), reduction in biodiversity, and interference with a plant's uptake of other important cations, such as potassium (Fangmeier et al., 1994). These negative effects can be particularly pronounced at high altitudes, where buffering capacities can be below average (Fenn et al., 1998; Williams and Tonnessen, 2000).

Dry deposition, which is the process by which pollutants are transported from the atmosphere to the earth's surface without precipitation (Seinfeld and Pandis, 2006), is an important component of atmospheric deposition. This process is estimated to account for up to 50% of total atmospheric deposition in the United States (EPA, 2010; Wesely and Hicks, 2000). Despite this sizable contribution to total atmospheric deposition, there is a lack of direct measurements for dry-deposition in the US. Currently employed direct dry-deposition measurements are not part of the routine measurement suite because they are prohibitively expensive and complex. This results in significant uncertainty in deposition loads, specifically regarding transfer ratios (the relationship between ambient concentrations and total deposition). Given the large spatio-temporal variability in air-surface exchange rates of reactive compounds, there is a need for low-cost, easily deployable

systems to directly measure dry deposition.

There has been significant debate over whether ozone damage to vegetation is best quantified and regulated using ambient concentrations or atmospheric fluxes (EPA, 2013; Musselman et al., 2006). While the use of ambient concentrations is certainly much simpler, fluxes have more physical meaning. Understanding deposition and emission rates is an important piece of estimating atmospheric concentrations in the planetary boundary layer for climate and weather models. Since it is not possible to measure flux everywhere, improving deposition models is a crucial step in determining accurate transfer ratios. Efforts to improve models are ongoing (Brook et al., 1999; Zhang et al., 2001, 2003), and models estimate flux well under some conditions, but agreement between different models and observations can be off by up to 300% (Flechard et al., 2011; Schwede et al., 2011; Wu et al., 2011). Direct dry-deposition measurements are needed to improve and validate models for different ecosystems, and under varied environmental conditions.

Currently, the most common methods for measuring atmospheric fluxes are eddy covariance, the inferential method, and the gradient method (Seinfeld and Pandis, 2006; Turnipseed et al., 2009). Eddy covariance consists of taking high-speed measurements of concentration and three-dimensional wind velocity. The flux is computed from the covariance between the fluctuating components of wind velocity and concentration. This method is the most mathematically robust and accurate way to acquire dry-deposition measurements, but it is expensive and technically difficult compared with indirect-measurement methods (Baldocchi et al., 1988). The gradient method computes flux indirectly by combining vertical-concentration data and gradient-transport theory.

Another method for measuring flux, which is used more frequently to measure emissions than it is to measure deposition, is the flux chamber. Advantages of flux chambers over current methods include reduced cost, the ability to determine spatial variability in deposition, the capability of taking measurements in areas with complex topography and areas with non-uniform vegetation (eddy-covariance typically requires an area of uniform vegetation that is $\geq 100\,\mathrm{m}^2$, mobility, and the potential to be used with inexpensive sensors. The main drawback of using chambers for flux measurements is that they alter the environment in which they are placed. Static chambers, which

are commonly used to measure emissions, significantly affect environmental conditions. Dynamic chambers minimize this problem by operating in a normally open mode, with lids that close for just a few minutes per hour. This keeps the environmental conditions in the chamber very close to ambient (Pape et al., 2008). Another way to minimize the alteration of the ambient environment is to maintain a high air-turnover rate in the chamber. This prevents changes in temperature and humidity in the chamber, which both affect deposition processes. It is also critical to make flux chambers out of highly transparent materials, which enables sunlight to reach the vegetation inside.

In 2008, Pape et al. designed an automatic, dynamic flux chamber, which addressed many of the issues mentioned above. They tested their chambers against an eddy-covariance system at a grassland site, and demonstrated good agreement for CO_2 and methanol deposition (Pape et al., 2008). Our research effort expands on this validation-based flux-chamber development through the creation of an automated, inexpensive, and continuous multiple-species gas-flux monitoring system, which can provide data for a variety of relevant atmospheric pollutants, including O_3, CO_2, and NO_x.

2.0.1 Dry Deposition Theory

Dry deposition flux (F), or the amount of species depositing to a unit surface, is assumed to be proportional to the species' ambient concentration (C) at some reference height (Seinfeld and Pandis, 2006). The proportionality constant between the concentration and flux is called "deposition velocity," (v_d) (Chamberlain and Chadwick, 1953), such that

$$\mathrm{F} = -v_\mathrm{d}\mathrm{C}. \tag{2.1}$$

v_d has a negative direction, since it describes the downward movement of a species. Thus, the minus sign in equation 3.8 cancels out the negative v_d value, which results in a positive flux. The deposition-velocity representation is convenient because of its simplicity. However, since v_d represents many complex chemical and physical processes, its value is difficult to determine (Seinfeld and Pandis, 2006).

The deposition process is described using a resistance analogy (Wesely and Hicks, 2000), in which species transport from the atmosphere to the surface of a material is controlled by three resistances in series.

$$v_{\mathrm{d}} = \frac{1}{r_{\mathrm{t}}} = \frac{1}{r_{\mathrm{a}} + r_{\mathrm{b}} + r_{\mathrm{c}}}, \tag{2.2}$$

where r_{t} is the total resistance to deposition, r_{a} is the resistance to aerodynamic transport, r_{b} is the resistance to diffusion through the quasi-laminar boundary layer, and r_{c} is the resistance to uptake of the trace gas by the canopy. These resistances are shown in 2.1.

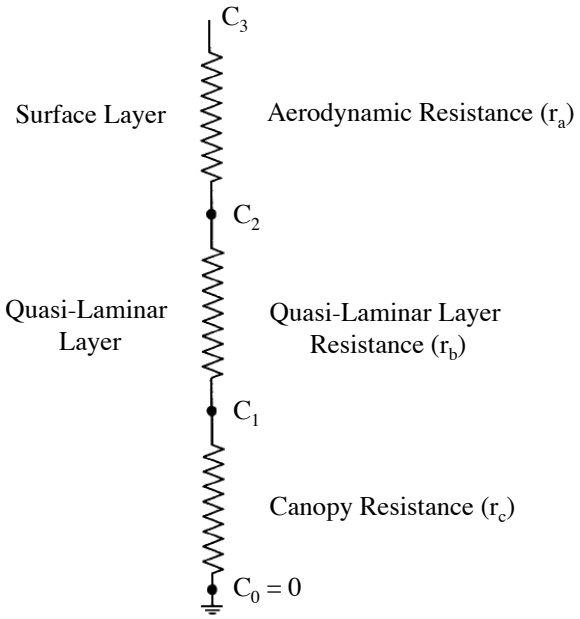

Figure 2.1: Substances encounter three resistances on their way to deposition: aerodynamic resistance, quasi-laminar resistance, and canopy resistance (Seinfeld and Pandis, 2006).

The resistor between C_1 and C_0 in Figure 2.1 represents the resistance offered by the surface. The canopy (surface) resistance is affected by surface type (vegetation, soil, water), ambient meteorological conditions (temperature, humidity, etc.), solar radiation, surface wetness, surface compensation point, and chemical species (Seinfeld and Pandis, 2006).

Theory has been developed to describe dry deposition of both particles and gases to different

surface types (Seinfeld and Pandis, 2006). This literature review will discuss gas-phase deposition to vegetative canopies and soil, since these are the surfaces of concern for our flux chamber.

2.0.1.1 Calculating Aerodynamic Resistance (r_a)

In order to solve Equation 3.9, we need equations for r_a, r_b, and r_c. It is assumed that r_a can be expressed as turbulent eddy diffusivity times trace-gas-concentration gradient. Since eddy diffusivity is not always known, it can be expressed as

$$\zeta = \frac{z}{L}, \tag{2.3}$$

where L is the Monin-Obukhov length and z is the height above the surface. L is related to atmospheric stability, and is found by first determining the Pasquill Stability Class, which can be found in Table 2.1, then calculating L using Table 2.2 and Equation 2.4,

$$\frac{1}{L} = a + b \log z_o. \tag{2.4}$$

Table 2.1: Estimation of Pasquill Stability Classes

Windspeed at 10 m (m/s)	Daytime Strong Solar Radiation	Daytime Moderate Solar Radiation	Nighttime Slight Solar Radiation	Nighttime Cloud Cover Fraction $\leq 4/8$	Cloud Cover Fraction $\leq 3/8$
< 2	A	A-B	B	-	-
2-3	A-B	B	C	E	F
3-5	B	B-C	C	D	E
5-6	C	C-D	D	D	D
> 6	C	D	D	D	D

Key: A-extremely unstable, B-moderately unstable, C-slightly unstable, D-neutral, E-slightly stable, F-moderately stable. Strong solar radiation is defined as more than 700 $W\,m^{-2}$, moderate solar radiation is 350-700 $W\,m^{-2}$, and slight solar radiation is less than 350 $W\,m^{-2}$ (Turner, 1969).

Table 2.2: Correlation Parameters for the Estimation of L (Seinfeld and Pandis, 2006)

Pasquill Stability Class	a	b
A (extremely unstable)	-0.096	0.029
B (moderately unstable)	-0.037	0.029
C (slightly unstable)	-0.002	0.018
D (neutral)	0	0
E (slightly stable)	0.004	-0.018
F (moderately stable)	0.035	-0.036

The dimensionless temperature profile is given by Equation 2.5.

$$\Phi_{\mathrm{T}}(\zeta) = \begin{cases} 1 + 4.7\zeta & \text{for} \quad 0 < \zeta < 1 \quad \text{(stable)} \\ 1 & \text{for} \quad \zeta = 0 \quad \text{(neutral)} \\ (1 - 15\zeta)^{-\frac{1}{4}} & \text{for} \quad -1 < \zeta < 0 \quad \text{(unstable)} \end{cases} \tag{2.5}$$

and the aerodynamic resistance is

$$r_{\mathrm{a}} = \begin{cases} \frac{1}{\kappa u_*}[\ln(\frac{z}{z_{\mathrm{o}}}) + 4.7(\zeta - \zeta_0)] & \text{(stable)} \\ \frac{1}{\kappa u_*}\ln(\frac{z}{z_{\mathrm{o}}}) & \text{(neutral)} \\ \frac{1}{\kappa u_*}[\ln(\frac{z}{z_{\mathrm{o}}}) + \ln(\frac{(\zeta_o^2+1)(\zeta_0+1)^2}{(\zeta_r^2+1)(\zeta_r+1)^2})] & \text{(unstable),} \end{cases} \tag{2.6}$$

where

$$\eta_0 = (1 - 15\zeta_0)^{\frac{1}{4}}, \tag{2.7}$$

$$\eta_r = (1 - 15\zeta_r)^{\frac{1}{4}}, \tag{2.8}$$

and

$$\zeta_0 = \frac{z_0}{L}. \tag{2.9}$$

This theory is only applicable to a maximum vertical height of ≈100m, in the surface layer, where the flux is non-divergent (Seinfeld and Pandis, 2006).

2.0.1.2 Calculating Quasi-Laminar Boundary Layer Resistance ($\mathbf{r_b}$)

Gas-phase transport through the quasi-laminar layer is governed by the molecular diffusivity of the gas through the air. This is represented by the Schmidt number,

$$\mathrm{Sc} = \frac{\nu}{D}, \tag{2.10}$$

where ν is the kinematic viscosity of air and D is the molecular diffusivity of the depositing species.

Resistance to transport in the quasi-laminar layer can be determined, using the Schmidt number, as

$$r_b = \frac{5\ \mathrm{Sc}^{\frac{2}{3}}}{u_*}, \tag{2.11}$$

where u_* is friction velocity (see Table 2.3).

2.0.1.3 Calculating Canopy Resistance ($\mathbf{r_c}$)

The canopy resistance (r_c), or surface resistance, is the most complicated and difficult to calculate of the three resistances to dry deposition. Depending on the type of surface, r_c is represented by either water resistance (r_cw), ground resistance (r_cg), or foliar resistance (r_cf). Figure 2.2 illustrates the breakdown of the canopy resistance by surface (Seinfeld and Pandis, 2006).

If deposition occurs over a forest or plant canopy,

$$\frac{1}{r_\mathrm{c}} = \frac{1}{r_\mathrm{cf}} + \frac{1}{r_\mathrm{cg}}, \tag{2.12}$$

or, if it occurs over a wet vegetated surface,

$$\frac{1}{r_\mathrm{c}} = \frac{1}{r_\mathrm{cf}} + \frac{1}{r_\mathrm{cw}}. \tag{2.13}$$

The foliar resistance (r_cf) comprises two pathways. The first is uptake via the cuticular (epidermal) surfaces (r_cut), and the other is via the plant's stomata (r_st).

Table 2.3: Friction Velocity (u_*) estimates based on land-use categories (Zhang et al., 2003).

	Land-Use Category	Day Dry or Rain	Night Dry or Rain	Night Dew	Day Snow
1	water	0.3	0.25	0.2	0.3
2	ice	0.25	0.15	0.15	0.25
3	inland lake	0.25	0.2	0.2	0.25
4	evergreen needleleaf trees	0.6	0.3	0.2	0.45
5	evergreen broadleaf trees	0.7	0.35	0.2	0.5
6	deciduous needleleaf trees	0.6	0.3	0.2	0.45
7	deciduous broadleaf trees	0.6	0.3	0.2	0.45
8	tropical broadleaf trees	0.7	0.35	0.2	0.5
9	drought deciduous trees	0.6	0.3	0.2	0.45
10	evergreen broadleaf shrubs	0.4	0.2	0.2	0.3
11	deciduous shrubs	0.4	0.2	0.2	0.3
12	thorn shrubs	0.4	0.2	0.2	0.3
13	short grass and forbs	0.4	0.2	0.2	0.3
14	long grass	0.4	0.2	0.2	0.3
15	crops	0.4	0.2	0.2	0.3
16	rice	0.4	0.2	0.2	0.3
17	sugar	0.4	0.2	0.2	0.3
18	maize	0.4	0.2	0.2	0.3
19	cotton	0.4	0.2	0.2	0.3
20	irrigated crops	0.4	0.2	0.2	0.3
21	urban	0.6	0.3	0.2	0.45
22	tundra	0.25	0.15	0.15	0.25
23	swamp	0.4	0.2	0.2	0.3
24	desert	0.25	0.15	0.15	0.25
25	mixed-wood forests	0.6	0.3	0.2	0.45
26	transitional forest	0.6	0.3	0.2	0.45

$$r_{\mathrm{cf}} = \left(\frac{1}{r_{\mathrm{cut}}} + \frac{1}{r_{\mathrm{st}}} \right)^{-1} (LAI)^{-1}, \tag{2.14}$$

where LAI is leaf-area index, which is the ratio of the total leaf-surface area to the area of the ground. Incorporating LAI into the equation adjusts the proper magnitude of r_{cf} in relation to r_{cg} or r_{cw}. LAI varies throughout the year for some land-use categories (LUC), and Figure 2.3 displays the monthly LAI for each category. LAI values for LUCs with constant values can be found in Table 2.4.

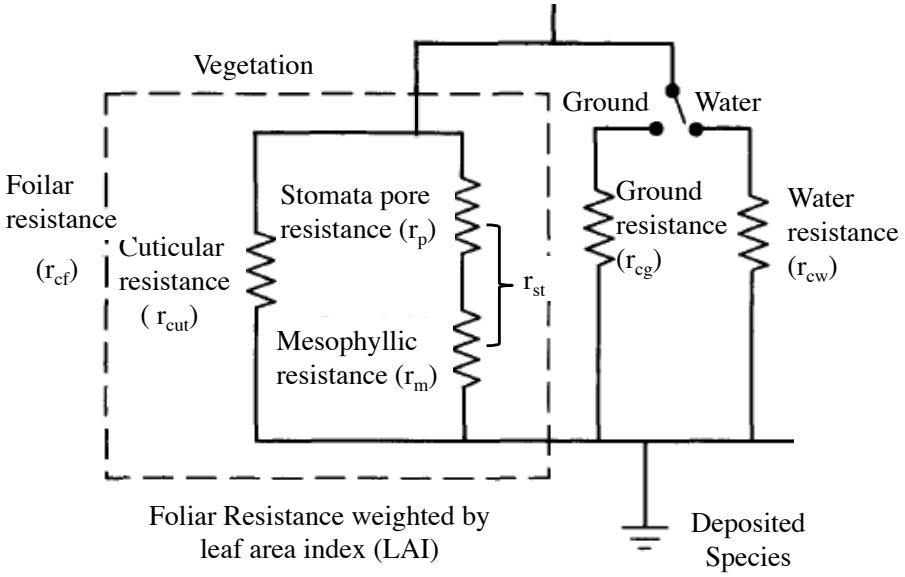

Figure 2.2: Depending on the type of surface, canopy resistance (r_c) is represented by either water resistance (r_{cw}), ground resistance (r_{cg}), or foliar resistance (r_{cf}) (Seinfeld and Pandis, 2006).

Theory for the surface resistance for dry deposition of gases to water is available (Seinfeld and Pandis, 2006), but will not be discussed in this literature review.

2.0.1.4 Improvements to Canopy Resistance

The theory in the previous section has been accepted for decades, and is summarized in review papers and textbooks (Seinfeld and Pandis, 2006; Wesely and Hicks, 2000). More recently, model improvements have been proposed, particularly for non-stomatal resistance (Zhang et al., 2003). The theory discussed in this section is based on the work of L. Zhang and coworkers (Zhang et al., 2001, 2003)).

Non-stomatal resistance (r_{ns}) includes any resistance to uptake that is not related to stomata. This includes cuticular, soil, and in-canopy aerodynamic resistances. Zhang et al. (2003) characterized non-stomatal resistance by studying the deposition of O_3 and SO_2 over 5 vegetation types, and scaling the results to predict the behavior of other chemical species based on their physical and chemical characteristics. Relative humidity (RH), leaf-area index (LAI), friction velocity, and

Table 2.4: Leaf-Area Index (LAI) estimates based on land-use categories (Zhang et al., 2003).

Land-Use Category	LAI
4	5.0
5,8	6.0
9,23	4.0
10,12	3.0
13	1.0
1-3,22,24	0.0

canopy wetness are input parameters to the model.

Canopy resistance is defined as

$$\frac{1}{r_{\mathrm{c}}} = \frac{1 - W_{\mathrm{st}}}{r_{\mathrm{st}} + r_{\mathrm{m}}} + \frac{1}{r_{\mathrm{ns}}}, \tag{2.15}$$

where W_{st} is the stomatal blocking fraction under wet conditions, and r_{m} is mesophyllic resistance, which Zhang and coworkers treat as dependent only on species (Zhang et al., 2002, 2003). r_{m} is assumed to be 0 for both NO_2 and O_3. W_{st} is zero in dry conditions. For wet canopies,

$$W_{st} = \begin{cases} 0 & SR <= 200 \text{ W/m}^2 \\ (SR - 200)/800 & 200 < SR <= 600 \text{ W/m}^2 \\ 0 & \text{SR} > 600 \text{ W/m}^2, \end{cases} \tag{2.16}$$

where SR is solar radiation. The stomatal resistance (r_{st}) is found using the equation,

$$r_{\mathrm{st}} = \frac{1}{G_{\mathrm{s}}(PAR) f(T) f(D) f(\psi) D_i / D_\nu}, \tag{2.17}$$

where $G_{\mathrm{s}}(PAR)$ is the unstressed leaf-stomatal conductance, D_i/D_ν is the ratio of the molecular diffusivity of water to the depositing gas, and $f(T)$, $f(D)$, and $f(\psi)$ are the conductance-reducing effects of air temperature (T), water-vapor deficit (D), and water stress (ψ) on stomatal conductance, respectively.

D_i/D_ν values can be found in 2.5.

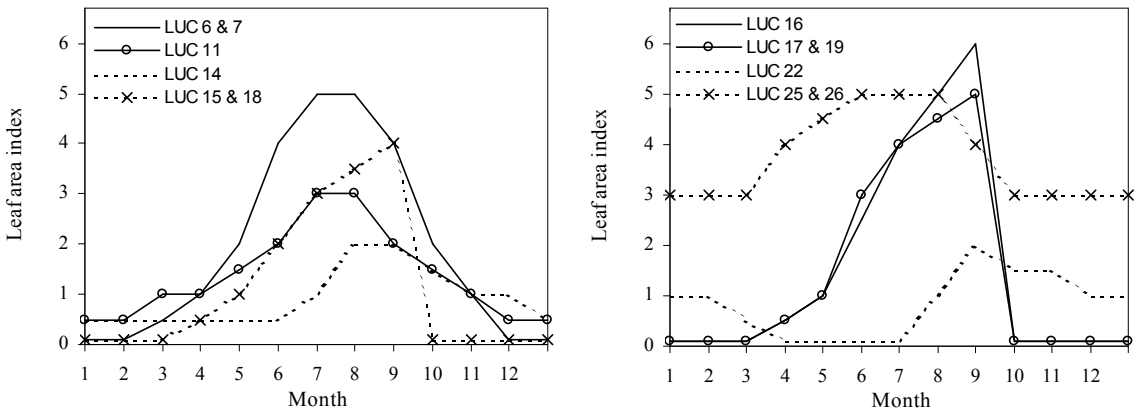

Figure 2.3: Leaf-Area Index (LAI) estimates based on land-use categories. *Source:* Zhang et al. (2003).

Table 2.5: D_i/D_ν for various gases

Species	D_i/D_ν
sulfur dioxide	1.89
ozone	1.63
nitrogen dioxide	1.6
nitric oxide	1.29
nitric acid	1.87
hydrogen peroxide	1.37
acetaldehyde	1.56
propionaldehyde	1.8
formaldehyde	1.29
methyl hydroperoxide	1.6
formic acid	1.6
acetic acid	1.83
ammonia	0.97
petrozyacetyl nitrate	2.59
nitrous acid	1.62
pernitric acid	2.09
hydrochloric acid	1.42

Source: Seinfeld and Pandis (2006)

$$f(T) = \frac{T - T_{\min}}{T_{\text{opt}} - T_{\min}} \left[\frac{T_{\max} - T}{T_{\max} - T_{\text{opt}}} \right]^{b_t}, \tag{2.18}$$

where T is air temperature, $T_{\max}$ and $T_{\min}$ are the temperatures, in °C, above and below

which complete stomatal closure occurs, and T_{opt} is the temperature corresponding to maximum stomatal opening (seeTable 2.6). The term, b_{t}, is defined as

$$b_{\text{t}} = \frac{T_{\text{max}} - T_{\text{opt}}}{T_{\text{opt}} - T_{\text{min}}}. \tag{2.19}$$

$$f(D) = 1 - b_{\text{vpd}} D_{\text{vap}}, \tag{2.20}$$

where b_{vpd} is the water-vapor-pressure-deficit constant in $\text{k}\,\text{Pa}^{-1}$ (see Table 2.6), and D_{vap} is the vapor pressure deficit in kPa.

$$D_{\text{vap}} = e^*(T) - e, \tag{2.21}$$

where $e^*(T)$ is the saturation water-vapor pressure (kPA) at the ambient air temperature (°C) and e is the ambient water vapor pressure in kPa.

$$e^* = 1013.25 e^{13.3185a - 1.97a^2 - 0.6445a^3 - 0.1299a^4}, \tag{2.22}$$

where

$$a = 1 - \frac{373.15}{T}, \tag{2.23}$$

and T is temperature in Kelvins.

$$f(\psi) = \frac{\psi - \psi_{\text{C}_2}}{\psi_{\text{C}_1} - \psi_{\text{C}_2}}, \tag{2.24}$$

where ψ_{C_1} and ψ_{C_2} are parameters that specify leaf-water-potential dependency in MPa (see Table 2.6), and ψ is defined as

$$\psi = -0.72 - 0.0013\, SR, \tag{2.25}$$

where SR is solar radiation. Non-stomatal resistance (r_{ns}) is defined as

$$\frac{1}{r_{\text{ns}}} = \frac{1}{r_{\text{ac}} + r_{\text{cg}}} + \frac{1}{r_{\text{cut}}}, \tag{2.26}$$

where r_{ac} is the in-canopy aerodynamic resistance, r_{cg} is the ground resistance, and r_{cut} is the cuticular resistance. r_{cg} can represent deposition onto surfaces covered with ice (r_{ice}), snow (r_{snow}), soil (r_{soil}), or water (r_{cw}).

For SO_2, the snow, ice, and water resistances are defined as

$$r_{\text{snow,ice SO}_2} = 70(2 - T), \tag{2.27}$$

and

$$r_{\text{water SO}_2} = 20. \tag{2.28}$$

r_{soil} can be broken down into resistance to deposition onto dry soil (r_{gd}) (Table 2.6), soil that has been wetted by rain (r_{grain}), and soil that has been wetted by dew (r_{gdew}).

For O_3, the snow, ice, and water resistances are defined as

$$r_{\text{snow,ice,water O}_3} = 2000. \tag{2.29}$$

The soil resistance for O_3 deposition to vegetated surfaces is defined as

$$r_{\text{soil O}_3} = 200, \tag{2.30}$$

and for non-vegetated surfaces,

$$r_{\text{soil O}_3} = 500. \tag{2.31}$$

When the ambient temperature is below -1°C,

$$r_{\text{gd,winter}} = r_{\text{gd}} e^{0.2(-1-T)}, \tag{2.32}$$

where $r_{\mathrm{gd,winter}}$ is the adjusted soil resistance when T < -1°C. The cuticular resistance ($r_{\mathrm{cut,dry}}$) in dry conditions is defined as

$$r_{\mathrm{cut,dry}} = \frac{r_{\mathrm{cutd0}}}{e^{0.03RH} LAI^{(1/4)} u^*}, \tag{2.33}$$

where r_{cutd0} can be found in Table 2.6, u^* is friction velocity, and LAI is leaf-area index.

Cuticular resistance in wet conditions $r_{\mathrm{cut,wet}}$ is defined as

$$r_{\mathrm{cut,wet}} = \frac{r_{\mathrm{cutw0}}}{LAI^{(1/2)} u^*}, \tag{2.34}$$

where r_{cutw0} is 100 $\mathrm{s\,m^{-1}}$ for dewy conditions and 50 $\mathrm{s\,m^{-1}}$ for rainy conditions. This model does not work well when $u^* > 2$ m/s.

When the ambient temperature is below -1°C,

$$r_{\mathrm{cut,winter}} = r_{\mathrm{cut}} e^{0.2(-1-T)}, \tag{2.35}$$

where $r_{\mathrm{cut,winter}}$ is the adjusted cuticular resistance when T < -1°C.

When snow is on the ground, the soil and cuticular resistances are modified as

$$\frac{1}{r_{\mathrm{g,snow}}} = \frac{1 - 2f_{\mathrm{snow}}}{r_{\mathrm{g}}} + \frac{2f_{\mathrm{snow}}}{r_{snow}} \tag{2.36}$$

and

$$\frac{1}{r_{\mathrm{cut,snow}}} = \frac{1 - f_{\mathrm{snow}}}{r_{\mathrm{cut}}} + \frac{f_{\mathrm{snow}}}{r_{snow}}, \tag{2.37}$$

where $2f_{\mathrm{snow}}$ is the fraction of soil covered in snow, f_{snow} is the fraction of leaves covered in snow, $\mathrm{r_{g,snow}}$ is the modified soil resistance for snow cover, and $\mathrm{r_{cut,snow}}$ is the modified cuticular resistance for snow cover.

$$f_{\mathrm{snow}} = \frac{sd}{sd_{\mathrm{max}}} \tag{2.38}$$

where sd is the snow depth in cm and $sd_{\max}$ is the snow depth at which all leaves are covered with snow ($f = 1$).

The in-canopy aerodynamic resistance is a function of friction velocity (u_*), leaf-area index (LAI), and a reference value for in-canopy aerodynamic resistance (r_{ac0}), which depends on plant species and seasonal variation in leaf coverage.

$$r_{\mathrm{ac}} = \frac{r_{\mathrm{ac0}} LAI^{1/4}}{u_*^2}, \tag{2.39}$$

and

$$r_{\mathrm{ac0}}(t) = r_{\mathrm{ac0}}(\min) + [r_{\mathrm{ac0}}(\max) - r_{\mathrm{ac0}}(\min)] \frac{LAI(t) - LAI(\min)}{LAI(\max) - LAI(\min)}, \tag{2.40}$$

where $r_{\mathrm{ac0}}(\min)$ and $r_{\mathrm{ac0}}(\max)$ correspond to periods of minimum ($LAI(\min)$) and maximum ($LAI(\max)$) leaf coverage, respectively, and can be found in Table 2.6.

Typically, a roughness length (z_0) can be assumed for each land-use category (LUC), and values are listed in Table 2.6. Some categories have a constant roughness length, and others have a listed range. For those with a range, z_0 is

$$z_0(t) = z_0(\min) + [z_0(\max) - z_0(\min)] \frac{LAI(t) - LAI(\min)}{LAI(\max) - LAI(\min)}, \tag{2.41}$$

where $z_0(t)$ is roughness length at a given time, $z_0(\max)$ is the maximum roughness length, and $z_0(\min)$ is the minimum roughness length.

Zhang et al. (2003) evaluated the equations mentioned above, and found that the new model provides more realistic deposition velocities for O_3 deposition.

2.0.2 Previous Chamber Work

Many research groups have conducted experiments using static and dynamic flux chambers. The main drawback of using any chambers for flux measurements, is that they can alter the environment in which they are placed. Static chambers, which have been used extensively in soil flux

Table 2.6: Land-Use Categories and Related Parameters

LUC		R_{ac0}	R_{cutd0} O_3	R_{cutw0} O_3	R_{cutd0} SO_2	R_{gd} SO_2	R_{stmin} (sm^{-1})	b_{rs} (W m^{-2})	T_{min} $(^\circ C)$	T_{max} $(^\circ C)$	T_{opt} $(^\circ C)$	b_{vpd} (kPA^{-1})	ψ_{c1} (MPa)	ψ_{c2} (MPa)	z_0 (m)	Sd_{max} (cm)
1	water	0	n/a	n/a	n/a	20	n/a	n/a	n/a	n/a	n/a	n/a	n/a	n/a	f(u)	n/a
2	ice	0	n/a	n/a	n/a	Equation 2.27	n/a	n/a	n/a	n/a	n/a	n/a	n/a	n/a	0.01	1
3	inland lake	0	n/a	n/a	n/a	20	n/a	n/a	n/a	n/a	n/a	n/a	n/a	n/a	f(u)	n/a
4	evergreen needleleaf trees	100	4000	200	2000	200	250	44	-5	40	15	0.31	-2	-2.5	0.9	200
5	evergreen broadleaf trees	250	6000	400	2500	100	150	40	0	45	30	0.27	-1	-5	2	400
6	deciduous needleleaf trees	60-100	4000	200	2000	200	250	44	-5	40	15	0.31	-2	-2.5	0.4-0.9	200
7	deciduous broadleaf trees	100-250	6000	400	2500	200	150	43	0	45	27	0.36	-1.9	-2.5	0.4-1.0	200
8	tropical broadleaf trees	300	6000	400	2500	100	150	40	0	45	30	0.27	-1	-5	2.5	400
9	drought deciduous trees	100	8000	400	6000	300	250	44	0	45	25	0.31	-1	-4	0.6	200
10	evergreen broadleaf shrubs	60	6000	400	2000	200	150	40	0	45	30	0.27	-2	-4	0.2	50
11	deciduous shrubs	20-60	5000	300	2000	200	150	44	-5	40	15	0.27	-2	-4	0.05-0.2	50
12	thorn shrubs	40	5000	300	2000	200	250	44	0	45	25	0.27	-2	-3.5	0.2	50
13	short grass and forbs	20	4000	200	1000	200	150	50	5	40	30	0	-1.5	-2.5	0.04	5
14	long grass	10-40	4000	200	1000	200	100	20	5	45	25	0	-1.5	-2.5	0.02-0.1	20
15	crops	10-40	4000	200	1500	200	120	40	5	45	27	0	-1.5	-2.5	0.02-0.1	10
16	rice	10-40	4000	200	1500	50	120	40	5	45	27	0	-1.5	-2.5	0.02-0.1	10
17	sugar	10-40	4000	200	2000	200	120	50	5	45	25	0	-1.5	-2.5	0.02-0.1	10
18	maize	10-50	5000	300	2000	200	250	65	5	45	25	0	-1.5	-2.5	0.02-0.1	10
19	cotton	10-40	5000	300	2000	200	125	65	10	45	30	0	-1.5	-2.5	0.02-0.2	10
20	irrigated crops	20	4000	200	2000	50	150	40	5	45	25	0	-1.5	-2.5	0.05	10
21	urban	40	6000	400	4000	300	200	42	0	45	22	0.31	1.5	3	1.0	50
22	tundra	0	8000	400	2000	300	150	25	5	40	20	0.24	0	1.5	0.03	2
23	swamp	20	5000	300	1500	50	150	40	0	45	20	0.27	1.5	2.5	0.1	10
24	desert	0	n/a	n/a	n/a	700	n/a	n/a	n/a	n/a	n/a	n/a	n/a	n/a	0.04	2
25	mixed wood forests	100	4000	200	2500	200	150	44	3	42	21	0.34	2	2.5	0.60.9	200
26	transitional forest	100	4000	200	2500	200	150	43	0	45	25	0.31	2	3	0.60.9	200

measurements, can cause large increases in temperature and humidity, and decrease or completely block solar radiation.

Dynamic flux chambers minimize these environmental changes by pumping ambient air through the chamber. Table 3.1 lists previous flux-chamber measurements of NO, NO_2, CO_2, and O_3. One type of flux chamber listed in Table 3.1 is the leaf-scale dynamic chamber, which is used to measure fluxes to and from individual leaves and branches (Altimir et al., 2002; Breuninger et al., 2012a,b; Gessler et al., 2000; Sparks et al., 2001). While leaf-scale deposition measurements are important for understanding leaf dynamics, they can be difficult to scale to the canopy scale, and do not directly represent ecosystem-level flux.

Another type of chamber listed in Table 3.1, is the dynamic soil-flux chamber (Butterbach-Bahl et al., 1997; Norman et al., 1997; Remde et al., 1993). A significant portion of the chambers listed did not have open tops, and the soil or vegetation in the chamber was only exposed to ambient conditions via air pumped into the chamber. These chambers, which are not normally open to the ambient environment, have significant drawbacks. They all block a fraction of incoming solar radiation, and in order to maintain ambient conditions, they have to be moved frequently, which makes long-term or remote deployments difficult.

Several research groups have addressed these issues by developing chambers with lids that open and close automatically](Kitzler et al., 2006; Meixner et al., 1997; Pape et al., 2008). These automatic chambers operate in a normally open mode, with lids that close for just a few minutes per hour. Provided that the chambers are made out of highly transparent materials, so sunlight can reach the vegetation inside, the environmental conditions in the chamber remain very close to ambient (Pape et al., 2008).

While many chamber measurements have been made (Table 3.1), very few of these studies compare NO, O_3, and CO_2 fluxes measured by chambers to measurements acquired via micrometeorological techniques. Several groups have compared chamber measurements of NO fluxes from soils to gradient measurements (Kaplan et al., 1988; Parrish et al., 1987; Stella et al., 2012)). Norman et al. (1997) compared several types of static and dynamic chambers with each other and

eddy correlation for measuring CO_2 fluxes in forest soils, but only two data points for eddy correlation were available for comparison, each representing one day. Li et al. (1999) compared chamber measurements of NO fluxes from agricultural soils with eddy-correlation measurements, and found that the fluxes measured by the chambers were higher than the eddy-correlation measurements, but followed a similar diurnal trend. Pape et al. (2008) compared an automatic, dynamic flux chamber with an eddy-covariance system at a grassland site, and demonstrated good agreement for CO_2 deposition. Due to the fact that these comparison studies are limited in number, and sometimes did not yield good agreement between methods, further comparisons of flux chambers and micrometeorological methods are warranted.

Pape et al. (2008) used measurements of mixing ratios and flow rate, in combination with a mass balance equation, to determine flux. They began with the general equation,

$$V\rho_{\mathrm{d}}\frac{\mathrm{d}\mu_{\mathrm{cham}}}{\mathrm{dt}} = AF_{\mathrm{cham}} - Q\rho_{\mathrm{d}}(\mu_{\mathrm{cham}} - \mu_{\mathrm{amb}}), \tag{2.42}$$

where V is the chamber volume, ρ_{d} is the density of the air molecules, A is the soil surface-area enclosed by the chamber, F_{cham} is the flux of an inert gas, Q is the chamber flow rate, t is time, and μ_{cham} and μ_{amb} are the trace-gas-mixing ratios for the air leaving the chamber, and the ambient air, respectively. Under steady state conditions, Equation 3.5 can be reduced to

$$F_{\mathrm{cham}} = \rho_{\mathrm{d}}\frac{Q}{A}(\mu_{\mathrm{cham}} - \mu_{\mathrm{amb}}). \tag{2.43}$$

Equations 3.5 and 2.43 are based on the assumption that the chamber is well mixed. The authors ensured good mixing by placing mixing fans inside their chamber.

Pape and coworkers point out that the flux chamber will inevitably alter the ambient aerodynamic transport of trace gases to the ground and vegetation. The trace gas flux in ambient conditions can be written as

$$F_{\mathrm{amb}} = \frac{\rho_{\mathrm{d}}(\mu_{\mathrm{comp}} - \mu_{\mathrm{amb}})}{r_{\mathrm{a}} + r_{\mathrm{b}} + r_{\mathrm{c}}}, \tag{2.44}$$

Table 2.7: Summary of Selected Chamber Measurements of NO_2, NO, O_3, and CO_2

Reference	Gases Measured	Surface	Chamber Type	Validation Method
Aeschlimann et al. (2005)	CO_2	grassland	dynamic	none
Altimir et al. (2002)	CO_2, O_3	Scots Pine Shoots	dynamic, shoot chamber	compared w/ typical O_3 flux values
Aneja et al. (1995)	NO_2, NO	Agricultural Soil	dynamic	none
Breuninger et al. (2012b)	NO_2, NO, CO_2, O_3	Norway Spruce	dynamic, branch chamber	none
Breuninger et al. (2012a)	NO_2, NO, CO_2, O_3	Norway Spruce	dynamic, branch chamber	none
Burkart et al. (2007)	CO_2	barley, sugar beet, wheat	dynamic	destructive harvest
Butterbach-Bahl et al. (1997)	NO_2, NO, O_3	forest soil	dynamic, automated lids	none
Garcia et al. (1990)	CO_2	soybeans	dynamic	none
Gessler et al. (2000)	NO_2, CO_2, NH_3	beech saplings and twigs	dynamic	none
Gut et al. (1999)	NO	wheat	dynamic	model comparison
Gut et al. (2002)	NO_2, NO, CO_2, O_3	soil	dynamic	model comparison (using ambient concentration)
Horváth et al. (2006)	NO, O_3	spruce and oak soil	dynamic	none
Kaplan et al. (1988)	NO	forest soil	dynamic	compared well with nighttime vertical profile
Kirkman et al. (2002)	NO_2, NO, O_3	pasture	dynamic	none
Kitzler et al. (2006)	NO_2, CO_2	forest soil	dynamic, automated lid	none
Laville et al. (2011)	NO, CO_2	agricultural soil	dynamic, automated lid	none
Li et al. (1999)	NO	agricultural soil	dynamic	chamber values larger than eddy-covariance, but varied similarly with time
Machon et al. (2010)	NO	grassland	dynamic	compared with model
Maljanen et al. (2007)	NO	dung and urine patches on soil	dynamic	none
Meixner et al. (1997)	NO, NO_2, O_3	grassland & crops	dynamic, automated lid	none
Norman et al. (1997)	CO_2	forest soil	dynamic & static	compared 5 types of chambers and 2 eddy-covariance data points
Pape et al. (2008)	NO_2, NO, CO_2, O_3	grassland	dynamic, automatic lid	very good agreement w/ eddy covariance for CO_2 (did not compare NO, NO_2, & O_3)
Parrish et al. (1987)	NO	grassland	dynamic	nighttime comparison with gradient method
Pilegaard et al. (1999)	NO, CO_2	forest soil	dynamic	none
Pilegaard (2001)	NO, NO_2, O_3	forest soil	dynamic, automated lid	none
Remde et al. (1993)	NO, NO_2, O_3	marsh soil	dynamic	none
Roelle et al. (1999)	NO, NO_2	corn soil	dynamic	none
Roelle et al. (2001)	NO	agricultural soils	dynamic	none
Skiba et al. (1993)	NO	ryegrass	dynamic	none
Slemr and Seiler (1984)	NO, NO_2	grassland soil	dynamic	none
Sparks et al. (2001)	NO_2	25 leaf species	dynamic leaf chamber	none
Stella et al. (2012)	NO	agricultural soil	dynamic, automated lid	agreed with gradient method for low fluxes, but underestimated high fluxes
Unsworth et al. (1984)	O_3	soybeans	dynamic, open top	canopy resistances comparable to other field studies
Dijk and Duyzer (1999)	NO	forest soil	dynamic	none
Williams and Davidson (1993)	NO	grassland	dynamic	comparison of 2 chamber types
Yamulki et al. (1995)	NO	agricultural soil	dynamic	none

where r_a, r_b, and r_c are the turbulent resistance, quasi-laminar boundary-layer resistance, and surface resistance to gas deposition, respectively. F_{amb} is the true trace gas flux in ambient conditions, and μ_{comp} is the mixing ratio of the trace gas at the compensation point (concentration at the low end of the resistance chain, such as inside the soil or plant leaf) (Pape et al., 2008).

The flux chamber modifies these resistances, with the change in r_a (aerodynamic resistance) being the most significant. Aeschlimann et al. (2005) imitated the diurnal variations in ambient r_a by using a slower chamber-purging flow rate at night than during the day. In the modified flux equation, r_a is replaced by two resistances in series. The first is the purging resistance (r_{purge}) between chamber and ambient air. The second is the mixing resistance (r_{mix}), which represents the turbulent mixing inside the chamber. If the chamber air is well mixed, r_{mix} is very small in comparison with r_{purge}, and can be neglected. r_b, the boundary layer resistance, is also altered by the chamber, and Pape refers to the modified boundary layer resistance as r_b^* (Pape et al., 2008).

For a well-designed chamber that maintains near-ambient conditions, r_c (canopy resistance) and μ_{comp} (compensation point mixing ratio) inside the chamber should be very close to ambient. Combining the chamber resistances and Equation 2.44 yields

$$\frac{F_{cham}}{F_{amb}} = \frac{r_a + r_b + r_c}{r_{purge}} + r_b^* + r_c, \tag{2.45}$$

where

$$r_{purge} = \frac{A}{Q} \tag{2.46}$$

and

$$r_b^*(LAI) = \frac{r_b^*}{1 + LAI}. \tag{2.47}$$

For trace gases with zero compensation points, such as ozone,

$$r_b^*(LAI) = \frac{r_{purge}}{\frac{\mu_{amb}(O_3)}{\mu_{cham}(O_3)} - 1} - r_c(O_3). \tag{2.48}$$

In order to use Equation 2.48, the value of $r_c(O_3)$ must be known, which is typically not the case. However, under optimal conditions for stomatal uptake (high LAI and solar radiation), $r_c(O_3)$ should approach its minimum value (Pape et al. (2008)), which has been reported to be about 100 $s\,m^{-3}$ (Wesely and Hicks (2000)).

It is important to consider photochemical reactions in flux chambers (Meixner et al. (1997); (Pape et al., 2008)). A reaction that likely occurs in the chamber is the photolysis of NO_2. The primary reactions that occur between NO, NO_2, and O_3 are

$$NO + O_3 \rightarrow NO_2 + O_2 \tag{2.49}$$

and

$$NO_2 + h\nu \xrightarrow{O_2} NO + O_3, \lambda < 420\text{nm}. \tag{2.50}$$

Because of the relationships between NO, NO_2 and O_3 displayed in reactions 3.11 and 3.12, they must all be measured simultaneously, even if only one is of concern. Reactions 3.11 and 3.12 have the following kinetics:

$$\frac{d\mu(NO)}{dt} = -k\,\mu(NO)\,\mu(O_3) \tag{2.51}$$

$$\frac{d\mu(NO)}{dt} = j(NO_2)\,\mu(NO_2), \tag{2.52}$$

where k is the first-order rate constant of Equation 3.11, and $j(NO_2)$ is the photolysis rate of NO_2. Pape et al. (2008) found that the average value of $j(NO_2)$ inside their flux chambers was 48% of the value outside their chambers. The net source (S_{gp}) of gas-phase NO resulting from reactions 3.11 and 3.12 within the chamber, is

$$S_{gp}(NO) = V[j(NO_2)\,\mu_{cham}(NO_2) - k\,\mu_{cham}(NO)\,\mu_{cham}(O_3)]. \tag{2.53}$$

The reaction kinetics for NO_2 and O_3 are equal or inversely proportional to the reaction kinetics for NO, such that

$$S_{\mathrm{gp}}(\mathrm{NO}) = S_{\mathrm{gp}}(\mathrm{O_3}) = -S_{\mathrm{gp}}(\mathrm{NO_2}). \tag{2.54}$$

Combining these reaction sources or sinks with the mass balance from Equations 3.5 and 2.43 yields

$$V\rho_{\mathrm{d}}\frac{\mathrm{d}\mu_{\mathrm{cham}}}{\mathrm{dt}} = AF_{\mathrm{cham}} - Q\rho_{\mathrm{d}}(\mu_{\mathrm{cham}} - \mu_{\mathrm{amb}}) + S_{\mathrm{gp}} \tag{2.55}$$

and

$$F_{\mathrm{cham}} = \rho_{\mathrm{d}}\frac{Q}{A}(\mu_{\mathrm{cham}} - \mu_{\mathrm{rf:amb}}) - \frac{1}{A}S_{\mathrm{gp}}. \tag{2.56}$$

2.0.3 Spatial Variability

Dry deposition flux varies spatially, due to both trace-gas concentration and deposition velocity, and regional models must accurately predict both of these variables in order to accurately estimate atmospheric fluxes. Emberson et al. (2000) evaluated different methods of estimating ozone damage to vegetation. They estimated dry-deposition flux to vegetation in Europe using a stomatal-conductance-based model, then based damage estimates on their calculated flux. They compared their estimates of damage with those estimated using a concentration-based exposure metric, which takes into account concentrations over a threshold of 40 ppb (AOT40). They found that their stomatal-conductance-based modeling approach predicted very different spatial variability of ozone damage than the AOT40 maps, which demonstrates the importance of considering deposition velocity when creating atmospheric models.

It is also important to consider sub-grid spatial variability in deposition. Atmospheric models typically assume grid cells ranging in size from 10-100 km and 100-500 km, for regional and global models, respectively. The EPA operates the Community Multiscale Air Quality (CMAQ) model,

which is used for air-quality management, with 12 km x 12 km grid cells. Large amounts of spatial variability within a grid cell of a model can lead to poor estimates of trace-gas flux and concentration. With the reduction of sub-grid variability in mind, the monitoring sites used for model inputs are chosen to be representative of the surrounding areas, but accurate representations of an entire grid cell cannot always be achieved (Clarke et al., 1997).

Tong and Mauzerall (2006) evaluated the ability of the (CMAQ) model to capture spatial variability in ozone concentrations in the United States. They compared summertime, surface-level ozone concentrations predicted by CMAQ with observations from 987 Air Quality Systems (AQS) sites and 123 Clean Air Status and Trends Network (CASTNET) sites. They found that CMAQ systematically overpredicts O_3 concentrations in the east by 15-20 ppbv, and underpredicts concentrations in the west by 10-15 ppbv. These over- and under-predictions can result from uncertainty in many different variables (meteorological data, emissions, etc.), one of which is deposition velocity. These inaccuracies are a concern because studies have begun to use CMAQ concentrations to evaluate the impacts of air pollution on health, and they can lead to great over- or underestimations of exposure.

2.0.4 Low-cost Sensors

The instruments typically used to measure trace-gas concentrations in flux-measurement systems cost between $5000 and $100,000. Flux chambers are advantageous because they do not require the high-sampling-rate instruments needed for eddy covariance. Low-cost sensors have the potential to be used for flux-chamber measurements.

Federal reference method (FRM) measurements of O_3 are taken using monitors that rely on the detection of chemiluminescence, which is the product of the reaction between O_3 and ethylene gas (EPA, 2013). These monitors typically cost USD 10 000 to 20 000, and use approximately 1 kW of power. A slightly less costly method for measuring ozone concentrations is UV absorption, which is a federal equivalence method (FEM). UV absorption sensors typically cost USD 2000 +. Metal oxide (MO_x) ozone sensors, which we use in our low-cost monitors, cost between USD 5 and 100,

with power consumption as low as 90 mW. Metal-oxide sensors consist of a high surface-to-volume ratio semiconducting material on a heated insulating substrate, between two electrodes (Moseley, 1997). Reactions with trace-gas molecules on the semiconductor surface change the density of charge carriers available, which changes the conductance. The resistance across the electrode decreases proportionally to the increase in trace-gas concentration.

The metal-oxide O_3 sensors in the flux chambers have been used in other studies at CU. (Piedrahita et al., 2014b) developed low-cost, wearable air-quality monitors, and evaluated their performance. They calibrated their monitors in a collocation study, and found that the O_3 sensors had a median standard error of 9.7 ppb.

Other research groups, including Mead et al. (2013), Aoki et al. (2008), Williams et al. (2009) and Hasenfratz et al. (2012) have used MO_x sensors to measure ozone in previous studies. While MO_x sensors cost 0.05 - 5% as much as UV absorption and chemiluminescence sensors, their use is not without challenges. MO_x sensors respond to changes in ambient temperature and relative humidity, and their output is non-linear with respect to gas concentration (Barsan and Weimar, 2001; Delpha et al., 1999; Marco, 2014; Masson et al., 2015; Piedrahita et al., 2014a; Romain et al., 1997; Sohn et al., 2008). Additionally, response can vary from sensor to sensor (Romain and Nicolas, 2010). Correcting sensor responses to changes in temperature and humidity is particularly difficult in dynamic flux chambers, since the humidity and temperature of the sample air change rapidly when the chamber lid closes.

To account for these cross-sensitivities, and improve sensor calibrations, several groups have explored the use of machine-learning algorithms. Sundgren et al. (1991) used partial least squares and artificial neural network models to calibrate MO_x H, NH_3 and acetone sensors. Di Natale et al. (2002) used independent component analysis to separate environmental disturbances from the meaningful portion of their data for an electronic nose. Kamionka et al. (2006) calibrated MO_x O_3 and NO_2 sensors using neural networks. De Vito et al. (2009) used neural networks to calibrate their MO_x CO, NO_x and NO_2 sensors, which they used to monitor urban air pollution. Zampolli et al. (2004) used a fuzzy associative memory neural network to calibrate MO_x CO and

NO_2 sensors. Wolfrum et al. (2006) calibrated metal-oxide VOC sensors using principal component analysis and partial least squares regression models. Vergara et al. (2013) calibrated a metal-oxide sensor array using support vector machines.

Chapter 3

Chamber Validation Paper

The first paper on this work, which was published in Volume 8 of Atmospheric Measurement Techniques, follows.

3.1 Introduction

Deposition of pollutants, including ozone, nitrogen, and acidic compounds (SO_x, NO_y), places environmental stress on sensitive vegetated landscapes and aquatic ecosystems (Fangmeier et al., 1994; Williams and Tonnessen, 2000). Examples of this stress include increased susceptibility to injury and decreased growth for sensitive plant species, decreased water quality, toxicity to freshwater organisms, eutrophication, change in greenhouse emissions from soil (Fenn et al., 1998), reduction in biodiversity, and interference with a plant's uptake of other important cations, such as potassium (Fangmeier et al., 1994). These negative effects can be particularly pronounced at high altitudes, where buffering capacities can be below average (Benedict et al., 2013; Fenn et al., 1998; Williams and Tonnessen, 2000). There has been debate over whether ozone damage to vegetation is best quantified and regulated using ambient concentrations or atmospheric fluxes (Musselman et al., 2006). While the use of ambient concentrations is certainly much simpler, fluxes have more physical meaning.

Additionally, understanding deposition and emission rates is an important piece of estimating atmospheric concentrations in the planetary boundary layer for climate and weather models. Since it is not possible to measure flux everywhere, improving deposition models is a crucial step in

determining accurate transfer ratios. Efforts to improve models are ongoing (Brook et al., 1999; Zhang et al., 2001, 2003); models estimate flux well under some conditions, but fluxes determined by different models and observations can vary by a factor of 2 to 3 (Flechard et al., 2011; Schwede et al., 2011; Wu et al., 2011). Direct dry-deposition measurements are needed to improve and validate models for different ecosystems, and under varied environmental conditions.

Dry deposition, which is the process by which pollutants are transported from the atmosphere to the earth's surface without precipitation (Seinfeld and Pandis, 2006), is an important component of atmospheric deposition. This process is estimated to account for up to 50 % of total atmospheric deposition in the United States (EPA, 2010; Wesely and Hicks, 2000). Despite this sizable contribution to total atmospheric deposition, there is a lack of direct measurements for sulfur and nitrogen dry-deposition in the US. Currently employed direct dry-deposition measurements are not part of the routine measurement suite (Clean Air Status and Trends Network) because they are prohibitively expensive and complex. This results in significant uncertainty in deposition loads, specifically regarding transfer ratios (the relationship between ambient concentrations and total deposition). Given the large spatio-temporal variability in air-surface exchange rates of reactive compounds, there is a need for low-cost, easily deployable systems to measure dry deposition directly. These measurement devices should be automated and remotely controlled, so that they can be deployed for extended periods of time without excessive maintenance.

Currently, the most accurate direct method for measuring atmospheric fluxes is eddy covariance (Seinfeld and Pandis, 2006; Turnipseed et al., 2009). Eddy covariance consists of taking high-speed measurements of concentration and three-dimensional wind velocity. The flux is computed from the covariance between the fluctuating components of wind velocity and concentration (Turnipseed et al., 2009). This method is the most mathematically robust and accurate way to acquire dry-deposition measurements, but it is expensive and technically difficult compared with indirect measurement methods (Baldocchi et al., 1988).

Another method for measuring flux, which is used more frequently to measure emissions than it is to measure deposition, is the flux chamber. Advantages of flux chambers over eddy covariance

include reduced cost, the ability to determine spatial variability in deposition, the ability to take measurements in areas with complex topography and areas with non-uniform vegetation (eddy-covariance typically requires an area of uniform vegetation that is $\geq 100\,m^2$), mobility, and the potential to be used with inexpensive sensors (Horst and Weil, 1994). The main drawback of using chambers for flux measurements is that they alter the environment in which they are placed. Static chambers, which are commonly used to measure emissions, significantly affect environmental conditions (Pape et al., 2008).

Dynamic flux chambers minimize the alteration of environmental conditions by constantly pumping ambient air into the chamber. Table 3.1 lists previous flux-chamber measurements of NO, NO_2, CO_2 , and O_3. One type of flux chamber listed in Table 3.1 is the leaf-scale dynamic chamber, which is used to measure fluxes to and from individual leaves and branches (Altimir et al., 2002; Breuninger et al., 2012a,b; Gessler et al., 2000; Sparks et al., 2001). While leaf-scale deposition measurements are important for understanding plant dynamics, they can be difficult to translate to the canopy scale, and do not directly represent ecosystem-level flux.

Another type of chamber listed in Table 3.1 is the dynamic soil-flux chamber (Butterbach-Bahl et al., 1997; Norman et al., 1997; Remde et al., 1993). A significant portion of the chambers listed did not have open tops, and the soil or vegetation in the chamber was only exposed to ambient conditions via air pumped into the chamber. These chambers, which are not normally open to the ambient environment, have significant drawbacks. They all block a fraction of incoming solar radiation, and in order to maintain ambient conditions, they have to be moved frequently, which makes long-term or remote deployments difficult.

Several research groups have addressed these issues by developing chambers with lids that open and close automatically (Kitzler et al., 2006; Meixner et al., 1997; Pape et al., 2008). These automatic chambers operate in a normally open mode, with lids that close for just a few minutes per hour. Provided that the chambers are made out of highly transparent materials, so sunlight can reach the vegetation inside, the environmental conditions in the chamber remain very close to ambient (Pape et al., 2008).

While many chamber measurements have been made (Table 3.1), very few of these studies compare O_3 fluxes measured by chambers to measurements acquired via micrometeorological techniques. Several groups have compared chamber measurements NO fluxes from soils to gradient measurements (Kaplan et al., 1988; Parrish et al., 1987; Stella et al., 2012). Norman and coworkers (1997) compared several types of static and dynamic chambers with each other and eddy correlation for measuring CO_2 fluxes in forest soils, but only two data points for eddy correlation were available for comparison, each representing one day. Li and coworkers (1999) compared chamber measurements of NO fluxes from agricultural soils with eddy-correlation measurements, and found that the fluxes measured by the chambers were higher than the eddy-correlation measurements, but followed a similar diurnal trend. Pape and coworkers (2008) compared an automatic, dynamic flux chamber with an eddy-covariance system at a grassland site, and demonstrated good agreement for CO_2 deposition. Due to the fact that these comparison studies are limited in number, and sometimes did not yield good agreement between methods, further comparisons of flux chambers and micrometeorological methods are warranted.

Our research effort expands on this validation-based flux-chamber development through the creation of an automated, inexpensive, and continuous multiple-species gas-flux monitoring system, which can provide data for a variety of relevant atmospheric pollutants, including O_3, CO_2, and NO_x. The chambers have automatic lids, which keeps the environment in the chambers close to ambient, and eliminates the need to regularly remove them from sampling plots. This project is unique, because, in addition to contributing to the very limited chamber-validation literature, our chambers are designed to be very inexpensive ($< \$2000$ each). The chambers are equipped with inexpensive metal-oxide O_3 and NO_2 sensors, which cost between \$10 and \$100, and our ultimate goal is to obtain fluxes using these inexpensive sensors. The first step toward reaching that goal is to use data from established O_3 monitors to validate the dynamic flux-chamber measurements, which enables us to isolate the uncertainty related to the use of inexpensive sensors from chamber performance. We present preliminary results, comparing chamber fluxes to eddy-covariance fluxes for O_3.

Table 3.1: Summary of Selected Chamber Measurements of NO_2, NO, O_3, and CO_2

Reference	Gases Measured	Surface	Chamber Type	Validation Method
Aeschlimann et al. (2005)	CO_2	grassland	dynamic	none
Altimir et al. (2002)	CO_2, O_3	Scots Pine Shoots	dynamic, shoot chamber	compared w/ typical O_3 flux values
Aneja et al. (1995)	NO_2, NO	Agricultural Soil	dynamic	none
Breuninger et al. (2012b)	NO_2, NO, CO_2, O_3	Norway Spruce	dynamic, branch chamber	none
Breuninger et al. (2012a)	NO_2, NO, CO_2, O_3	Norway Spruce	dynamic, branch chamber	none
Burkart et al. (2007)	CO_2	barley, sugar beet, wheat	dynamic	destructive harvest
Butterbach-Bahl et al. (1997)	NO_2, NO, O_3	forest soil	dynamic, automated lid	none
Garcia et al. (1990)	CO_2	soybeans	dynamic	none
Gessler et al. (2000)	NO_2, CO_2, NH_3	beech saplings and twigs	dynamic	none
Gut et al. (1999)	NO	wheat	dynamic	model comparison
Gut et al. (2002)	NO_2, NO, CO_2, O_3	soil	dynamic	model comparison (using ambient concentration)
Horváth et al. (2006)	NO, O_3	spruce and oak soil	dynamic	none
Kaplan et al. (1988)	NO	forest soil	dynamic	compared well with nighttime vertical profile
Kirkman et al. (2002)	NO_2, NO, O_3	pasture	dynamic	none
Kitzler et al. (2006)	NO_2, CO_2	forest soil	dynamic, automated lid	none
Laville et al. (2011)	NO, CO_2	agricultural soil	dynamic, automated lid	none
Li et al. (1999)	NO	agricultural soil	dynamic	chamber values larger than eddy-covariance, but varied similarly with time
Machon et al. (2010)	NO	grassland	dynamic	compared with model
Maljanen et al. (2007)	NO	dung and urine patches on soil	dynamic	none
Meixner et al. (1997)	NO, NO_2, O_3	grassland & crops	dynamic, automated lid	none
Norman et al. (1997)	CO_2	forest soil	dynamic & static	compared 5 types of chambers and 2 eddy-covariance data points
Pape et al. (2008)	NO_2, NO, CO_2, O_3	grassland	dynamic, automatic lid	very good agreement w/ eddy covariance for CO_2 (did not compare NO, NO_2, & O_3)
Parrish et al. (1987)	NO	grassland	dynamic	nighttime comparison with gradient method
Pilegaard et al. (1999)	NO, CO_2	forest soil	dynamic	none
Pilegaard (2001)	NO, NO_2, O_3	forest soil	dynamic, automated lid	none
Remde et al. (1993)	NO, NO_2, O_3	marsh soil	dynamic	none
Roelle et al. (1999)	NO, NO_2	corn soil	dynamic	none
Roelle et al. (2001)	NO	agricultural soils	dynamic	none
Skiba et al. (1993)	NO	ryegrass	dynamic	none
Slemr and Seiler (1984)	NO, NO_2	grassland soil	dynamic	none
Sparks et al. (2001)	NO_2	25 leaf species	dynamic leaf chamber	none
Stella et al. (2012)	NO	agricultural soil	dynamic, automated lid	agreed with gradient method for low fluxes, but underestimated high fluxes
Unsworth et al. (1984)	O_3	soybeans	dynamic, open top	canopy resistances comparable to other field studies
Dijk and Duyzer (1999)	NO	forest soil	dynamic	none
Williams and Davidson (1993)	NO	grassland	dynamic	comparison of 2 chamber types
Yamulki et al. (1995)	NO	agricultural soil	dynamic	none

3.2 Methods

3.2.1 Overview

We conducted gas-phase dry-deposition experiments in a grassy clearing in the Blackwood Division of Duke Forest in Orange County, North Carolina, USA (35.97 N, 79.09 W). The field is

480 m x 305 m, and the vegetation is primarily tall fescue (Festuca arundinacea Shreb.), which is a common C3 grass in the southeastern United States. Less-prominent vegetation includes C3 and C4 grasses, herbs, and forbs, which are present in smaller amounts (Fluxnet, 2015).

We used five pairs of acrylic-glass flux chambers to measure dry deposition of O_3 to the grassland vegetation. Experiments were carried out in June and September, under a variety of meteorological conditions. We compared the chamber results with eddy-covariance measurements, which were conducted by the EPA at the same site.

3.2.2 Leaf-Area Index

The LAI in the field, as well as in Chambers A and B, was measured on November 11th. LAI measurements in the open field were made by sampling at regular distances along 100 m transects (n = 10 locations) to the southwest and northwest of the eddy-covariance tower (prevailing fetch) with a LI-COR Model LAI-2000 plant canopy analyzer (LI-COR Biosciences, Lincoln, NE). LAI measurements within the chambers were made by inserting the leaf area meter through a port at the bottom of the chamber. Individual measurements consisted of one above-canopy measurement and five below-canopy measurements. Three replicate measurements were taken in each chamber. Measurements within the control chambers showed no difference between above- and below-canopy measurements.

The LAI in the field was between 2.8 and 3.5, the LAI in chamber A was between 2.4 and 2.9, and the LAI in Chamber B was between 2.75 and 3.1. While the chamber-LAI measurements were on the low end of the field measurements, they were inside the range of LAI measurements in the field.

3.2.3 Eddy-Covariance Measurements

Briefly, the eddy covariance approach ((Baldocchi et al., 1988)) for measuring the vertical exchange of momentum, heat, and mass is based on the simplified form of the mass balance for a scalar (c), at time (t), in a notional control volume, at height (z) within the surface layer, expressed

as:

$$\frac{\overline{\partial c}}{\partial t} + \frac{\partial \overline{wc}}{\partial z} = \overline{S}\delta(z), \tag{3.1}$$

where $\overline{wc}$ is the total covariance of c and the vertical velocity, w, S is the surface exchange rate, and $\delta(z)$ is the Dirac delta function. Overbars denote Reynolds averaging. If the scalar field is stationary, the first term on the left-hand side of Equation (3.1) reduces to zero. After integrating from $z = 0$ to the top of the control volume (h), Equation (3.1) further reduces to

$$\overline{wc}(h) = S. \tag{3.2}$$

Finally, the total covariance, $\overline{wc}$, is decomposed into mean ($\overline{\overline{wc}}$) and fluctuating ($\overline{w'c'}$, i.e., eddy flux) components, using an appropriate averaging operation (i.e., Reynolds decomposition), such that $\overline{wc} = \overline{\overline{wc}} + \overline{w'c'}$. Assuming that the mean vertical velocity is zero, the surface exchange (S) becomes equivalent to the eddy-covariance flux:

$$F = \overline{w'c'}, \tag{3.3}$$

where the overbar represents time averaging, usually 30 minutes, and the primes represent deviations from the mean, e.g.,

$$c' = c - \overline{c}. \tag{3.4}$$

Above-canopy fluxes of CO_2, H_2O, O_3, sensible heat, and momentum were measured using an instrument package, which consisted of an R.M. Young sonic anemometer (Model 81000V, Traverse City, MI), aspirated thermocouple (Model ASPTC, Campbell Scientific, Logan, UT), LI-COR (Lincoln, NE) Model 7500 (CO_2 and H_2O) open path infrared gas analyzer (IRGA), and a custom fast chemiluminescence O_3 sensor, positioned at 2.5 m above the canopy. Gas-phase instruments were calibrated weekly by mass flow controlled dilution of compressed gas standards with clean air. Wind speed components (u, v, w), temperature, and air concentrations were sampled at a frequency

of 10 Hz, and data were recorded on a single laptop, using a custom data-acquisition system. Data were reduced to 30-minute and hourly averages using a custom SAS program (Institute, 2003).

Eddy-covariance O_3 fluxes were measured with a custom sensor that follows the basic design of Guesten and coworkers (1992), which consists of a pump (Model BTC IIS miniature diaphragm pump, Parker, Hollis, NH), a reaction cell, and a photomultiplier tube (Model H9306 side-on photosensor, Hamamatsu, Middlesex, NJ) (Guesten et al., 1992). While Guesten and coworkers (1992) are generally credited with developing the first of these systems for flux measurement applications, a number of variants of the original design have been developed over the following years (see Zahn et al. (2012)). This measurement technique is known as "dry chemiluminescence", and the air sample passes over a disk, which is coated with Coumarin-1 dye (Bagus Consulting, Speyer, Germany). The reaction of O_3 with the dye results in luminescence, which is quantified by counting the resulting photons with a photomultiplier tube that views the reaction chamber from the side opposite the Coumarin disk. The ozone concentration is proportional to the number of photons produced. However, this is not an absolute measurement, and the disks have a limited lifetime over which the photon yield per unit O_3 decreases. Thus, to calculate the absolute flux, the fast sensor must be calibrated to a second collocated sensor. The second sensor measures absolute O_3 concentrations, at a frequency consistent with the time scale of the flux, which is 30 minutes to one hour. The collocated instrument is a Model 205 dual-beam instrument (2B Technologies, Boulder, CO), which measures O_3 by UV absorption. Ozone fluxes were calculated from 10 Hz measurements, calibrated to the 2B sensor, using the ratio-offset method recommended by Muller and coworkers (Muller et al., 2010).

For flux calculations, 10 Hz data were subjected to spike filtering, 2-D coordinate rotation, correction for the time delay between the chemical sensor and vertical velocity, application of Webb-Pearmon-Leuning correction (CO_2, H_2O), and correction for high-frequency spectral attenuation (O_3) (Horst and Weil, 1994). The fast O_3 sensor has an effective time response of approximately 1.5 Hz. At lower frequencies, the cospectra of O_3 and vertical velocity match the shape of the temperature/vertical velocity cospectra well, with both following the generalized cospectral character-

istics described by Kaimal and Finnigan (Kaimal and J.Finnigan, 1994). In this case, the method described by Horst (1997) was used to correct for spectral attenuation at frequencies >1.5 Hz (Horst and Weil, 1994). Tests for stationarity and the presence of fully developed turbulence were also applied (Foken and Wichura, 1996).

3.2.4 Ancillary Measurements

Ancillary measurements included net solar radiation (Rebs Q7.1 Net Radiometer, Campbell Scientific, Logan, UT), photosynthetically active radiation (Model LI190 quantum sensor, LI-COR, Inc., Lincoln, NE), soil heat flux (Model HP101 heat flux plate, Hukseflux USA, Inc., Manorville, NY), soil temperature (thermocouple, OMEGA Engineering, Stamford, CT), soil volumetric water (Model CS615 water content reflectometer, Campbell Scientific, Logan UT) leaf wetness (Model 237, Campbell Scientific, Logan UT) and rainfall (Model TE525 rain gauge, Campbell Scientific, Logan, UT). Data are recorded on a Campbell Scientific CR23X data logger and reduced to 30-minute and hourly averages.

3.2.5 Flux-Chamber Description

The dynamic flux chambers, which are shown in Figure 3.1, were constructed using clear, cylindrically shaped acrylic. The chambers were constructed in pairs, and each pair had an open-bottomed chamber, which measured deposition to the vegetation inside, and a "blank" chamber, which had an acrylic bottom, and enabled us to measure deposition in the absence of vegetation. The "blank" measurement represents trace-gas losses to the chamber walls as well as any chemical reactions in the chamber that are unaccounted for in the flux calculations.

All of the chambers have a 45.7 cm diameter and 0.48 cm wall thickness. Four pairs of chambers have a height of 83.8 cm, and the remaining pair has a height of 58.4 cm. The chambers were designed with this height distribution because many species of natural vegetation, including grassland, are taller than 58.4 cm. The shorter chambers were designed to measure fluxes over shorter vegetation, such as alpine tundra, which is present in sensitive areas such as Rocky Mountain

National Park. The shorter chambers are likely more accurate for vegetation below 59 cm tall, since they increase the ratio of vegetative surface area to volume.

The chambers were designed to minimize deposition of trace gases to the chamber walls, which was accomplished by placing the inlet and outlet holes in locations that limited contact between the flow path and the chamber walls. Ambient air enters the chambers through four holes, which are each 5.2 cm in diameter, and evenly spaced around the circumference of the chamber. The chamber outlet is at the top of the chamber, as shown in Figure 3.2. The grass outside the chamber, near the inlet holes, is removed, which prevents trace gases from depositing to external vegetation before the air stream enters the chamber.

Air is pulled through the chamber by a US General 3 CFM Two-Stage Vacuum pump, and concentration samples were measured in one of two polytetrafluoroethylene (PTFE) tubes at the outlet. Gas-phase sampling is discussed in more detail in Section 3.2.6.

For most experiments, the pump was set to pull 80 L min^{-1} of air through the chamber. In addition to the flow induced by the vacuum pump, the 2B ozone monitor pulled approximately

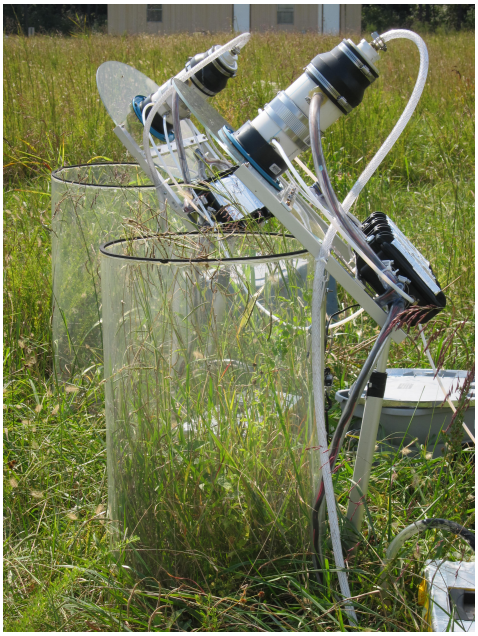

Figure 3.1: The photo above shows a pair of flux chambers at the field site in the Duke Forest.

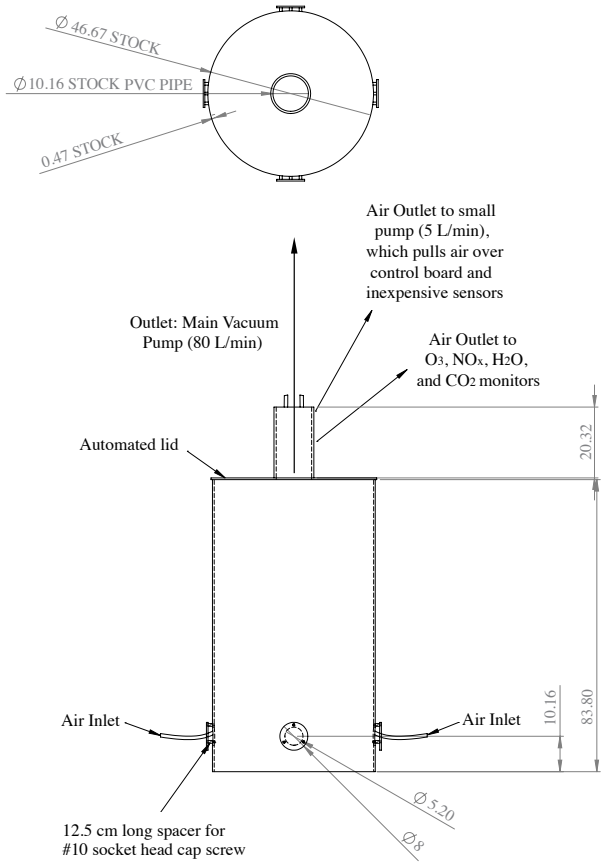

Figure 3.2: The plot above shows the dimensions of the chamber, and the locations of the air inlets and outlet.

$1\,\mathrm{L\ min^{-1}}$, and the small, inexpensive pump, which pulled air over the inexpensive sensors, pulled $5\,\mathrm{L\ min^{-1}}$. Thus, the total flow rate through the chamber was $86.35\,\mathrm{L\ min^{-1}}$, which equates to a residence time of 1.5 minutes. Pape and coworkers found that other researchers have operated dynamic flux chambers with residence times ranging from 10 seconds to 24 minutes, and chose to operate their dynamic flux chambers at a residence time of 40 seconds (Pape et al., 2008). Gillis and Miller found that changes in air-stream residence time in flux chambers caused proportional changes in mercury flux for both absorption and emission (Gillis and Miller, 2000). Aeschlimann and coworkers used a residence time of 15 seconds during the day and 60 seconds at night (Aeschli-

mann et al., 2005), which reflects ambient diurnal variation in friction velocity. Low residence times ensure that chambers are well-mixed, and minimize reactions between gases in the chamber. However, reducing residence times also reduces the difference in ambient and steady-state trace-gas concentrations in the chamber. Thus, as residence time is decreased, more precise instrumentation is required. We chose to operate our chambers with a 1.5-minute residence time, because 1.5 minutes is sufficiently low to keep environmental conditions close to ambient yet still yield a trace-gas concentration change that is large enough to be detected by inexpensive sensors. This residence time also translates to a flow rate that can be generated with an inexpensive pump. Further reducing the residence time would have required investment in a significantly more expensive pump, as well as more precise sensors, which would undermine the goal of creating an inexpensive flux-measurement system.

Another way that we reduced the cost of the chamber, was by designing our own control system, using inexpensive electronic components. A customized embedded-system platform was used to automate the flux chamber sampling system. The system is based on the low-cost M-Pod air quality monitor (Masson, 2015), with additional instrumentation for pump and actuator control. Firmware running on the common Atmel (San Jose, CA) Atmega 328 microcontroller controls both the data logging and flux-chamber sampling routine.

Each chamber runs approximately once an hour, and the main vacuum pump is off when the chamber is not sampling. Once per hour, a predefined and automated sampling schedule begins, and the vacuum pump turns on and runs with the lid open for 6.75 minutes. The pressure change caused by the pump can cause fluctuations in instrument readings, and this boot up time allows the instruments to stabilize before the chamber lid closes. After the 6.75 minute initialization, the chamber lid closes, and remains closed for 5 minutes. It is important to note that the eddy-covariance measurements are fluxes averaged over a 30-minute or 1-hour time period, and the chamber measurements are a 5-minute average, taken every 53 minutes.

Fluxes were calculated based on the assumption that the chamber was well mixed. A mass balance in the chamber yields the equation,

$$V\frac{d\mu_{\mathrm{j}}(t)}{dt} = Q\mu_{\mathrm{j,amb}} - Q\mu_{\mathrm{j}}(t) - F_{\mathrm{j}}A_{\mathrm{s}}, \tag{3.5}$$

where $\mu_{\mathrm{j}}(t)$ is the mixing ratio in the chamber of gas, j, with respect to time, Q is the flow rate of air through the chamber, $\mu_{\mathrm{j,amb}}$ is the ambient mixing ratio of gas, j, t is time, A_{s} is the surface area of the opening at the bottom of the chamber, V is volume of the chamber, and F_{j} is the flux of gas, j, to the vegetation. Differentiating, $\mu_{\mathrm{j}}(t)$ is found to be

$$\mu_{\mathrm{j}}(t) = \mu_{\mathrm{j,amb}} - \frac{F_{\mathrm{j}}A_{\mathrm{s}}}{Q}(1 - e^{-\frac{Q}{V}t}). \tag{3.6}$$

The steady-state solution to this equation, solving for flux, is

$$F = \frac{Q}{A_{\mathrm{s}}}(\mu_{\mathrm{j,amb}} - \mu_{\mathrm{j}}(\tau_{\mathrm{ss}})), \tag{3.7}$$

where τ_{ss} is the time when the trace-gas concentration in the chamber reaches steady state.

3.2.6 Gas-Phase Measurements

Figure 3.2 shows the flow path of sample air through the chamber. Gas-phase measurements were conducted at the chamber outlet, which consisted of an 11.4 cm diameter PVC pipe. Chamber air was pulled through the outlet via the main vacuum pump. Two 4.76 mm-diameter tubes were attached to the sides of the PVC pipe on one end, and instruments on the other. One tube was connected to a 2B Technologies Model 202 Ozone Monitor. The second tube was connected to a small vacuum pump, which moved air through the chamber control box.

In addition to the control board, the box housed metal-oxide NO_x and O_3 sensors. Additional data was collected using these commercially available sensors, specifically the Sensortech (Chemlsford, UK) (formerly e2v) MICs-2611 O_3 sensor. All low-cost sensors implemented in the flux-chamber system ranged in cost from \$10-\$100, and the O_3 sensors had a detection limit well within typical concentration changes seen in ground-flux measurements. Complex quantification schemes are necessary to quantify the sensor output properly. Such schemes incorporate correction

parameters for interference effects. Inexpensive sensor technology has the potential to be incorporated into a flux-chamber system effectively, which would make widespread flux measurements a realizable objective. More information about the instruments is available in Table 3.2.

3.2.7 Comparison of Eddy-Covariance and Flux-Chamber Measurements

Theoretically, dry deposition flux (F) is proportional to the ambient concentration (C) of a trace gas at some reference height (Seinfeld and Pandis, 2006). The proportionality constant between the concentration and flux is called "deposition velocity" (v_d) (Chamberlain and Chadwick, 1953), and

$$F = -v_\mathrm{d} C. \tag{3.8}$$

The deposition process has been described using a resistance analogy (Wesely and Hicks, 2000), in which species transport from the atmosphere to the surface of a material is controlled by three resistances in series.

$$v_\mathrm{d} = r_\mathrm{t} = r_\mathrm{a} + r_\mathrm{b} + r_\mathrm{c}, \tag{3.9}$$

where r_t is the total resistance to deposition, r_a is the resistance to aerodynamic transport, r_b is the resistance to diffusion through the quasi-laminar boundary layer, and r_c is the resistance to uptake of a trace gas by the canopy.

This resistance analogy is based on the assumption that the atmosphere is unaltered. It is an accurate analogy for eddy-covariance measurements, but flux chambers alter the wind speed above

Table 3.2: Trace Gas Detectors, with Manufacturers' Specifications

Gas	Detection Method	Manufacturer & Model	Detection Limit	Precision
O_3	UV Light Absorption	2b Technologies (Boulder, CO) 202	1.5 ppb	± 1.5 ppb
NO_x	chemiluminescence	Thermo Scientific (Waltham, MA) 42S	0.4 ppb	± 0.4 ppb
CO_2	non-dispersive infrared	LI-COR (Lincoln, NE) 7000	0 ppm	0.01 ppm
H_2O	non-dispersive infrared	LI-COR (Lincoln, NE) 7000	0 ppm	0.01 ppm

the canopy, so the resistance analogy must be adjusted. Pape and coworkers proposed an alternate resistance scheme (Pape et al., 2008), which replaces r_{a} with r_{purge} and r_{mix}, which represent the purging resistance between ambient and chamber air, and mixing in the chamber, respectively. When the chamber is well mixed, r_{mix} is very small, and it can therefore be neglected in this case. r_{b} is replaced with a modified boundary-layer resistance, r_{b}^{*}. r_{c} should be modified very little by the chamber, provided the chamber does not substantially alter the environmental conditions (temperature, relative humidity) of the natural environment.

Thus, the ratio of chamber flux to ambient flux can be written as

$$\frac{F_{\mathrm{cham}}}{F_{\mathrm{amb}}} = \frac{r_{\mathrm{a}} + r_{\mathrm{b}}^{*} + r_{\mathrm{c}}}{r_{\mathrm{purge}}} + \rho_{\mathrm{d}}(\mu_{\mathrm{comp}} - \mu_{\mathrm{amb}}), \tag{3.10}$$

where ρ_{d} is the molar density of dry air molecules, and μ_{comp} is the compensation point mixing ratio (Pape et al., 2008).

The results presented in this paper are not corrected using this ratio. While this conversion factor enables chamber flux to be scaled to eddy-covariance flux, it significantly increases the complexity of data processing, and introduces modeling assumptions to an otherwise direct measurement. We present a direct comparison between chamber and eddy-covariance measurements, and will note any bias in chamber measurements.

3.3 Results & Discussion

3.3.1 Data Processing

We collected O_3 flux data for 8 days. We used two pairs of identical tall chambers, and one pair of shorter chambers. Each set of data was based on a five-minute sampling period, which occurred once per hour. The flux during each sampling period was assumed to be constant. Each data run was analyzed for noise and pattern, and some data sets excluded from results.

Figure 3.4 is an example of a sampling period that we excluded from our results. The ozone concentration increased by an unreasonable amount when the chamber lid opened, which likely

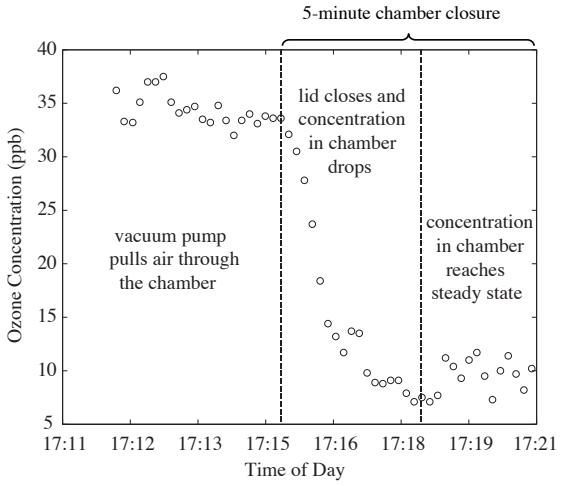

Figure 3.3: The plot above is an example of ozone data that can be analyzed using the steady-state mass-balance equation. The data before the lid is closed and at the end of the sample both have low noise, and stay relatively constant for at least one minute.

indicates malfunction in the 2B ozone monitor. 9 % of Chamber A data were excluded, 11 % of Chamber B data were excluded, and 0 % of the Chamber C data were excluded.

Figure 3.3 shows the ozone concentration in the chamber during one sampling period, as an example of ozone data that can be analyzed using the steady-state solution. The area before the decline of the ozone concentration represents the time period when the chamber lid was open. After the lid closed, the concentration began to decline, and eventually reached a steady-state value. This data set met our data-quality requirements, as the data just before the lid closed and at the end of the sample both have low noise, and stay relatively constant for at least one minute. Therefore, the flux was computed using the steady-state solution (Equation (3.7)).

When the ambient ozone concentration is below 5 ppb, we assume that the ozone flux is zero. Ambient O_3 concentrations of 5 ppb or lower typically occur only at night, when wind speeds are low, which means that the aerodynamic resistance to deposition is high, equating to a low flux. The absolute highest flux rate that could occur, with an ambient concentration of 5 ppb, is 0.09 μg m^{-2} s^{-1} (from Equation (3.7)), and a flux rate this high is very unlikely with low wind speeds. The median ozone-flux rate measured via eddy covariance, when the ambient ozone concentration

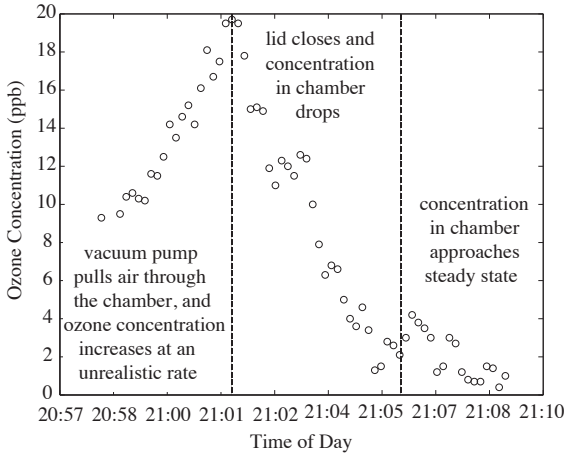

Figure 3.4: The plot above is an example of a run where the data could not be used to calculate a flux. The ozone concentration increases by an unreasonable amount when the chamber lid opens, which likely indicated malfunction in the 2B ozone monitor.

was ≤ 5 ppb, during the eight-day sampling period, was 0 μg m^{-2} s^{-1}, with a standard deviation of 0.05 μg m^{-2} s^{-1}.

We did not use the blank chamber data to make any adjustments to the fluxes measured by the dynamic chambers. The median difference between ambient concentration and steady-state ozone concentration was 1.9 ppb for the blank chambers. Since the uncertainty in ozone concentrations, measured by the 2B ozone monitor is $\pm$1.5 ppb, the concentration difference is within a 95 % confidence interval for noise. Thus, correcting chamber fluxes for blank flux would only introduce more error into our measurements.

Also, the median flux measured by the blank chambers, when the open-bottom-chamber flux was nonzero, was -0.001 μg m^{-2} s^{-1}. This value is less than 1 % of the median of the non-zero open-bottom-chamber fluxes, which was -0.21 μg m^{-2} s^{-1}. Therefore, correcting for the blank chamber fluxes would not have a significant impact on measurements. It was encouraging that the blank fluxes were so small, since this indicated that wall losses do not have a significant impact on the flux-chamber measurements. Since wall losses were insignificant, the chamber design could be further simplified by eliminating the blank chambers.

3.3.2 Photochemistry in the Chamber

Photochemical reactions between NO, NO_2, and O_3 can occur in the chamber, and therefore must be considered in Equation (3.5) (Meixner et al., 1997), (Pape et al., 2008). The primary reactions of concern are

$$NO + O_3 \rightarrow NO_2 + O_2 \tag{3.11}$$

and

$$NO_2 + h\nu \xrightarrow{O_2}, NO + O_3,\ \lambda < 420\,\text{nm}. \tag{3.12}$$

Because of the relationships shown in reactions 3.11 and 3.12, NO, NO_2 and O_3 must all be measured simultaneously (Pape et al., 2008). Using reactions 3.11 and 3.12, the change in NO and NO_2 mixing ratios is:

$$\frac{\mathrm{d}\mu(\mathrm{NO})}{\mathrm{d}t} = -k\,\mu(\mathrm{NO})\,\mu(\mathrm{O_3}) \tag{3.13}$$

$$\frac{\mathrm{d}\mu(\mathrm{NO})}{\mathrm{d}t} = j(\mathrm{NO_2})\,\mu(\mathrm{NO_2}), \tag{3.14}$$

where k is the first-order rate constant of Equation (3.11), and $j(NO_2)$ is the photolysis rate of NO_2 (Pape et al., 2008; Seinfeld and Pandis, 2006). The net source (S_{gp}) of gas-phase NO resulting from Reactions (3.11) and (3.12) within the chamber, is

$$S_{\mathrm{gp}}(\mathrm{NO}) = \mathrm{V}[\,j(\mathrm{NO_2})\,\mu_{\mathrm{cham}}(\mathrm{NO_2}) - k\,\mu_{\mathrm{cham}}(\mathrm{NO})\,\mu_{\mathrm{cham}}(\mathrm{O_3})]. \tag{3.15}$$

The rates of formation for NO_2 and O_3 are equal or inversely proportional to the rates of formation for NO, and

$$S_{\mathrm{gp}}(\mathrm{NO}) = S_{\mathrm{gp}}(\mathrm{O_3}) = -S_{\mathrm{gp}}(\mathrm{NO_2}). \tag{3.16}$$

Combining these reaction sources or sinks with the mass balance from Equations (3.5) and (3.7) yields

$$V\frac{dC_{\mathrm{j}}(t)}{dt} = Q\mu_{\mathrm{j,amb}} - Q\mu_{\mathrm{j}}(t) - F_{\mathrm{j}}A_{\mathrm{s}} + S_{\mathrm{gp}}, \tag{3.17}$$

and

$$F = \frac{Q}{A_{\mathrm{s}}}(\mu_{\mathrm{j,amb}} - \mu_{\mathrm{j}}(t)) + \frac{S_{\mathrm{gp}}}{A_{\mathrm{s}}}. \tag{3.18}$$

Pape and coworkers measured $j(\mathrm{NO_2})$ inside their chamber, and found that the average value of $j(\mathrm{NO_2})$ inside the chamber was 48 % of the value outside the chamber (Pape et al., 2008). They fit a curve of $j(\mathrm{NO_2})$ versus global radiation (G), and we used that curve in our calculations, since our chambers were similar in shape and material. To quantify the impact of this assumption, we calculated how increasing and decreasing $j(\mathrm{NO_2})$ by 25 % affects ozone flux, and found that this changes ozone flux by <1 % in all cases. The maximum flux change due to photolysis in all of our results is 1.7 %. Thus, the impact of photolysis on ozone flux was small during our study.

3.3.3 Results

We measured ozone dry deposition with flux chambers for two days in June, and eight days in September. When compared with eddy-covariance measurements, flux-chamber ozone measurements were able to capture the diurnal flux trends. It is important to remember that eddy-covariance measurements are not without error. For an eddy-covariance system similar to the one used in this study, Finkelstein and Sims ((Finkelstein and Sims, 2001)) found that mean sampling errors for 30-minute-average eddy-covariance $\mathrm{O_3}$ fluxes were in the range of 27-33 %.

Figure 3.5 shows $\mathrm{O_3}$ fluxes measured via eddy covariance, and flux chambers A, B and C, and also calculated using an indirect method, which combined meteorological data and surface-exchange model for the time period between September 22nd and September 28th. The theory used to calculate the model values is described by Wesely (1989) and Seinfeld and Pandis (2006).

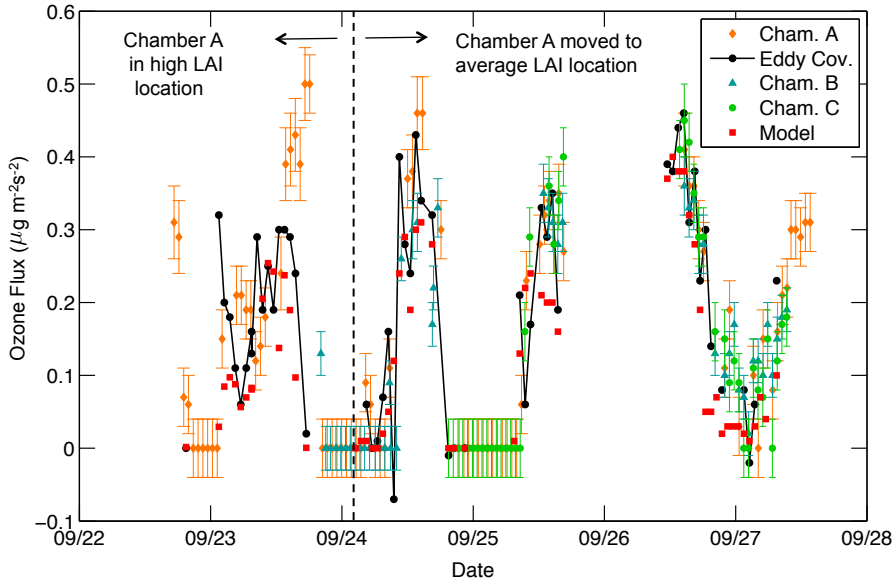

Figure 3.5: The plot above compares O_3 fluxes measured using eddy covariance (solid black line and black dots), surface-exchange modeling (red triangles), and flux chambers A (orange diamonds), B (blue stars), and C (green dots). The tick marks represent midnight on the date listed.

The surface-exchange model results underestimated the mean eddy-covariance flux rate by 26 % between September 22nd and 27th. This is a good model-to-measurement match, but it is important to remember that the models do not always predict flux accurately (Wu et al., 2012), (Schwede et al., 2011).

Chamber A was moved from its original location in the field to a different position on September 24th. Prior to being moved, the chamber was on a plot of land with a less-prevalent vegetation type, which had a higher LAI than the dominant vegetation (see Figure 3.6) . After the chamber was moved to a location with more representative vegetation, the data matched the eddy-covariance results much better. Before the chamber was moved (September 18th and 23rd), the mean ozone-flux rate measured by eddy-covariance was -0.16 μg m^{-2} s^{-1}, and the mean chamber flux rate was -0.23 μg m^{-2} s^{-1}, which is 48 % higher than the eddy-covariance measurement. After the move (September 24th-27th), the mean eddy-covariance flux rate was -0.25 μg m^{-2} s^{-1}, and the mean flux measured by the chamber was -0.26 μg m^{-2} s^{-1}, which is 4 % higher than the eddy-covariance measurement. This difference in measurement agreement highlights the importance of selecting a

Figure 3.6: Chamber A (left). Chamber B (right) – The vegetation in Chamber A, prior to being moved on 9/24, was not representative of the typical vegetation type or LAI at the site. As a result, flux measurements prior to the move were large when compared with measurements from other chambers and eddy covariance. The vegetation in Chamber B was representative of the vegetation in the field.

chamber placement that contains vegetation representative of that in the footprint of the eddy-covariance tower.

Chamber B operated from September 18th to 19th, and again from September 23rd to September 27th. The mean ozone flux measured by the flux chamber during this period was -0.17 μg m^{-2} s^{-1}, which is 9 % higher than the mean eddy-covariance ozone flux during the same period (-0.15 μg m^{-2} s^{-1}).

Chamber C, which is the shorter chamber, was operated between September 18th and 19th, and again between September 24th and 27th. The mean chamber flux measured during this period was -0.115 μg m^{-2} s^{-1}, which was 6 % lower than the mean eddy-covariance flux during the same time period (-0.108 μg m^{-2} s^{-1}).

In addition to the September measurements, data were collected for four days in June. The chambers underestimated ozone flux by 50-100 % in June, and we believe that this was because

the the LAI was much lower in the chambers than in the field during that time. We did not measure LAI during our June sampling period, but we estimate, by visual inspection, that LAI in the chambers was about 50 % lower in June than in September. The mean grass height in the field did not significantly change between June and November, and measured heights were 42.2 and 43.7 cm, respectively. Further studies that measure ozone deposition with various known LAI values in the chamber could confirm the effects of changing LAI on measured flux.

There was not a systemic bias in the ozone flux data. The excellent agreement between the September flux-chamber and eddy-covariance measurements demonstrates that the flux chamber is capable of measuring ozone flux to grassland ecosystems when the LAI inside the chamber represents the average LAI in the field. Therefore, we conclude that, under the environmental conditions in this study, it is not necessary to use Equation (3.10) to scale the dynamic-chamber flux to the eddy-covariance flux.

3.4 Conclusions

Ozone deposition onto grassland ecosystems was measured using dynamic flux chambers and eddy covariance. Measurements from the two methods matched very well (4–10 % difference) when the LAI inside the chambers was representative of the average LAI in the field. This discrepancy is within the uncertainty of eddy covariance, and the flux chambers are considered an accurate measurement system under these conditions. There was not a bias in the chamber data, when compared with the eddy-covariance data.

When LAI inside the chambers was significantly higher or lower than the rest of the field, chamber measurements over- or under-predicted flux, respectively. A discrepancy between chamber and average LAI values can be caused by both inconsistency in vegetation density and differences in vegetation species. Eddy-covariance systems can only measure net flux to an entire fetch ($>100\,\mathrm{m}^2$), which means that they measure a mean flux to all vegetation in the field, and cannot measure flux to small patches of different vegetation types. Flux chambers are able to measure flux onto different patches of vegetation, which enables the user to understand the relative contribution of different

vegetation species to total flux.

We found that the median ozone flux measured by the blank chambers, when the open-bottom-chamber flux was non zero, was -0.001 μg m^{-2} s^{-1}. This value is less than 1 % of the median of the non-zero open-bottom-chamber fluxes, which was -0.21 μg m^{-2} s^{-1}. Therefore, we can conclude that we achieved the design goal of minimizing trace-gas interactions with the walls of the chamber.

Chapter 4

Metal-Oxide Sensor Calibration Methods Paper

The second paper on my work, which focuses on improving the performance of metal-oxide ozone sensors via statistics and machine learning, follows this page. It is being submitted to Atmospheric Measurement Techniques.

4.1 Introduction

Exposure to high concentrations of ozone can cause a variety of negative health effects (Lippmann, 1989). These effects include lung inflammation, increases in respiratory-system-related hospital visits, cardiopulmonary mortality, and alterations in sleep patterns, neurotransmitters, short and long term memory, and motor activity (EPA, 2013). State and federal regulatory agencies take continuous measurements of ozone concentrations at centralized locations. Because current ozone monitoring systems are costly and consume large quantities of power, the number of monitoring sites is limited.

Ozone concentrations can vary spatially, and are often lower in the immediate vicinity of roadways due to reactions with NO (EPA, 2013). Concentrations can also be higher in locations downwind of an urban area than in the urban core, due to ozone's formation as a secondary pollutant. These local-scale variations can have a sizable impact on the relative magnitude of ozone concentrations in urban areas. This variability in outdoor ozone concentrations can lead to error estimates of personal exposure. Additionally, since the ratio of indoor and outdoor ozone concentrations varies based on air-exchange rate and a number of other factors, and the amount

of time individuals spend indoors varies from person to person, ratios between personal exposure and ambient outdoor concentration can vary between 0.1 and 0.9 (EPA, 2013). More accurate measurements of personal exposure can be obtained through the use of monitoring networks with high spatial coverage, as well as portable devices. This scale of measurements has historically been prevented by the cost of monitoring devices, but recent development of low-cost monitors is aimed at solving this problem (Almand-Hunter et al., 2015; Aoki et al., 2008; Hasenfratz et al., 2012; Mead et al., 2013; Piedrahita et al., 2014a; Shum et al., 2011; Williams et al., 2009).

Federal reference method (FRM) measurements of O_3 are taken using monitors that rely on the detection of chemiluminescence, which is the product of the reaction between O_3 and NO (EPA, 2013). These monitors typically cost USD 10 000 to 20 000, and use approximately 1 kW of power. A slightly less costly method for measuring ozone concentrations is UV absorption, which is a federal equivalence method (FEM). UV absorption sensors typically cost USD 2000 +, and consume approximately 4 W of power. Metal oxide (MO_x) ozone sensors, which we use in our low-cost monitors, cost between USD 5 and 100, with power consumption as low as 90 mW.

Mead et al. (2013), Aoki et al. (2008), Williams et al. (2009) and Hasenfratz et al. (2012) used MO_x sensors to measure ozone in previous studies. While MO_x sensors cost 0.05 - 5% as much as UV absorption and chemiluminescence sensors, their use is not without challenges. MO_x sensors respond to changes in ambient temperature and relative humidity, and their output is non-linear with respect to gas concentration (Barsan and Weimar, 2001; Delpha et al., 1999; Marco, 2014; Masson et al., 2015; Piedrahita et al., 2014a; Romain et al., 1997; Sohn et al., 2008). Additionally, response can vary from sensor to sensor (Romain and Nicolas, 2010).

Many groups have explored the use of machine-learning algorithms for improving sensing results. Sundgren et al. (1991) used partial least squares and artificial neural network models to calibrate MO_x H, NH_3 and acetone sensors. Di Natale et al. (2002) used independent component analysis to separate environmental disturbances from the meaningful portion of their data for an electronic nose. Kamionka et al. (2006) calibrated MO_x O_3 and NO_2 sensors using neural networks. De Vito et al. (2009) used neural networks to calibrate their MO_x CO, NO_x and NO_2 sensors, which

they used to monitor urban air pollution. Zampolli et al. (2004) used a fuzzy associative memory neural network to calibrate MO_x CO and NO_2 sensors. Wolfrum et al. (2006) calibrated metal-oxide VOC sensors using principal component analysis and partial least squares regression models. Vergara et al. (2013) calibrated a metal-oxide sensor array using support vector machines.

This work is focused on the use of machine learning techniques for improving metal-oxide ozone sensor calibrations. Collocation calibrations were performed, as previous deployments have revealed that collocation calibrations, with real-world ambient conditions, provide more accurate concentration estimates than laboratory calibrations (Piedrahita et al., 2014a).

4.2 Methods

4.2.1 Experimental Setup

Low-cost measurement pods, which we call pods, were equipped with Sensortech MiCS-2611 O_3 sensors and Maxdetect RHT03 temperature and humidity sensors. The pods are based on the Arduino UNO microcontroller and the Arduino programming language, and log data onto microSD cards. Collocation calibrations were completed during two separate weeks (before and after a 4-week field deployment) in July and August of 2014. The pods were placed on the roof of CAMP (Continuous Air Monitoring Project), a reference station maintained by the Colorado Department of Public Health and the Environment, in downtown Denver, CO (EPA Air Quality System Site Number 080310002). A Teledyne T400E UV absorption O_3 analyzer was used as an FEM reference instrument, and the pods were placed approximately 3 m below the inlet of the reference monitor. The average error for the Teledyne monitor ozone concentration measurements was -1.1% during the collocation period. Pods were powered and continuously running throughout both calibration periods.

4.2.2 Data Analysis

4.2.2.1 Ozone, Temperature & Relative Humidity Correlations

As mentioned above, the metal-oxide ozone sensors respond to temperature and humidity in addition to ozone, so it is important to include these parameters in calibrations. Figure 5.2 shows the correlations between reference ozone, MO_x ozone sensor signal (mV), temperature and humidity for Pod A. The correlation between the reference ozone and MO_x ozone is -0.87, which is reasonable, since the MO_x ozone voltage response is inversely proportional to ambient ozone. The correlation between the reference ozone concentration and temperature is 0.71, which is logical, since ozone is typically high when ambient temperatures are high. The correlation between the MO_x ozone sensor and temperature is smaller, at -0.52 (the negative sign is because the sensor response is inversely proportional to ambient ozone). The correlation between relative humidity and reference ozone concentration is -0.46, which implies that high relative humidity is inversely proportional to ambient ozone concentration, which is typically true, as relative humidity is usually highest when temperatures are low. The correlation between the MO_x ozone sensor signal and relative humidity is -0.44, which means that relative humidity has the opposite effect on the sensor signal than it has on ambient ozone concentration.

4.2.2.2 Data Preprocessing

The algorithms in this code were developed using the sci-kit learn, SciPy, and NumPy libraries in Python (Jones et al., 01 ; Pedregosa et al., 2011). Before analyzing the data, we completed several preprocessing steps. First, we removed any outliers that were clearly machine error. Next, we applied a finite impulse response filter to the reference and pod ozone data, for intervals of 5, 10, and 20 minutes, but ultimately found that better models were produced with no smoothing. The data were prescaled in two steps - first to a range between zero and one, then to zero mean and unit variance.

After scaling the data, it is split into half-day long chunks, and three of these chunks were

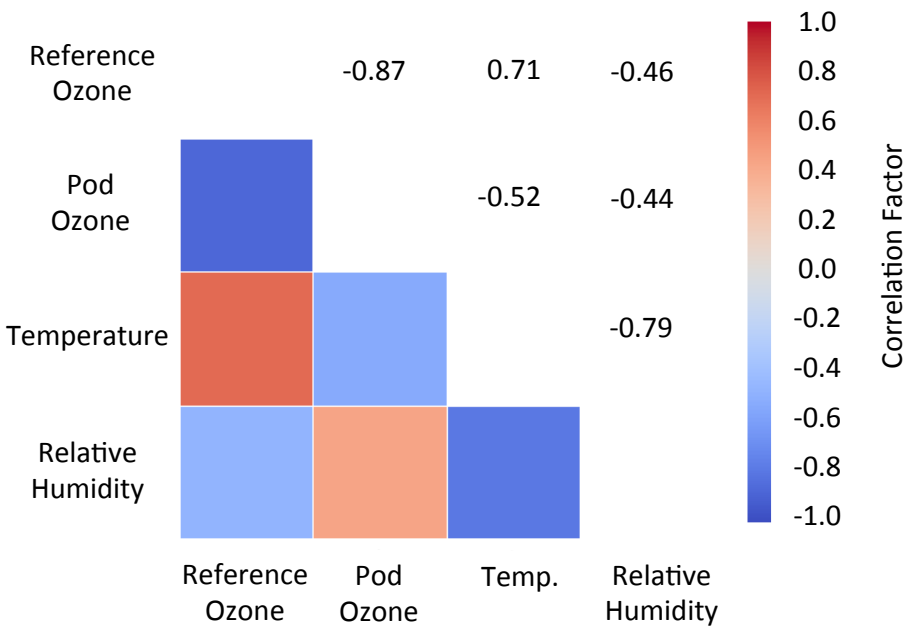

Figure 4.1: The visualization above shows the correlations between reference ozone, metal-oxide ozone sensor signal, temperature and humidity..

randomly selected to use as holdout data. The rest of the data were used as a training set. We chose to split data into chunks to prevent leakage of information from the training set to the cross-validation set. The first and last 90-minutes of data for each training and holdout set were removed to prevent contamination via the time-series features. The holdout data represents at least 15% of each dataset. To aid in model selection, we used a custom cross-validation set, where one half-day of data at a time was held out. Final model evaluations are based on the true holdout set.

4.2.2.3 Linear Regression

Linear regression assumes that the relationship between a predictor and response variable is approximately linear, and because of its simplicity, it is a good jumping off point when developing a regression model (Gareth et al., 2013). Additionally, we have found in previous studies that linear regressions perform similarly to more complex calibration functions for MOx sensors (Piedrahita et al., 2014a). The first step in this analysis was to perform simple linear regressions with the

measured (base) features (raw metal-oxide ozone sensor signal, temperature, and humidity).

Figure **??** is a comparison between the ozone values predicted by a linear regression model, using the data from the low-cost sensors, and the ozone values measured by a reference instrument. The root-mean-square error (RMSE) for this regression is 6 ppb, which means that the mean difference between the reference ozone concentration measurements and the model predictions is 6 ppb. This RMSE seems good, especially when you consider the fact that we're comparing the performance of a metal-oxide sensor to a reference instrument that uses UV photometry. However, when you look at Figure **??**, you can see that at high ozone values (¿ 50 ppb), the model significantly underpredicts ozone (by an average of 10.4 ppb, with an RMSE of 11 ppb). Since exposure to high ozone concentrations can negatively impact health, it is critical to measure high concentrations accurately. Improving these high-value measurements without compromising overall accuracy was a goal of this work.

Figure 4.3 shows the distribution of the predicted and reference data. The blue lines represent how the data would look if it were perfectly normally distributed, and examining the actual data distribution in the bins shows us that the scaled data was approximately normally distributed.

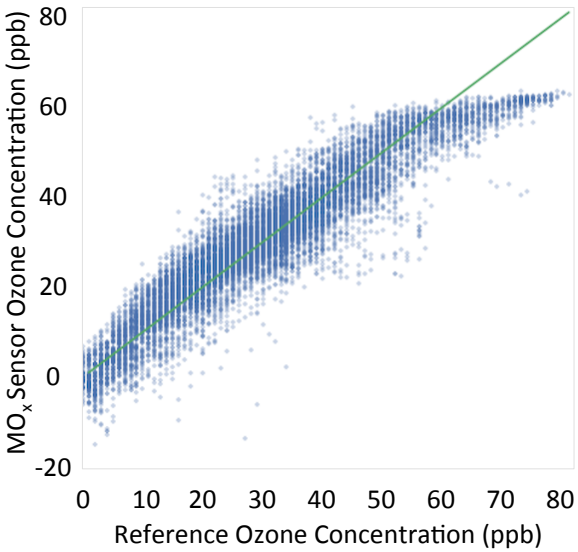

Figure 4.2: The plot above shows the results of a linear regression model created using the measured features (2b ozone sensor voltage signal, temperature, and humidity).

Figure 4.3(b) shows the distribution of the reference data. There was an abrupt cutoff at a concentration of zero, since ozone concentration cannot be less than zero. Notice that when the ozone concentration was above 50 ppb, the bins match the normal distribution very closely. The ozone concentration predictions in Figure 4.3(a), on the other hand, abruptly drop off around 60 ppb, and there were no predicted concentrations above 65 ppb.

4.2.2.4 Learning Curves

When data is fit poorly, it is important to determine whether the data has more of a bias (underfitting) or variance (overfitting) problem before deciding how to proceed. In this work,

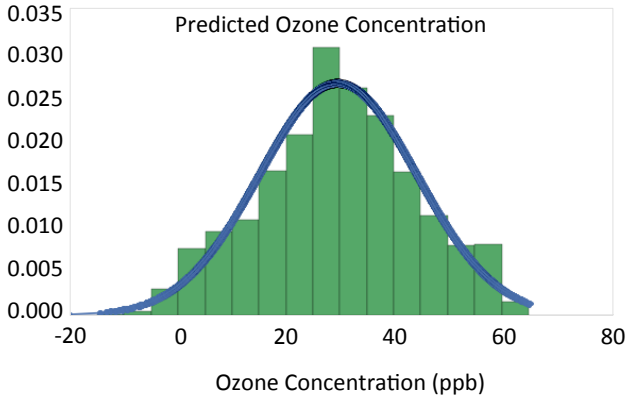

(a)

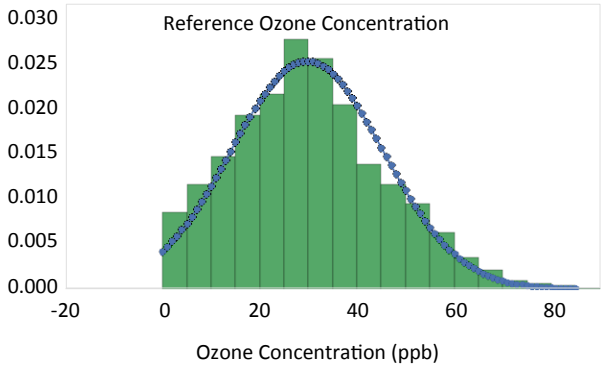

(b)

Figure 4.3: The figures below are histograms of the ozone concentrations measured by the reference and pod results (base features, linear regression). The concentrations measured by the pods (figure (a)) max out around 60 ppb, while the reference measurements (figure (b)) go up to 80 ppb.

learning curves were used to evaluate where each model lies in the bias-variance spectrum. Learning curves visualize how error (RMSE, in this case) for a cross-validation set and training set change as the number of training samples increases (Friedman et al., 2001). Figure 4.4 shows learning curves that indicate bias and variance problems. Figure 4.4(a) is a learning curve for a linear regression with the base features, and it indicates a bias problem. The training and cross-validation error converge at a somewhat high RMSE value. A model with a bias problem can be improved by acquiring additional features, adding polynomial effects, and/or decreasing the value of the shrinkage penalty. Figure 4.4(b), which is discussed in more detail below, shows a learning curve for a fit with high variance. As the number of samples increases, the gap between the training error and cross-validation error remains large. For a fit that suffers from high variance, measures that may improve the fit include reducing the number of features, increasing the shrinkage penalty, and/or acquiring more data.

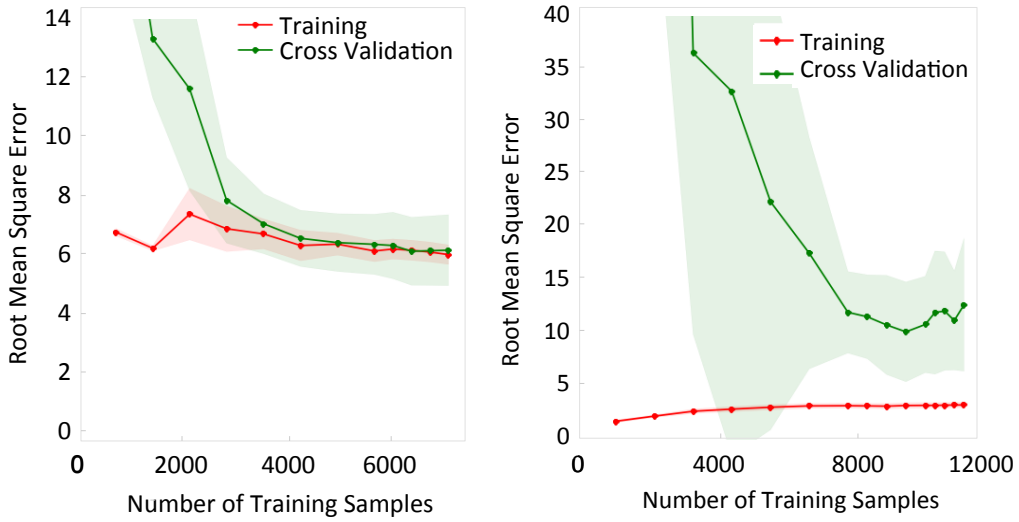

(a) (b)

Figure 4.4: The figures below are learning curves, which indicate bias and variance. Figure 2(a) indicates a bias problem. As the number of samples is increased, the training and cross-validation error converge at high values. Figure 2(b) shows a variance problem. As the number of samples increases, the gap between the training error and cross-validation error remains large.

4.2.2.5 Feature Engineering

Since the base features (ozone, temperature and relative humidity signals) result in a fit with high bias, additional features were created by transforming the base features; these included polynomial features (x_2, x_3, xy, x_2y_2, etc.), logarithmic features, and square root features. To characterize the time-series effects, we also created features representing the area under the ozone sensor signal curve, temperature curve, and humidity curve for 5, 15, 30, 45, 60, and 90 minutes before and after each data point. The slopes of the ozone, temperature and relative humidity curves for the time periods mentioned above were included as features. Next, we created interaction features for these curves, and also integral and slope features for the logarithmic base features.

After creating 320 additional features, learning curves were used to evaluate whether or not the additional features led to high variance. Figure 4.4(b) is an example of a fit that led to overfitting. This can be remedied by reducing the number of features used to create the fit. While the learning curves for some sensors in this study did not indicate indicate serious overfitting, finding the most important features is always advisable, as it is preferable to keep models as simple as possible without compromising accuracy. As complexity increases, fitting becomes more computationally expensive, and models become more difficult to interpret.

4.2.2.6 Forward-Stepwise Selection

Various methods (principal component analysis, best-subset selection, backward- and forward-stepwise selection) can be used to extract the most important features for a model. For this work, we started with forward-stepwise selection, as it provides a good balance between accuracy and computational expense. A forward-selection algorithm starts with the intercept, then adds the predictor that produces the best fit. Features are added sequentially, finding the best fit at each step (Friedman et al., 2001). Various scoring functions (R^2, mean-squared error, mean absolute error) can be used to evaluate the quality of a fit and aid in selecting the most important features. In this work, a custom error function was created to choose the best features. As mentioned in

Section 4.2.2.3, a linear model of the base features underestimates ozone at high values. The custom error function was designed to select features that optimize model fit at high values. Instead of using the standard equation for MSE,

$$MSE = \frac{1}{n}\sum_{i=1}^{n}(\hat{y}_i - y_i)^2, \tag{4.1}$$

where y_i are the reference values, $\hat{y}_i$ are the predicted values, and n is the number of samples, a custom error function was used.

$$error = \left|(C_{\mathrm{m,r}} - C_{\mathrm{m,p}}) - \sqrt{MSE_{\mathrm{high}} + 0.1\,MSE_{\mathrm{low}}}\right|, \tag{4.2}$$

where $C_{\mathrm{m,r}}$ is the median of the reference ozone data for high reference ozone concentrations (¿ 50ppb), $C_{\mathrm{m,p}}$ is the median of the predicted ozone data for high reference ozone, MSE_{high} is the mean squared error at high ozone values, and MSE_{low} is the mean squared error at low ozone values. The weights of MSE_{high} and MSE_{low} put ten times more emphasis on the MSE at high values than low values. The $C_{\mathrm{m,r}}$ minus $C_{\mathrm{m,p}}$ term penalizes under predictions.

Using this modified error function to select the most important features improved the fit at high values compared with the standard MSE function, without substantially increasing the overall MSE.

A common approach to choosing important features is to select the most parsimonious model which has error within one standard error of the minimum value (Friedman et al., 2001). Since a custom error function was used to select the best features, and we needed to evaluate each additional feature‘s effect on both the custom error and the overall RMSE, we did not use this method. Instead, at each step, a combination of the custom score, RMSE, and learning curves were used to evaluate whether or not to include additional features in the model.

Forward selection can reduce the error of a model and improve interpretability. However, since features are either kept or removed, it is a discrete process, and can sometimes lead to high variance, resulting in a model that does not have an improved prediction error (Friedman et al.,

2001). Shrinkage methods, which place a penalty on high coefficient values, are more continuous, and can reduce variance. In order to test whether forward selection or shrinkage methods result in the best model for the ozone data, all three methods were explored. The first shrinkage method applied was a ridge regression.

4.2.2.7 Ridge Regression

Ridge regressions are very similar to least squares regressions, and they minimize

$$\sum_{i=1}^{n}\left(y_i - \beta_0 - \sum_{j=1}^{p}\beta_j x_{ij}\right)^2 + \lambda\sum_{j=1}^{p}\beta_j^2. \tag{4.3}$$

where β_0 and β_j are the model coefficients, y_i are the observed values, and x_{ij} are the predictor (feature) values, and $\lambda \geq 0$ is a tuning parameter (Gareth et al., 2013; Hoerl, 1962). The sum on the left side of the equation is the residual sum of squares, and Equation 4.3 can be written as

$$RSS + \lambda\sum_{j=1}^{p}\beta_j^2. \tag{4.4}$$

A least squares regression computes coefficients $(\beta_0, \beta_1, ..., \beta_i)$ that minimize the RSS. The ridge regression adds a shrinkage penalty, $\lambda\sum_{j=1}^{p}\beta_j^2$, which penalizes large β values. The tuning parameter, λ, which represents the bias-variance trade off, balances the weight of these two terms. When $\lambda = 0$, the shrinkage penalty is zero, and the regression is equal to a least squares regression. When λ is very large, the RSS term becomes small in comparison with the shrinkage penalty, and the coefficient estimates approach zero. As the value of λ increases, the model flexibility decreases, which reduces variance but increases bias (Gareth et al., 2013). To choose the best λ value, the custom error was calculated (Equation 4.2) for a range of λ values. Our methods for choosing the best value for lambda are described below.

4.2.2.8 Lasso Method

The main disadvantage of ridge regressions for feature selection is that they include all of the original features in the final model. While the shrinkage penalty forces the coefficients toward zero as λ is increased, they will never reach zero (unless $\lambda = \infty$) (Gareth et al., 2013). This can make interpreting models very challenging. Tibshirani (1996) developed a method, called the Lasso, which overcomes this problem. The lasso coefficients, $\hat{\beta_\lambda^L}$, minimize

$$\sum_{i=1}^{n}\left(y_i - \beta_0 - \sum_{j=1}^{p}\beta_j x_{ij}\right)^2 + \lambda\sum_{j=1}^{p}|\beta_j| = RSS + \lambda\sum_{j=1}^{p}|\beta_j|. \tag{4.5}$$

The only difference between the equation for the ridge regression (equation 4.4) and the lasso (equation 4.5) is the replacement of the β_j^2 term with $|\beta_j|$ in the penalty. This changes the regularization penalty from type l_2 to l_1. l_2 penalties shrink the coefficient values of less important features, whereas l_1 penalties force the less-important coefficients to zero, yielding a sparse model. l_1 penalties are also easier to interpret, since they have fewer features. When most of the predictors in a model are important, l_2 penalties are better at minimizing prediction error than l_1 penalties, since they do not remove features from the model. On the other hand, when the model contains extraneous features, l_1 penalties produce better results, as they remove these features. Since the importance of each feature is never known a priori, the methods can be compared via cross validation (Gareth et al., 2013).

It is important to choose the shrinkage parameter, λ, wisely for both ridge and lasso regressions. Figure 4.5 consists of visualizations that aid in the selection of the lambda. The higher the value of lambda, the larger the penalty placed on high coefficient values. Figure 4.5(a) shows how the coefficients change as lambda is increased, and Figure 4.5(b) shows how the custom error function varies with lambda. The optimal lambda value is the one that results in the lowest error, and a different lambda value was chosen for each pod. The best lambda values ranged from 0.000003 to 3138.

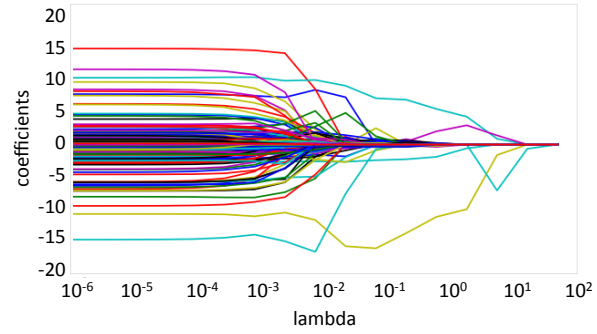

(a)

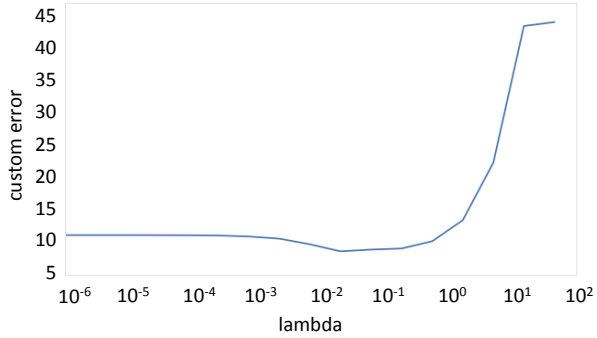

(b)

Figure 4.5: The plots below are visualizations that aid in the selection of the shrinkage parameter, lambda, for the lasso reduction method. The higher the value of lambda, the larger the penalty placed on high coefficient values. Plot (a) visualizes how the coefficients change as lambda is increased, and plot (b) shows how the custom error function varies with lambda. The optimal lambda value is the one that results in the lowest error.

4.2.3 Ensemble Regression Methods

4.2.3.1 Random Forests

Random forests are a tree-based ensemble method, which combines many randomized decision trees and outputs the mode of the mean predictions from all of the trees (Breiman, 2001). We applied random forests to the calibration data for five pods in this study, using all of the engineered features, as well as the best features chosen via forward selection. The models produced led to results with very high variance. Because the results were far inferior to those produced using the other methods mentioned in this paper, we chose not to apply random forests to the data for the

remaining pods. This poor performance is likely due to the fact that random forests often overfit noisy regression data. Additionally, while random forests are popular due to their ease of use and typical good performance, their results are difficult to interpret.

4.2.3.2 Support Vector Machines

Support Vector Machines (SVM) are a machine learning algorithms that can be used in classification and regression problems (Vapnik et al., 1996). SVMs are an extension of the idea of separating hyperplanes, which are linear boundaries that separate data into different categories (Friedman et al., 2001). Support Vector Machines for Regression (SVMR) work in a similar fashion to SVMs (Smola and Schölkopf, 2004).

To estimate the coefficients, β, in a linear model, linear SVMRs minimize the function,

$$\sum_{i=1}^{n} V(y_i - \hat{y_i}) + \frac{\lambda}{2}||\beta||^2, \tag{4.6}$$

where

$$V_\epsilon(r) = \begin{cases} 0 & \text{if } |r| < \epsilon, \\ |r| - \epsilon & \text{otherwise.} \end{cases}$$

r is the residual of a given data point, and $V_\epsilon(r)$ is an "ϵ-insensitive" error measure, which ignores errors smaller than the value of ϵ, and λ is a shrinkage parameter, similar to that of lasso and ridge regressions. In essence, linear SVMRs are similar to shrinkage methods, but they only consider data points with an error above some value, ϵ, in their minimization function. There are also non-linear generalizations of Support Vector Machines, the most common of which is the addition of a Gaussian Kernel.

In this work, models were generated using both linear and Gaussian SVMRs, and tried both methods with all of the generated features. A grid search was used to find the best value of ϵ for each metal-oxide sensor, and considered epsilon values of 0.1, 1, and 10.

4.3 Results

4.3.1 Model Performance

Linear regression, feature creation, forward selection, ridge and lasso regressions, random forests, and support vector machines were used to calibrate low-cost metal-oxide ozone sensors. The use of a linear regression model with the best features, selected from a set of generated features, substantially improved calibration accuracy. While the best features were selected using forward selection with a custom error function, standard linear regression was used to create a model with those features. For 75% of the pods, the best results were produced using a linear model with the best features extracted via forward-stepwise selection. For the other 25% of pods, the lasso regression method produced the best results. The cases that performed best with a lasso regression had learning curves that indicated high variance (at least 3 ppb difference between training and cross-validation RMSE for the 10 best features). The cases where linear regression with the best features was most accurate, on the other hand, had learning curves that did not indicate high variance for up to 15 features (¡ 2 ppb difference between training and cross-validation RMSE).

A comparison of the absolute differences between the medians of the reference and predicted data for the various methods employed in this study is shown in Figure 4.6. Ridge regressions produced inferior results to the methods above, probably because they have an l_2 regularization penalty, and do not reduce the number of features in a fit. SVMs, evaluated using all of the generated features, did not perform as well as the best methods. Like ridge regressions, SVMs have an l_2 regularization penalty. Since we generated a large number of features, many of which are not important, the lack of feature reduction in SVMs and ridge regressions led to overfitting. While SVM's emphasis on high-error data points can be good at reducing overall error, it does not place the same emphasis on high ozone-concentration value errors as the methods that allowed the use of the custom error function. This is an example of a case where the flexibility of simpler methods outweighs the power of more complex methods. Using the best features chosen by forward selection with ridge and lasso regressions and SVMs did not improve upon the forward selection results; the

Figure 4.6: The box plots below show the absolute difference in medians between the reference and pod ozone measurements for ambient ozone concentrations higher than 50 ppb. All of the methods shown below outperformed linear regressions with the base features. The box, labeled "Best (FS)" represents the outcomes of a linear regression with the best generated features, extracted using forward-stepwise selection. The "Best Overall" box represents the models determined to be the most accurate (best forward selection for 75% of pods and lasso for 25%). While switching 25% of the pods to the lasso model slightly increases the absolute median difference between the pod and reference measurements, it improved the RMSE for pods that had variance problems.

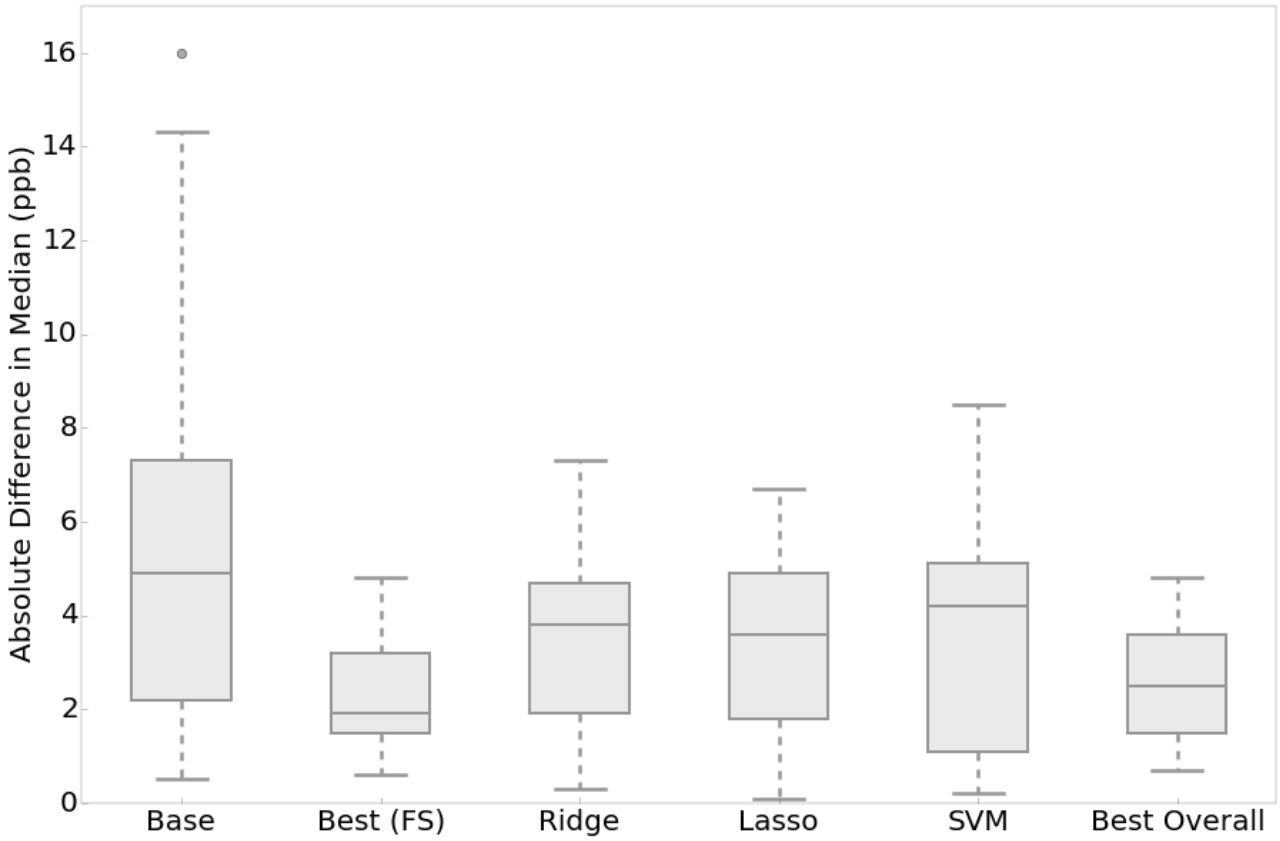

most important features were carefully chosen, so further reducing them did not improve the model.

Figure 4.7 compares results for ozone concentrations using a linear regression with the base features and when the best regression model is employed (linear with forward-stepwise selection or lasso). The performance metric used in Figure 4.7 is the absolute difference between the median high-ozone value (¿ 50ppb) for reference data and the and the median high-ozone value for predicted data. The linear model with base features produced differences in high ozone-concentration medians

of up to 16 ppb, with a median difference of 4.9 ppb, and standard deviation of 4.1 ppb. The largest absolute difference in high ozone-concentration median between the reference measurements and pods for the best regression model is 5 ppb, with a median of 2.5 ppb and standard deviation of 1.3 ppb.

To further demonstrate the performance of the various models for high ozone concentrations, we explored the RMSE for the model fits, using the holdout data. Figure 4.8(a) shows the high ozone-value RMSE for the base features and best features. The high ozone-value RMSE is reduced in 15 of the 16 pods. The median high ozone-value RMSE for the linear model with base features is 6 ppb, with a standard deviation of 3.7 ppb. The median and standard deviation of the RMSE values are reduced to 4 ppb and 1.1 ppb, respectively, when the best models are used.

The emphasis on improvements in the fit at high values did not lead to a less accurate model at lower values (see Figure 4.8(b)). Employing the best models rather than a linear regression with base features reduced the overall RMSE in 15 of the 16 pods. The median overall RMSE was reduced from 6 ppb to 5 ppb, and the standard deviation was reduced from 2.5 ppb to 1.6 ppb.

For four weeks between collocation calibration studies, the pods were deployed across a 10 km by 10 km region in Erie, CO. Pod P, however, was located at the collocation site for twenty days. This relatively large dataset enabled us to evaluate the model on a larger holdout set. Figure 4.9 shows the results from holding out the first and last five days of data, and using the middle 10 days of data to train the model. Figure 4.9(b), which represents the holdout data, with the best-features linear model applied, shows a substantial improvement over the base model (Figure 4.9(a)). The overall RMSE, high ozone concentration RMSE, and high ozone value median difference were reduced from 9 ppb to 4 ppb, 8 ppb to 3 ppb, and 8 ppb to 2.5 ppb, respectively, by using the best models instead of a linear regression with the base features.

From July 22nd to August 20th, 2014, Pod I was at the Boulder Atmospheric Observatory, and was approximately 50 m from an FEM ozone monitor (2b Technologies Model 202). The FEM monitor was at a height of 10 m, and the pod was at a height of 1.5 m. Due to imperfect mixing and dry deposition, the ozone concentrations measured at the two heights can not be expected to

Figure 4.7: This slopegraph shows how the difference between the medians of high-ozone values (> 50 ppb) measured by the reference instrument and the pods changes when the regression model is changed from linear with the base features (pod ozone sensor signal, temperature, relative humidity) to a linear model with the best created features.

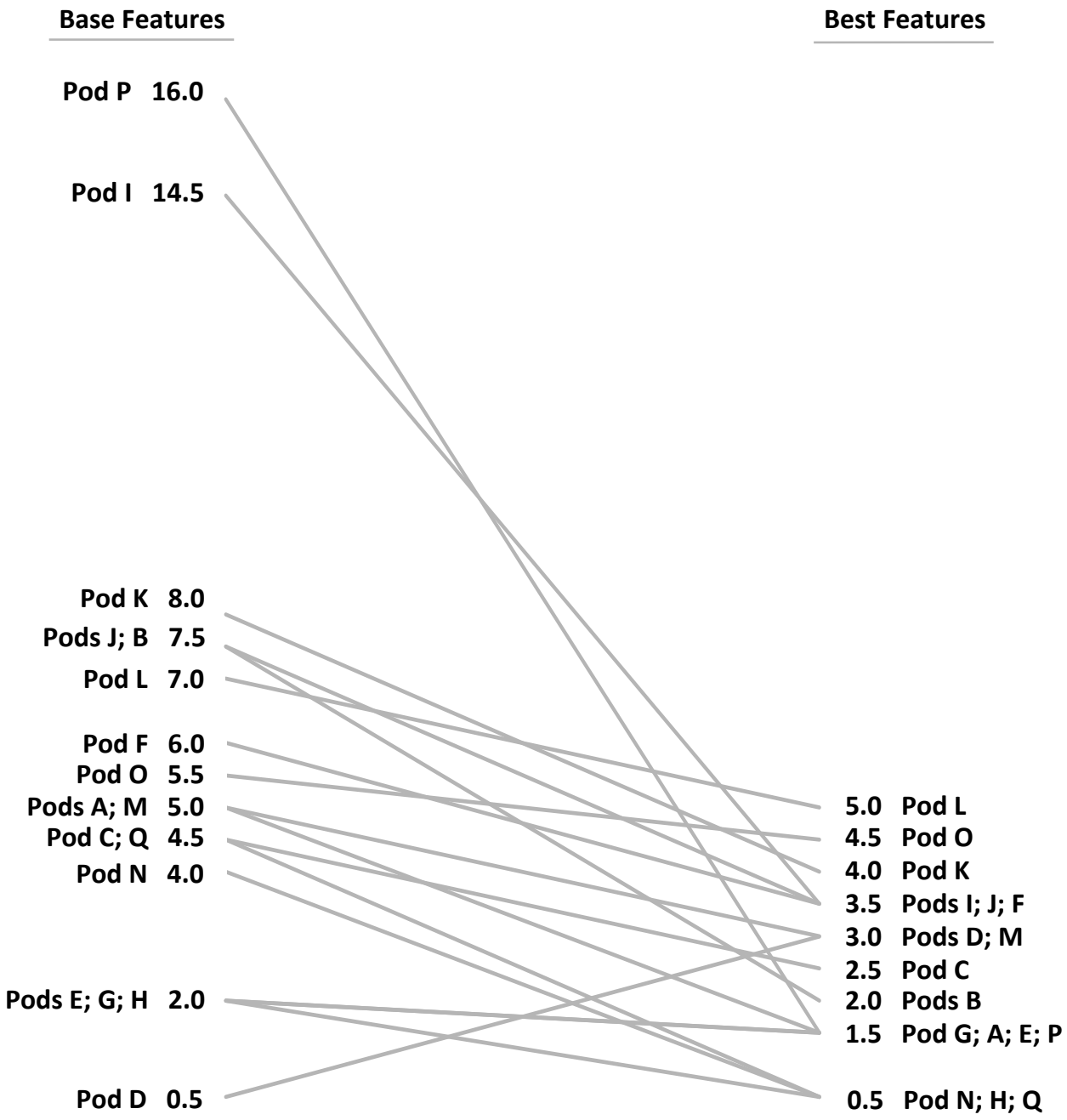

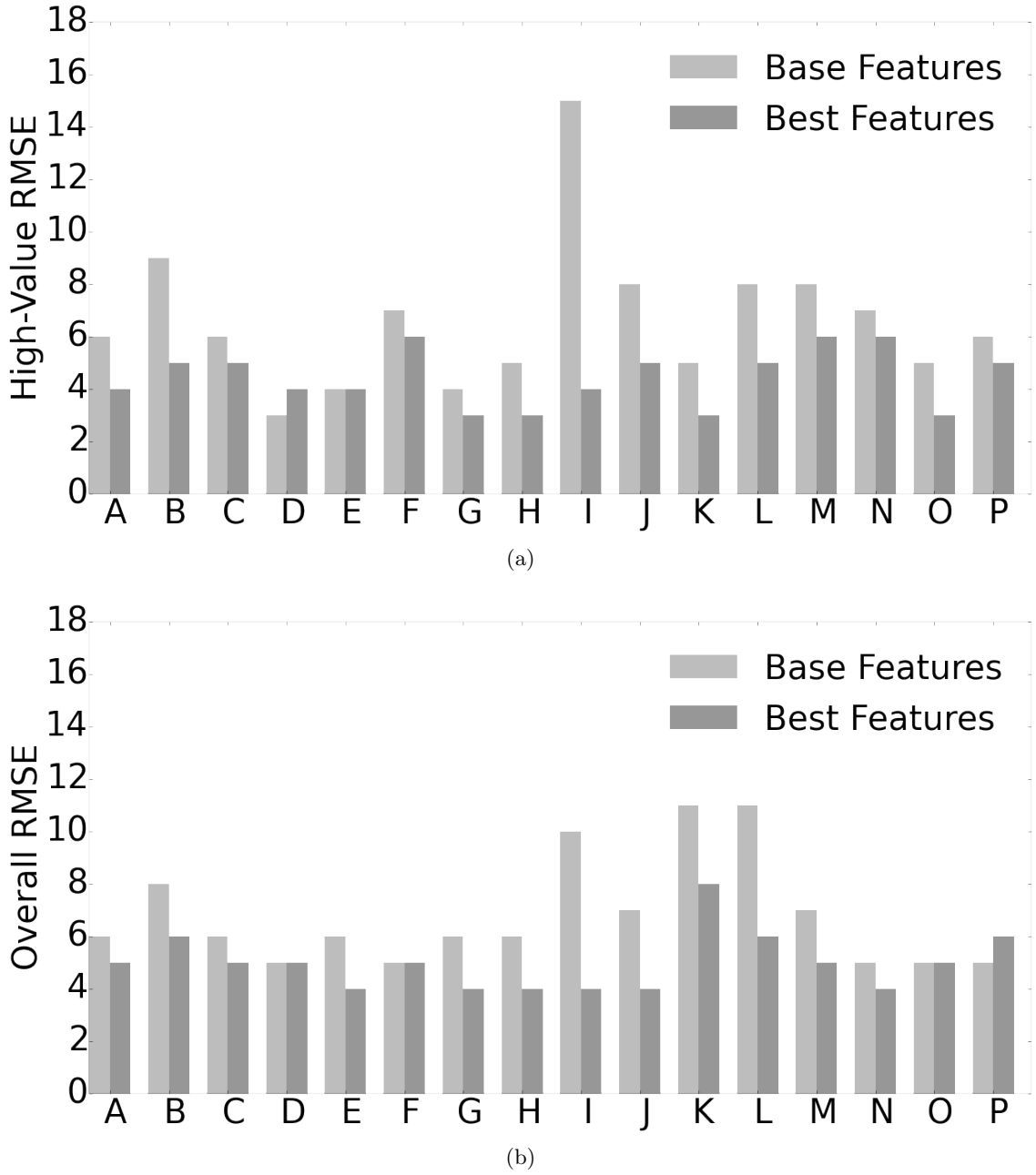

(a)

(b)

Figure 4.8: The bar graphs below show the high-value (¿ 50 ppb) RMSE and overall RMSE for holdout data for linear models using the base features and best created features.

be exactly equal, but the concentrations should be similar, and comparing them is an interesting exercise for contrasting the different models. Figure 4.10 shows a comparison of the FEM ozone data, and the pod data, using the base calibration model and the best model described above. The

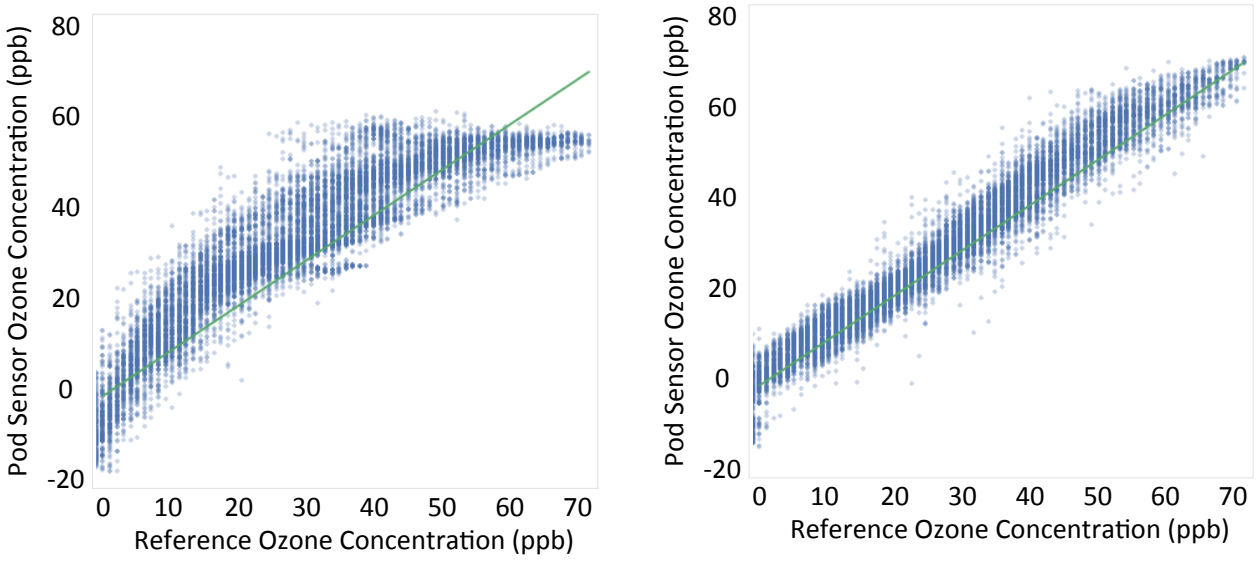

Figure 4.9: The plots above show how reference and pod ozone measurements compare for Pod P. Twenty days of data were collected, and the first and last five days were used as holdout data, which is the data shown here. Plot (a) shows the results of a linear model with the base features (pod MO_x ozone senzor voltage, temperature, and relative humidity). Plot (b) shows the results of a linear model with the best generated features extracted using forward stepwise selection. The green lines represent a one-to-one fit.

best features model consistently provides higher estimates of daily peak ozone values than the base model, and provides concentration estimates very close to those measured by the FEM monitor.

When the ambient ozone concentration is greater than approximately 75 ppb, the pod predicts lower concentrations than the FEM monitor. While this could be due to the difference in measurement height, it is likely that, even with the improved model, the pod is still slightly underpredicting the highest ozone concentrations. The training data for this pod, which were gathered during the collocation calibration, were all at concentrations below 75 ppb. This highlights the importance of calibrating the pods using data that contains the highest ozone values the pods could encounter during deployments. This is a limitation of using collocation calibrations; we cannot control atmospheric conditions, and it is probable that peak ozone values will not occur during ambient-environment calibrations. Future work should combine real-world collocation data with

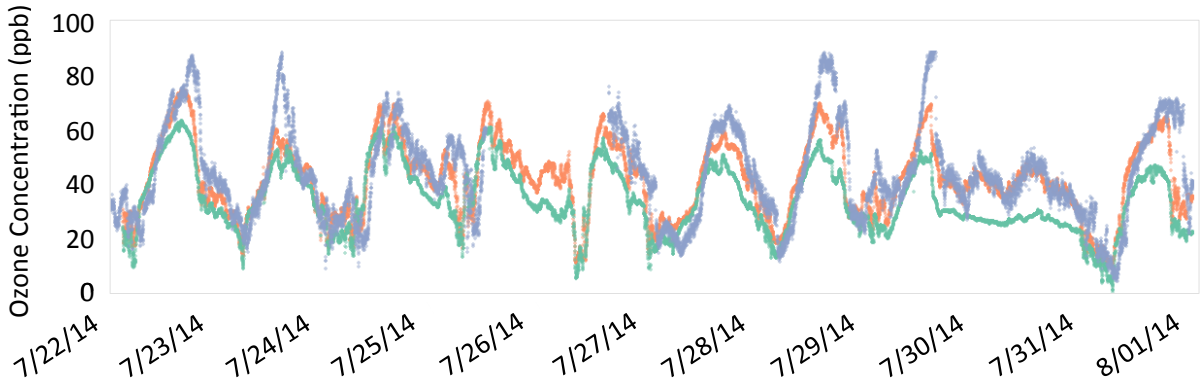

(a)

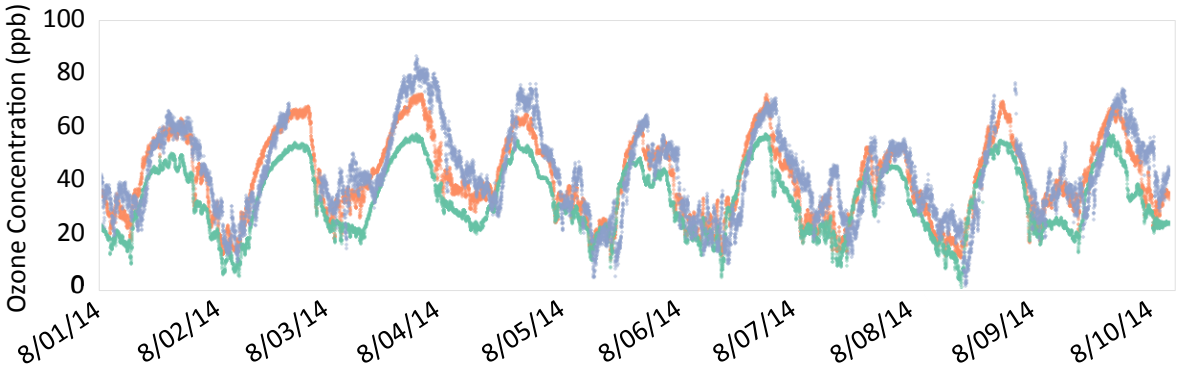

(b)

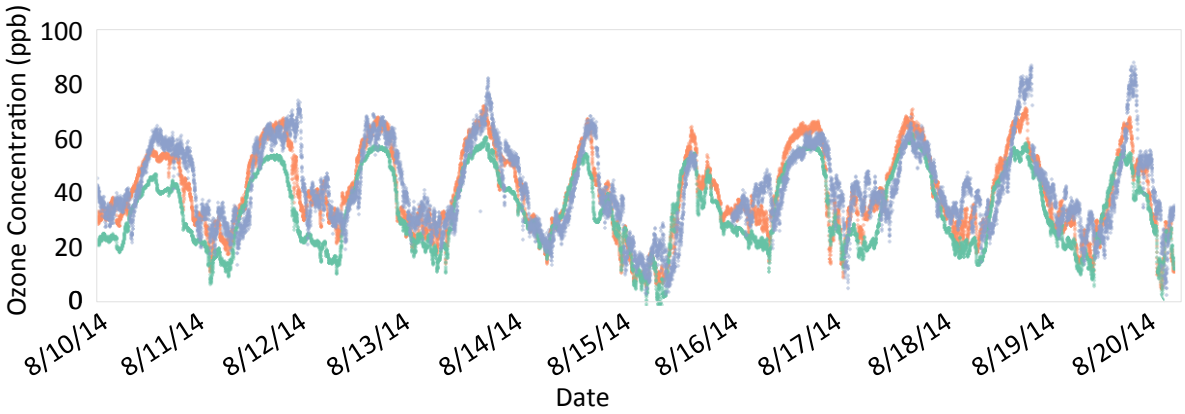

(c)

Figure 4.10: The plots above show ambient ozone, measured by a Pod I, first calibrated using a linear model with the base features (green), then a linear model with the best features (orange), and finally a nearby FEM ozone monitor (purple).

laboratory calibrations that represent the entire range of ozone values that could be observed during a deployment, with emphasis on high values.

4.3.2 Implications of the Most Important Features

Table 4.1 lists the features that appeared in the "best features" list for four or more of the 16 pods. The most common feature, $\int_{t}^{t+5} \ln(V_{O_3})$, was important in 75% of the pods. V_{O_3} is the raw voltage reading from the MO_x ozone sensor, and the fact that it is in natural log form means that it emphasizes low values of V_{O_3}. The ozone sensor response is inversely proportional to ambient ozone concentration, so low V_{O_3} equate to high ozone. The feature looks at the integral over the 5 minutes after the reading, which could imply a slower response to ozone changes from the MO_x sensor than the reference instruments, and/or act as a smoothing mechanism.

The next most common important feature is T^3, which was important for 56% of pods. Cubing a feature emphasizes high values, and ambient ozone is typically high when temperatures are high, so this effectively emphasizes periods of high ozone. Next is $V_{O_3}^2 T^2$ (important for 56% of pods), which looks at the interaction between $V_{O_3}^2$ and T^2. The sensitivity of MO_x sensors changes with ambient temperature, so it is not surprising that an interaction term between sensor signal and temperature is important (Masson et al., 2015; Piedrahita et al., 2014a). Additionally, response can vary from sensor to sensor (Romain and Nicolas, 2010). Because the features are squared, they both emphasize high values. The next most important feature is $\ln(V_{O_3})$ (56% of pods), which emphasizes low V_{O_3} (high ambient ozone) values. n_{days}, which is the number of days since the start of the first calibration, was important for 31% of the pods, and represents sensor drift. $V_{O_3}^2 RH^2$ (31% of the pods) represents the interaction between $V_{O_3}^2$ and RH^2. As mentioned in section 4.2.2.1, relative humidity has the opposite effect on the sensor signal that it has on ambient ozone concentration, so considering the combination of the two signals is insightful. $\int_{t-90}^{t} \ln(T)$ (31% of the pods) represents the area under the natural log temperature curve for 90 minutes before the data point being analyzed. The natural log term emphasizes low temperature values. This term implies that the sensor's response to temperature is important for 90 minutes.

Table 4.1: The features which appear in the "best features" list for at least four pods are listed below.

Feature Number	Feature	Number of Pods
1	$\int_t^{t+5} \ln\left(V_{\mathrm{O_3}}\right)$	12
2	T^3	9
3	$V_{\mathrm{O_3}}^2\, T^2$	6
4	$\ln\left(V_{\mathrm{O_3}}\right)$	6
5	n_{days}	5
6	$V_{\mathrm{O_3}}^2\, RH^2$	5
7	$\int_{t-90}^{t} \ln\left(T\right)$	5
8	$\left(\int_t^{t+5} \ln\left(V_{\mathrm{O_3}}\right)\right)\left(\int_t^{t+5} \ln(RH)\right)$	4
9	$\int_t^{t+5} V_{\mathrm{O_3}}$	4
10	RH^3	4
11	$\left(\frac{V_{\mathrm{O_3,t}} - V_{\mathrm{O_3,t-90}}}{90}\right)\left(\frac{T_{\mathrm{t}} - T_{\mathrm{t-90}}}{90}\right)$	4

Features that are important for 25% of the pods include $\left(\int_t^{t+5} \ln\left(V_{\mathrm{O_3}}\right)\right)\left(\int_t^{t+5} \ln(RH)\right)$, $\int_t^{t+5} V_{\mathrm{O_3}}$, RH^3, and $\left(\frac{V_{\mathrm{O_3,t}} - V_{\mathrm{O_3,t-90}}}{90}\right)\left(\frac{T_{\mathrm{t}} - T_{\mathrm{t-90}}}{90}\right)$. The meanings of the first three features are similar to the features discussed above. $\left(\frac{V_{\mathrm{O_3,t}} - V_{\mathrm{O_3,t-90}}}{90}\right)\left(\frac{T_{\mathrm{t}} - T_{\mathrm{t-90}}}{90}\right)$ looks at the interaction between the change in ozone sensor signal for 90 minutes before the data point being analyzed and the change in temperature during the same time period.

4.4 Conclusions

Creating a large number of features, which leverage time-series data, as well as feature interactions between the $\mathrm{MO_x}$ ozone sensor, temperature, and relative humidity, then extracting the

best features led to substantial improvements in pod ozone measurements when ambient concentrations are high. When learning curves did not indicate overfitting (75% of pods), forward stepwise selection of the best features, using a custom error function, followed by linear regression with the best features yielded the best results of the methods discussed in this work. When learning curves indicated overfitting (25% of pods), extracting important features using the lasso method with a custom error function produced the most accurate model.

These relatively simple methods of developing models outperformed the more complex methods, Random Forests and Support Vector Machines. The poor performance of Random Forests was probably due to the fact that the random forest algorithm could not be customized to emphasize high ozone concentrations. Like Random Forests, Support Vector Machines could not be customized to emphasize high ozone concentrations. Also, SVMs do not reduce the number of features in a fit, which can led to overfitting. The same is true of ridge regressions. While sophisticated algorithms can be very powerful, they often lack the flexibility of their simpler predecessors, which, in this case, meant that the simpler methods produced better models.

While the modeling in this work drastically improved our calibration results, sensors underpredicted ozone values that were higher than those seen during collocation calibrations. We recommend that future studies combine collocation calibrations, which represent real-world conditions, with laboratory calibrations that include exposure to the highest ozone concentrations that could be encountered in the field.

Finally, an inspection of the most important features across all 16 pods revealed that the area under the natural log of the ozone signal, for five minutes after the data point being evaluated, is the most important feature in creating an accurate model. Two of the eleven most common features included temperature for ninety minutes before the data point being considered, which indicates that the changes in temperature can affect the sensor signal for 90 minutes. Interaction terms between ozone signal and both relative humidity or temperature were important, reaffirming that both environmental conditions affect the sensor signal. Future laboratory experiments, where one of the three conditions (ozone concentration, temperature and humidity) is changed at a time

could improve understanding of these results and sensor response.

Chapter 5

Front Range Air Pollution and Photochemistry Experiment (FRAPPE)

Summertime ozone concentrations in the Northern Front-Range Metropolitan Area (NFRMA) of Colorado frequently exceed the National Ambient Air Quality Standards (NAAQS). Atmospheric modeling in the NFRMA is challenging due to the complex topography of the area, as well as the diversity of pollutant sources (urban NO_x and VOCs, power plants, oil and gas, agricultural emissions, biogenic emissions, and wildfires). Modeling boundary-layer O_3 deposition is challenging, and varies spatially due to micrometeorology, variation in ambient concentration, and ecosystem productivity. Model grid cells typically range in size from 10 to 100 km and 100 to 500 km, for regional and global models, respectively, and accurate representations of an entire grid cell cannot always be achieved. Large spatial variability within the grid cells of these models contributes to poor estimates of trace-gas flux and concentration.

5.1 Methods

To address this issue, I used dynamic flux chambers with low-cost metal-oxide ozone sensors to explore the spatial variability in ozone concentration and dry deposition during the Front Range Air Pollution and Photochemistry Experiment (FRAPPE). The experiment consisted of three flux chambers, and collected 720 hours of data for each chamber. All three chambers were within a 8.3 x 6 km square. One chamber was in the same location as the Boulder Atmospheric Observatory (BAO) tower, and was connected to a 2B Technologies Ozone Monitor. The other two chambers were at distances of 3.22 and 7.55 km from the tower. The largest distance between any two

chambers was 8.5 km. All three chambers measured flux onto native grasslands across a range of natural variability in species and ecosystem productivity.

Collocation calibrations were performed during the study, as previous deployments have revealed that they provide more accurate concentration estimates than laboratory calibrations because they expose the sensors to real-world ambient conditions (Piedrahita et al., 2014a). This was the most challenging aspect of the study. As mentioned in Chapter 3, MO_x sensors respond to changes in ambient temperature and relative humidity, and their output is non-linear with respect to gas concentration (Barsan and Weimar, 2001; Delpha et al., 1999; Marco, 2014; Masson et al., 2015; Piedrahita et al., 2014a; Romain et al., 1997; Sohn et al., 2008). Additionally, response can vary from sensor to sensor (Romain and Nicolas, 2010). Calibrating metal-oxide sensors for use in flux chambers is even more challenging than for ambient measurements since the opening and closing of the chamber lid leads to rapid changes in temperature and humidity.

One of the chambers was equipped with both MO_x sensors and a 2B Technologies Ozone Monitor for the entire study. This enabled us to compare the flux results from the MO_x sensors and 2B ozone monitor for the entire duration of the study.

5.2 Results

5.2.1 Environmental Conditions in the Chambers

Figures 5.1e and 5.1f show the temperatures in the pod for one measurement cycle in the afternoon and one in the middle of the night, when ozone concentrations are high and low, respectively. In both cases, the temperature rises after the chamber lid closes. During the day, the increase in temperature is likely caused by solar radiation. However, the temperature also increases in the pod in the middle of the night, so there must be another source of heat. The chamber operates by pulling air into the pod from the outlet of the chamber, and this air is constantly cycled through the pod at $5\,\mathrm{L\,min^{-1}}$. A larger pump pulls air at $80\text{-}90\,\mathrm{L\,min^{-1}}$ from the same outlet. It is likely that the increase in temperature in the pod is related to the increase in pressure drop

that results from closing the chamber. The volumetric flow rate to the pod is likely reduced as a result of this increase in pressure drop, which reduces the rate at which the heat produced by the electronics is removed. Regardless of the cause of the rise in temperature, it affects the sensitivity of the ozone sensor.

Figures 5.1g and 5.1h show the absolute humidity during the afternoon and in the middle of the night, respectively. During the day, the relative humidity in the chamber increases when the lid closes, which is due to the evapotranspiration of the vegetation in the chamber. However, even in the middle of the night, when there is no evapotranspiration, the relative humidity in the chamber drops slightly when the lid closes. This is likely due to the increase in temperature, and does not reflect a change in absolute humidity.

Figures 5.1a and 5.1b show how the raw voltage data from the ozone sensor changes during a measurement cycle. During the day (Figure 5.1a), the raw signal increases during the chamber closure. Since the sensor response is inversely proportional to ozone concentration, this is the expected result. At night (Figure 5.1b), the sensor signal is approximately constant. The fact that the change in ozone concentration is much smaller at night than during the day (50%, in this case) contributes to this, but the response to temperature and humidity also affects the signal. Figure 5.2 shows the correlations between sensor signal, ozone concentration, temperature and humidity. Decreasing ozone and relative humidity are correlated with increasing sensor signal (labeled "pod ozone" in the plot), but increasing temperature is correlated with a increase in sensor signal. These effects are likely canceling out the response to change in ozone concentration, which is why it is important to consider temperature and humidity in calibrations. These relationships are explained in more detail in Section 2.2.1 of Chapter 3.

5.2.2 Flux Measurements with 2B Ozone Monitor

Flux data measured by Chamber 2 (at the BAO Tower) with the 2B Technologies Ozone Monitor, between July 18th and August 12th, 2014 is shown in Figure 5.3. Peak daily O_3 flux rates occurred between 15:00 and 18:00 and had values of 0.2 to 0.5 $\mu g\, m^{-2}\, s^{-2}$. Minimum daily O_3

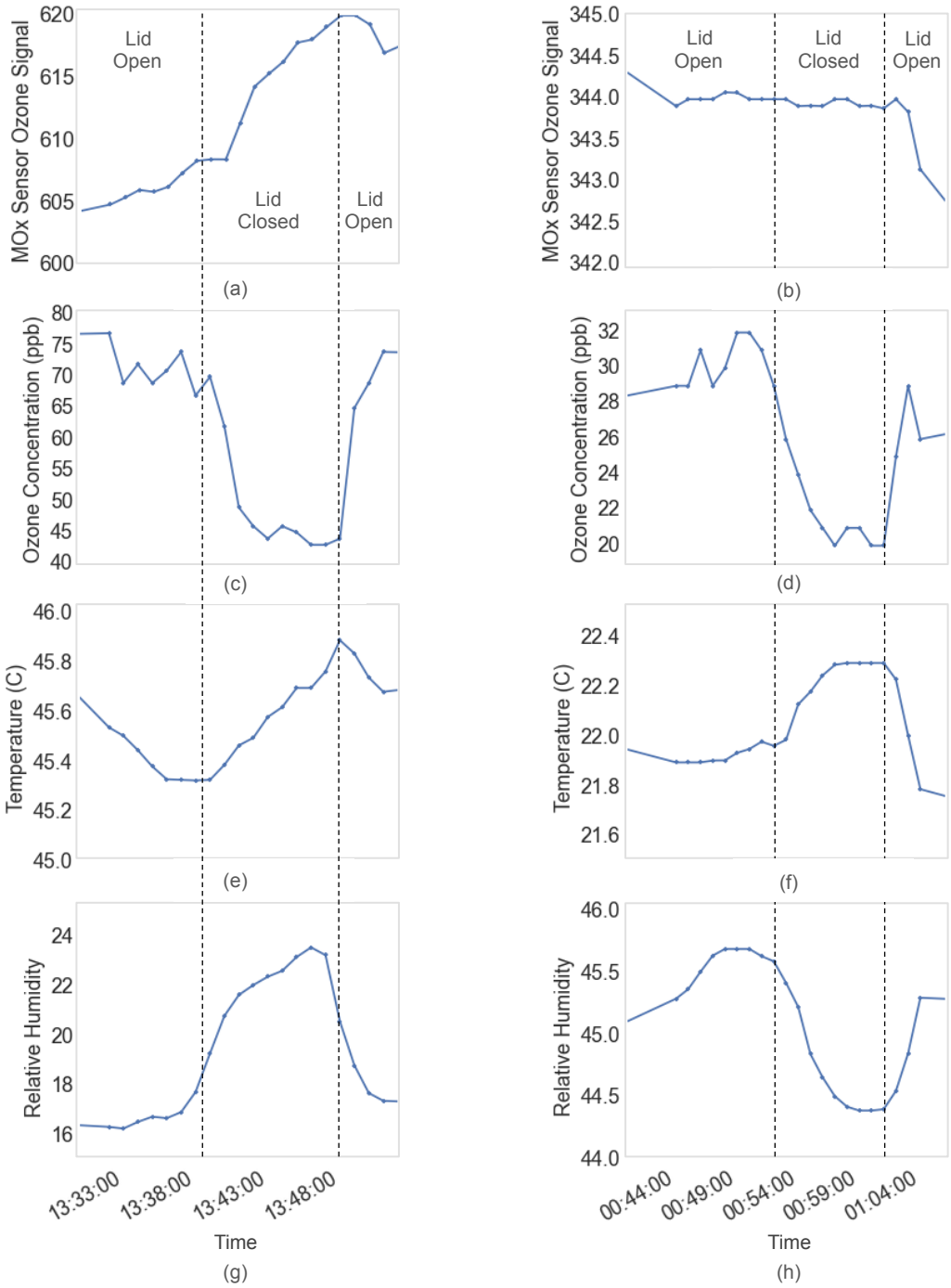

Figure 5.1: The figure above shows the MO_x sensor signal, ozone concentration, temperature, and relative humidity in the pod for one measurement cycle in the afternoon ((a), (c), (e), (g)) and one in the middle of the night ((b), (d), (f), (h)), when ozone concentrations are high and low, respectively.

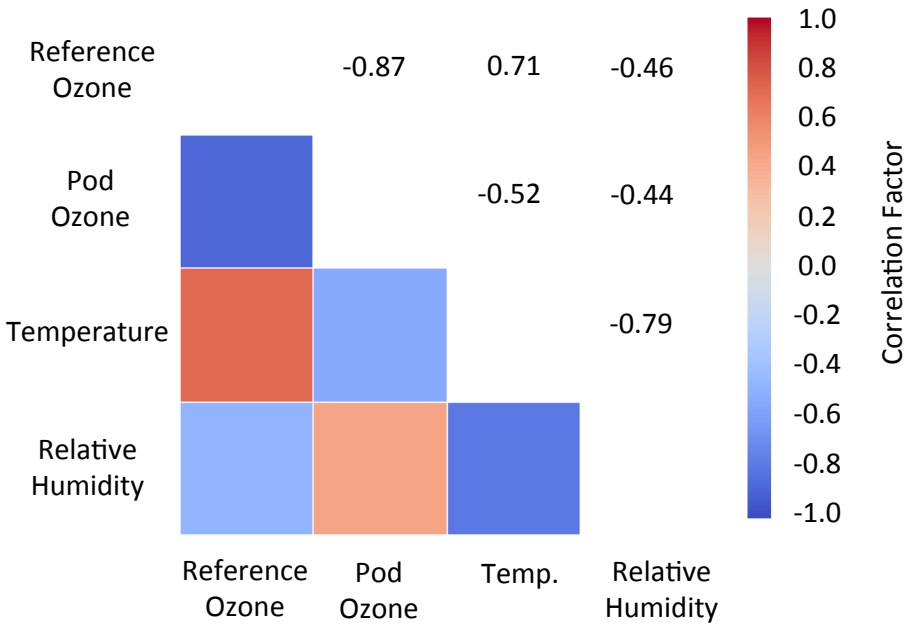

Figure 5.2: The matrix above show correlations between sensor signal, ozone concentration, temperature and humidity.

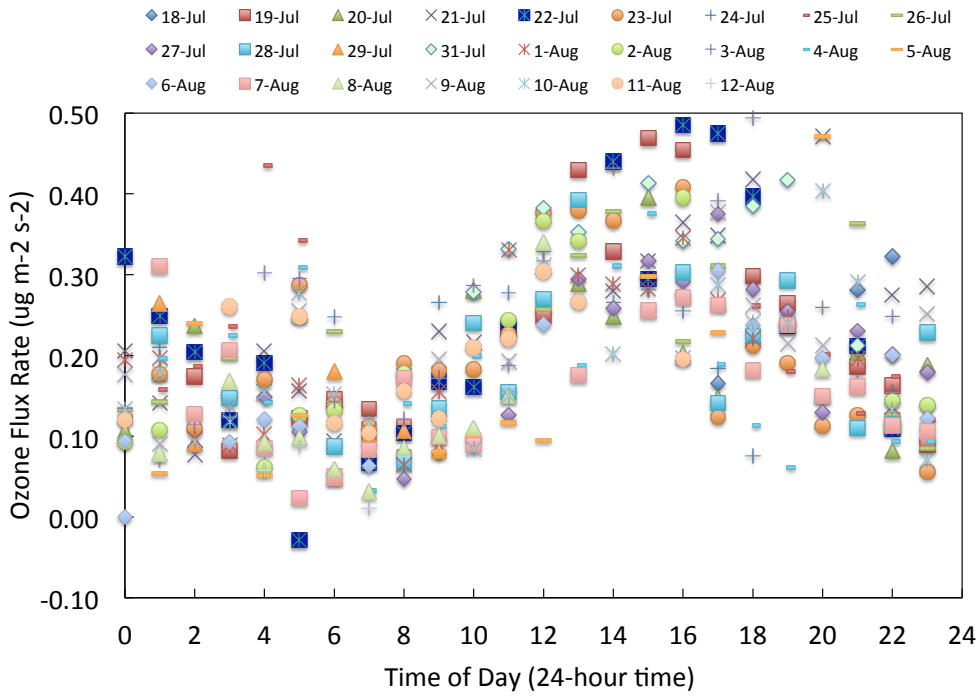

Figure 5.3: The figure above shows flux data measured by Chamber 2 (at the BAO Tower) with a 2B Technologies Ozone Monitor.

flux rates occurred between 5:00 and 7:00, and had values of -0.05 to 0.25 $\mu g\,m^{-2}\,s^{-2}$. Flux rates followed a similar trend for most days, with a few outliers.

5.2.3 Sensor Calibration

I used the regression techniques described in Section 2 of Chapter 3 to calibrate the MO_x ozone sensors in the chambers. Figure 5.4 shows the ozone concentrations measured by the MO_x ozone sensors in chamber 2 on August 3rd and 4th, 2014. Data from eight minutes before the lid closure and eleven minutes after were used to calibrate the sensor. The reference ozone concentration during these periods decreases, which reflects the deposition of ozone. The ozone concentration measured by the MO_x sensors, on the other hand, stays relatively constant during each chamber closure. This is due to poor calibration results, which are caused by the rapid changes in relative humidity and temperature after the closure of the chamber lid.

I resolved this problem by developing two separate calibration models – one for the last eight minutes before the chamber closed, and one for the last three minutes the chamber was closed before reopening. Figure 5.5 shows the results of this dual calibration method for chamber 3. The solid pink and purple lines represent reference measurements from the 2B ozone monitor for when the chamber was open and closed, respectively. The orange and green dashed lines represent MO_x ozone sensor measurements for when the chamber is open and closed, respectively.

This method results in a much better match between the measurements from the MO_x ozone sensors and the 2B Ozone monitor. While the concentrations do not always match perfectly, they follow the same trends, and the difference between the open and closed values is similar.

5.2.4 Comparison of 2B Ozone Monitor and MO_x Sensor Results

Figure 5.6 compares between flux rates measured by Chamber 2, using the 2B ozone monitor and MO_x sensor from July 28th to August 11th, 2014. While the data loosely follow a one-to-one trend, they are very spread out, and have a low correlation ($R^2 = 0.1$). Because of this poor fit, the measurements acquired using the flux chambers and the MO_x sensors cannot be

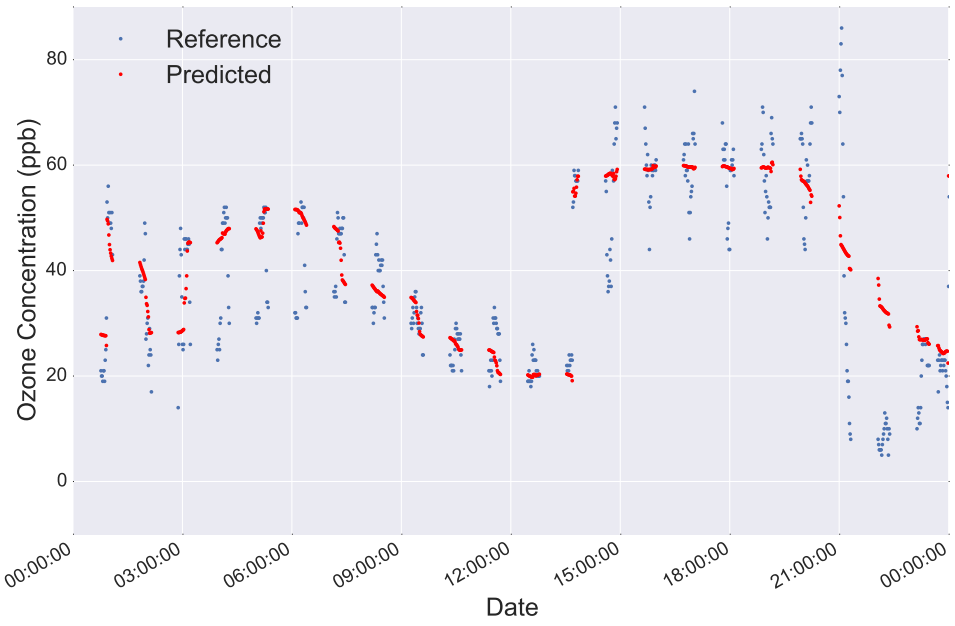

Figure 5.4: This plot shows the ozone concentrations measured by the MO_x ozone sensors in chamber 2 on August 3rd and 4th, 2014, using a single regression model.

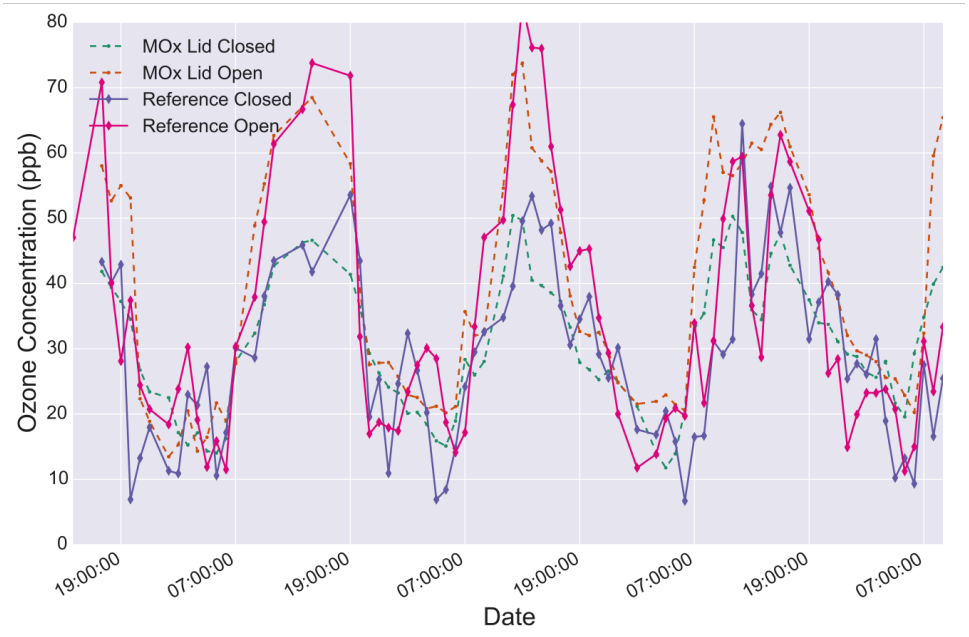

Figure 5.5: This plot shows the ozone concentrations measured by the MO_x ozone sensors and 2B Ozone Monitor with chamber 3 from July 26th through August 1st, 2014, using one regression model for when the chamber lid was open, and a separate model for when the chamber lid was closed.

considered reliable for hourly measurements. The MO_x sensors performed much better for time-averaged measurements. For the 15-day period studied, the mean flux rate measured by the MO_x sensors was -0.23 $\mu g\,m^{-2}\,s^{-1}$, which is a 21% overestimation of the flux measured by the 2B ozone monitor (0.19 $\mu g\,m^{-2}\,s^{-1}$). The source of much of this error is a 110% overestimation of fluxes at ambient ozone concentrations below 20 ppb, when flux measurement uncertainty is highest. For ambient ozone concentrations above 20 ppb, the MO_x sensor measurements only exceeded the 2B flux measurements by 14%.

5.2.5 Spatial Variability Results

Figure 5.7 shows ozone concentrations measured by Chamber 1 using the MO_x ozone sensors at the Erie Private Airport between July 26th and August 1st, 2014. Average afternoon ozone concentrations at the airport were about 10 ppb lower than those at the BAO tower. Figure 5.8 shows chamber measurements of ozone, measured by Chamber 3 at Frederick High School in Frederick, CO between July 26th and August 1st, 2014.

The average flux ozone flux values between August 1st and 6th, 2014 for Chambers 1, 2, and 3 (Erie Airport, BAO Tower, and Frederick High School) were 0.21 $\mu g\,m^{-2}\,s^{-1}$, 0.28 $\mu g\,m^{-2}\,s^{-1}$, and 0.18 $\mu g\,m^{-2}\,s^{-1}$, respectively. Ambient ozone concentrations at the BAO Tower were up to 20 ppb higher than Frederick High, which supports the lower flux rate. Given these results, we can conclude that low-cost flux chambers with MO_x ozone sensors can be used to measure time-averaged spatial variability in ozone flux.

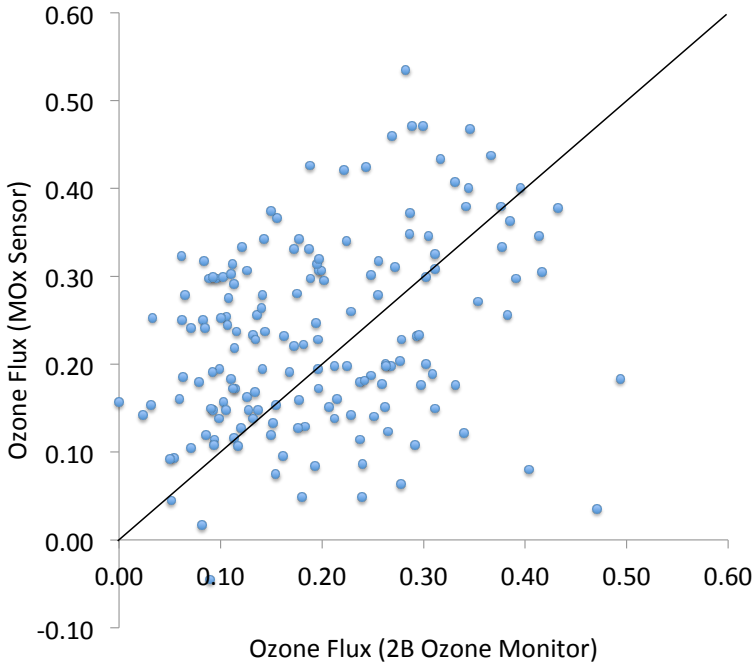

Figure 5.6: The plot above compares flux rates measured by Chamber 2, using the 2B ozone monitor and MO_x sensor

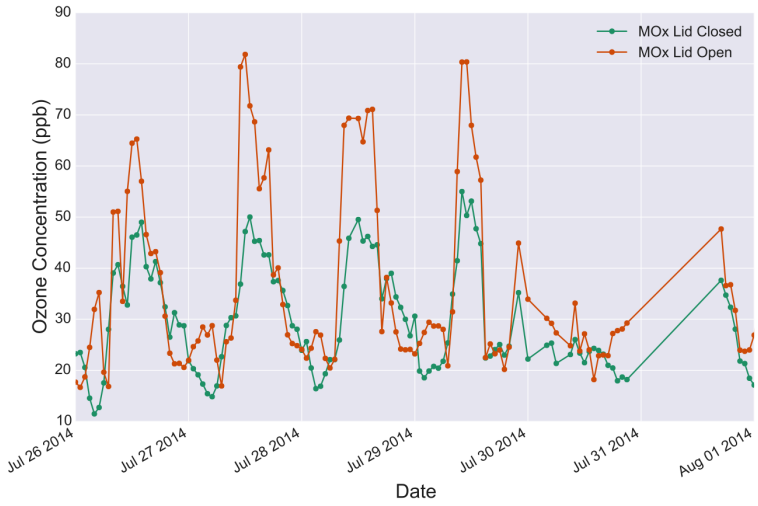

Figure 5.7: The plot above shows ozone concentrations measured by Chamber 1 using the MO_x ozone sensors at the Erie Airport between July 26th and August 1st, 2014.

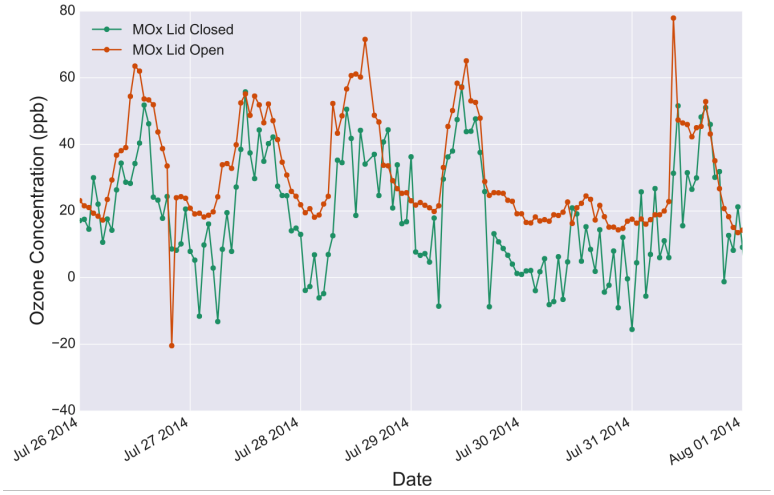

Figure 5.8: The plot above shows ozone concentrations measured by Chamber 3 (at the Fredrick High School) using the MO_x ozone sensors between July 26th and August 1st, 2014.

Chapter 6

Conclusions

In order to better understand the behavior of atmospheric ozone, from ambient concentrations to atmospheric deposition, it is crucial to acquire more measurements. This can be achieved through the use of low-cost instrumentation, including metal-oxide ozone sensors. The first portion of this work was centered around developing affordable dynamic flux chambers, which were demonstrated to be capable of accurately measuring ozone flux to grassland vegetation when paired with 2B Ozone Monitors. The next part of this work involved completing a field study using these flux chambers, with the goal of incorporating low-cost metal-oxide sensors to measure flux. When collocation calibrations proved to be difficult, the focus shifted to improving sensor quantification models.

During the first part of this work, the flux chambers we developed were collocated with an eddy covariance system in the Duke Forest in Chapel Hill, NC, and ozone deposition onto grassland ecosystems was measured using both methods. Measurements from the two methods matched very well (4–10 % difference) when the LAI inside the chambers was representative of the average LAI in the field. This 4–10 % difference is within the uncertainty of the eddy covariance measurements, and the flux chambers can be considered an accurate ozone-flux measurement system when combined with 2B ozone monitors.

The next step was to use these chambers measure spatial variability in ozone deposition using low-cost metal-oxide sensors with the dynamic flux chambers. Collocation calibrations of the sensors proved to be very difficult because the ozone the sensors were exposed to abrupt changes in

temperature and relative humidity every time the chamber lid opened and closed. Because of this challenge, we deemed it necessary to improve the models that we use to calibrate our sensors. The previous calibration models yielded particularly poor results at high ozone concentrations, even for ambient measurements, so the next step was improve the performance of the models in the ambient environment.

The first step in improving the models was to create a large number of features from the original data, which leveraged time-series data, as well as feature interactions between the MO_x ozone sensor, temperature, and relative humidity. Next, we extracted the best features via forward stepwise selection. Using these new features with a linear regression model led to a 42% reduction in the underprediction of ozone at ozone concentrations > 50 ppb. The Lasso regression, which is a linear regression with an L1 regularization, outperformed linear regression with forward selection when learning curves indicated high variance.

These relatively simple methods outperformed the more complex ensemble methods, Random Forests and Support Vector Machines, in this work. The lackluster performance of Random Forests was probably due to the fact that the algorithm could not be customized to emphasize high ozone concentrations. Support Vector Machines have the same problem. Also, SVMs do not reduce the number of features in a fit, which can lead to overfitting. While sophisticated algorithms can be very powerful, they lack the flexibility and interpretability of their simpler predecessors, which exhibited superior performance in this work.

While model revisions led to greatly improved sensor performance in general, when ambient ozone concentrations were much higher than during collocation calibrations, the underpredictions of ozone concentration were more pronounced. We recommend that future ozone studies combine collocation calibrations, which represent real-world conditions, with laboratory calibrations that include exposure to the highest ozone concentrations that could be encountered in the field.

After developing more accurate models to calibrate the ozone sensors, we applied them to the flux chamber collocation data. The new model resulted in more improved results for ambient concentrations, but because of the rapid changes in temperature and relative humidity in the

flux chambers, results for flux measurements were inaccurate. The development of two separate calibration models– one for the last eight minutes before the chamber closed, and one for the last three minutes the chamber was closed before reopening, reduced this error. This improved results, and concentrations measured with the MO_x sensors followed the same trends, and had similar concentrations to those measured by the 2B Ozone Monitor. While the results were improved, the the correlation between the concentrations measured by the two devices was still low, and the hourly measurements acquired using the flux chambers and the MO_x sensors cannot be considered reliable. The MOx sensors performed much better for time-averaged measurements. For the 15-day period studied, the mean flux rate measured by the MO_x sensors was only 21% greater than the flux measured by the 2B ozone monitor. Therefore, the flux chambers with the MO_x sensors can accurately be used to measure weekly-average ozone flux.

In summary, this work resulted in low-cost flux chambers that accurately measure hourly ozone flux rates when paired with 2B ozone monitors, and weekly ozone flux rates when paired with MO_x sensors. The cost of the chambers in combination with both 2B ozone monitors ($7000) and MO_x sensors ($2000) is much lower than the cost of eddy covariance. Additionally, a complete overhaul of the models used to calibrate metal-oxide ozone sensors resulted in a 42% improvement in the prediction of high ambient ozone values. The modeling algorithms developed in this work can be applied to all of the sensors used by our group, which will improve results for a number of studies.

Bibliography

Aeschlimann, U., Nösberger, J., Edwards, P. J., Schneider, M. K., Richter, M., and Blum, H. (2005). Responses of net ecosystem CO_2 exchange in managed grassland to long-term CO_2 enrichment, N fertilization and plant species. Plant, Cell & Environment, 28(7):823–833.

Almand-Hunter, B., Walker, J., Masson, N., Hafford, L., and Hannigan, M. (2015). Development and validation of inexpensive, automated, dynamic flux chambers. Atmospheric Measurement Techniques, 8(1):267–280.

Altimir, N., Vesala, T., Keronen, P., Kulmala, M., and Hari, P. (2002). Methodology for direct field measurements of ozone flux to foliage with shoot chambers. Atmospheric Environment, 36(1):19–29.

Aneja, V. P., Robarge, W. P., and Holbrook, B. D. (1995). Measurements of nitric oxide flux from an upper coastal plain, north carolina agricultural soil. Atmospheric Environment, 29(21):3037–3042.

Aoki, P. M., Honicky, R., Mainwaring, A., Myers, C., Paulos, E., Subramanian, S., and Woodruff, A. (2008). Common sense: Mobile environmental sensing platforms to support community action and citizen science.

Ashmore, M. (2005). Assessing the future global impacts of ozone on vegetation. Plant, Cell & Environment, 28(8):949–964.

Baldocchi, D. D., Hincks, B. B., and Meyers, T. P. (1988). Measuring biosphere-atmosphere exchanges of biologically related gases with micrometeorological methods. Ecology, 69:1331–1340.

Barsan, N. and Weimar, U. (2001). Conduction model of metal oxide gas sensors. Journal of Electroceramics, 7(3):143–167.

Benedict, K. B., Day, D., Schwandner, F. M., Kreidenweis, S. M., Schichtel, B., Malm, W. C., and Collett Jr, J. L. (2013). Observations of atmospheric reactive nitrogen species in rocky mountain national park and across northern colorado. Atmospheric Environment, 64:66–76.

Breiman, L. (2001). Random forests. Machine learning, 45(1):5–32.

Breuninger, C., Meixner, F., and Kesselmeier, J. (2012a). Field investigations of nitrogen dioxide NO_2 exchange between plants and the atmosphere. Atmospheric Chemistry and Physics Discussions, 12(7):18163–18206.

Breuninger, C., Oswald, R., Kesselmeier, J., and Meixner, F. (2012b). The dynamic chamber method: trace gas exchange fluxes (NO, NO_2, O3) between plants and the atmosphere in the laboratory and in the field. Atmospheric Measurement Techniques, 5(5):955–989.

Brook, J. R., Zhang, L., Di-Giovanni, F., and Padro, J. (1999). Description and evaluation of a model of deposition velocities for routine estimates of air pollutant dry deposition over north america.: Part i: model development. Atmospheric Environment, 33(30):5037–5051.

Burkart, S., Manderscheid, R., and Weigel, H.-J. (2007). Design and performance of a portable gas exchange chamber system for CO_2 and H_2O flux measurements in crop canopies. Environmental and Experimental Botany, 61(1):25 – 34.

Butterbach-Bahl, K., Gasche, R., Breuer, L., and Papen, H. (1997). Fluxes of no and n2o from temperate forest soils: impact of forest type, n deposition and of liming on the no and n2o emissions. Nutrient Cycling in Agroecosystems, 48(1-2):79–90.

Chamberlain, A. and Chadwick, R. C. (1953). Deposition of airborne radioiodine vapour. Nucleonics, 11:22–25.

Clarke, J., Edgerton, E., and Martin, B. (1997). Dry deposition calculations for the clean air status and trends network. Atmospheric Environment, 31(21):3667–3678.

De Vito, S., Piga, M., Martinotto, L., and Di Francia, G. (2009). Co, no 2 and no x urban pollution monitoring with on-field calibrated electronic nose by automatic bayesian regularization. Sensors and Actuators B: Chemical, 143(1):182–191.

Delpha, C., Siadat, M., and Lumbreras, M. (1999). Humidity dependence of a tgs gas sensor array in an air-conditioned atmosphere. Sensors and Actuators B: Chemical, 59(2):255–259.

Di Natale, C., Martinelli, E., and DAmico, A. (2002). Counteraction of environmental disturbances of electronic nose data by independent component analysis. Sensors and Actuators B: Chemical, 82(2):158–165.

Dijk, S. M. and Duyzer, J. H. (1999). Nitric oxide emissions from forest soils. Journal of Geophysical Research: Atmospheres (1984–2012), 104(D13):15955–15961.

Emberson, L., Ashmore, M., Cambridge, H., Simpson, D., and Tuovinen, J.-P. (2000). Modelling stomatal ozone flux across europe. Environmental Pollution, 109(3):403–413.

EPA, U. (2010). Clean air status and trends network 2010 annual report. Technical report.

EPA, U. S. (2011). Policy assessment for the review of the secondary national ambient air quality standards for oxides of nitrogen and oxides of sulfur. Technical report, United States Environmental Protection Agency, Research Triangle Park, NC.

EPA, U. S. (2013). Integrated science assessment of ozone and related photochemical oxidants (final report) epa/600/r-10/076f. Technical report, United States Environmental Protection Agency, Washington, DC.

Fangmeier, A., Hadwiger-Fangmeier, A., Van der Eerden, L., and Jäger, H.-J. (1994). Effects of atmospheric ammonia on vegetationa review. Environmental pollution, 86(1):43–82.

Fenn, M. E., Poth, M. A., Aber, J. D., Baron, J. S., Bormann, B. T., Johnson, D. W., Lemly, A. D., McNulty, S. G., Ryan, D. F., and Stottlemyer, R. (1998). Nitrogen excess in north american ecosystems: Predisposing factors, ecosystem responses, and management strategies. Ecological Applications, 8:706–733.

Finkelstein, P. and Sims, P. (2001). Sampling error in eddy correlation flux measurements. Journal of Geophysical Research, 106:3503–3509.

Flechard, C., Nemitz, E., Smith, R., Fowler, D., Vermeulen, A., Bleeker, A., Erisman, J., Simpson, D., Zhang, L., Tang, Y., et al. (2011). Dry deposition of reactive nitrogen to european ecosystems: a comparison of inferential models across the nitroeurope network. Atmospheric Chemistry and Physics, 11(6):2703–2728.

Fluxnet (2015). Duke forest open field. http://fluxnet.ornl.gov/site/867.

Foken, T. and Wichura, B. (1996). Tools for the quality assessment of surface-based flux measurements. Agricultural and Forest Meteorology, 78:83–105.

Friedman, J., Hastie, T., and Tibshirani, R. (2001). The elements of statistical learning, volume 1. Springer series in statistics Springer, Berlin.

Garcia, R. L., Norman, J. M., and McDermitt, D. K. (1990). Measurements of canopy gas exchange using an open chamber system. Remote Sensing Reviews, 5(1):141–162.

Gareth, J., Witten, D., Hastie, T., and Tibshirani, R. (2013). An introduction to statistical learning. Springer.

Gessler, A., Rienks, M., and Rennenberg, H. (2000). NH_3 and NO_2 fluxes between beech trees and the atmosphere–correlation with climatic and physiological parameters. New Phytologist, 147(3):539–560.

Gillis, A. and Miller, D. R. (2000). Some potential errors in the measurement of mercury gas exchange at the soil surface using a dynamic flux chamber. Science of the total environment, 260(1):181–189.

Guesten, H., Heinrich, G., Schmidt, R., and Schurath, U. (1992). Tools for the quality assessment of surface-based flux measurements. J. Atmos. Chem, 14:73–84.

Gut, A., Neftel, A., Staffelbach, T., Riedo, M., and Lehmann, B. (1999). Nitric oxide flux from soil during the growing season of wheat by continuous measurements of the no soil–atmosphere concentration gradient: A process study. Plant and soil, 216(1-2):165–180.

Gut, A., Van Dijk, S., Scheibe, M., Rummel, U., Welling, M., Ammann, C., Meixner, F., Kirkman, G., Andreae, M., and Lehmann, B. (2002). No emission from an amazonian rain forest soil: Continuous measurements of no flux and soil concentration. Journal of Geophysical Research: Atmospheres (1984–2012), 107(D20):LBA–24.

Hasenfratz, D., Saukh, O., Sturzenegger, S., and Thiele, L. (2012). Participatory air pollution monitoring using smartphones. Mobile Sensing.

Hoerl, A. (1962). Application of ridge analysis to regression problems. Chemical Engineering Progress, 58(3):54–59.

Horst, T. and Weil, J. (1994). How far is far enough?: The fetch requirements for micrometeorological measurement of surface fluxes. Journal of Atmospheric and Oceanic Technology, 11(4):1018–1025.

Horváth, L., Führer, E., and Lajtha, K. (2006). Nitric oxide and nitrous oxide emission from hungarian forest soils; linked with atmospheric N-deposition. Atmospheric Environment, 40(40):7786–7795.

Institute, S. (2003). Version 9.3 system help.

Jones, E., Oliphant, T., Peterson, P., et al. (2001–). SciPy: Open source scientific tools for Python.

Kaimal, J. and J.Finnigan (1994). Atmospheric Boundary-Layer Flows: Their Structure and Measurement. Oxford University Press.

Kamionka, M., Breuil, P., and Pijolat, C. (2006). Calibration of a multivariate gas sensing device for atmospheric pollution measurement. Sensors and Actuators B: Chemical, 118(1):323–327.

Kaplan, W., Wofsy, S., Keller, M., and Da Costa, J. M. (1988). Emission of no and deposition of o3 in a tropical forest system. Journal of Geophysical Research: Atmospheres (1984–2012), 93(D2):1389–1395.

Kirkman, G., Gut, A., Ammann, C., Gatti, L., Cordova, A., Moura, M., Andreae, M., and Meixner, F. (2002). Surface exchange of nitric oxide, nitrogen dioxide, and ozone at a cattle pasture in rondonia, brazil. Journal of Geophysical Research: Atmospheres (1984–2012), 107(D20):LBA–51.

Kitzler, B., Zechmeister-Boltenstern, S., Holtermann, C., Skiba, U., and Butterbach-Bahl, K. (2006). Nitrogen oxides emission from two beech forests subjected to different nitrogen loads. Biogeosciences, 3(3):293–310.

Laville, P., Lehuger, S., Loubet, B., Chaumartin, F., and Cellier, P. (2011). Effect of management, climate and soil conditions on N_2O and NO emissions from an arable crop rotation using high temporal resolution measurements. Agricultural and forest meteorology, 151(2):228–240.

Li, Y., Aneja, V. P., Arya, S., Rickman, J., Brittig, J., Roelle, P., and Kim, D. (1999). Nitric oxide emission from intensively managed agricultural soil in north carolina. Journal of Geophysical Research: Atmospheres (1984–2012), 104(D21):26115–26123.

Lippmann, M. (1989). Health effects of ozone a critical review. Japca, 39(5):672–695.

Machon, A., Horváth, L., Weidinger, T., Grosz, B., Pintér, K., Tuba, Z., and Führer, E. (2010). Estimation of net nitrogen flux between the atmosphere and a semi-natural grassland ecosystem in hungary. European journal of soil science, 61(5):631–639.

Maljanen, M., Martikkala, M., Koponen, H. T., Virkajärvi, P., and Martikainen, P. J. (2007). Fluxes of nitrous oxide and nitric oxide from experimental excreta patches in boreal agricultural soil. Soil Biology and Biochemistry, 39(4):914–920.

Marco, S. (2014). The need for external validation in machine olfaction: emphasis on health-related applications. Analytical and bioanalytical chemistry, 406(16):3941–3956.

Masson, N. (2015). Upod: An open-source platform for air quality monitoring. http://mobilesensingtechnology.com/.

Masson, N., Piedrahita, R., and Hannigan, M. (2015). Approach for quantification of metal oxide type semiconductor gas sensors used for ambient air quality monitoring. Sensors and Actuators B: Chemical, 208:339–345.

Mead, M., Popoola, O., Stewart, G., Landshoff, P., Calleja, M., Hayes, M., Baldovi, J., McLeod, M., Hodgson, T., Dicks, J., et al. (2013). The use of electrochemical sensors for monitoring urban air quality in low-cost, high-density networks. Atmospheric Environment, 70:186–203.

Meixner, F., Fickinger, T., Marufu, L., Serca, D., Nathaus, F., Makina, E., Mukurumbira, L., and Andreae, M. (1997). Preliminary results on nitric oxide emission from a southern african savanna ecosystem. Nutrient Cycling in Agroecosystems, 48(1-2):123–138.

Moseley, P. (1997). Solid state gas sensors. Measurement Science and technology, 8(3):223–237.

Muller, J., Percival, C., Gallagher, M., Fowler, D., Coyle, M., and Nemitz, E. (2010). Sources of uncertainty in eddy covariance ozone flux measurements made by dry chemiluminescence fast response analysers. Atmos. Meas. Tech., 3:163176.

Musselman, R. C., Lefohn, A. S., Massman, W. J., and Heath, R. L. (2006). A critical review and analysis of the use of exposure-and flux-based ozone indices for predicting vegetation effects. Atmospheric Environment, 40(10):1869–1888.

Norman, J., Kucharik, C., Gower, S., Baldocchi, D., Crill, P., Rayment, M., Savage, K., and Striegl, R. (1997). A comparison of six methods for measuring soil-surface carbon dioxide fluxes. Journal of Geophysical Research: Atmospheres (1984–2012), 102(D24):28771–28777.

Pape, L., Ammann, C., Nyfeler-Brunner, A., Spirig, C., Hens, K., and Meixner, F. (2008). An automated dynamic chamber system for surface exchange measurement of non- reactive and reactive trace gases of grassland ecosystems. Biogeosciences Discuss, 5:3157–3219.

Parrish, D. D., Williams, E. J., Fahey, D. W., Liu, S. C., and Fehsenfeld, F. C. (1987). Measurement of nitrogen oxide fluxes from soils: Intercomparison of enclosure and gradient measurement techniques. Journal of Geophysical Research: Atmospheres, 92(D2):2165–2171.

Pedregosa, F., Varoquaux, G., Gramfort, A., Michel, V., Thirion, B., Grisel, O., Blondel, M., Prettenhofer, P., Weiss, R., Dubourg, V., Vanderplas, J., Passos, A., Cournapeau, D., Brucher, M., Perrot, M., and Duchesnay, E. (2011). Scikit-learn: Machine learning in Python. Journal of Machine Learning Research, 12:2825–2830.

Piedrahita, R., Xiang, Y., Masson, N., Ortega, J., Collier, A., Jiang, Y., Li, K., Dick, R., Lv, Q., Hannigan, M., et al. (2014a). The next generation of low-cost personal air quality sensors for quantitative exposure monitoring. Atmospheric Measurement Techniques, 7(10):3325–3336.

Piedrahita, R., Xiang, Y., Masson, N., Ortega, J., Collier, A., Jiang, Y., Li, K., Dick, R., Lv, Q., Hannigan, M., and Shang, L. (2014b). The next generation of low-cost personal air quality sensors for quantitative exposure monitoring. Atmos. Meas. Tech. Discuss., 7:2425–2457.

Pilegaard, K. (2001). Air–soil exchange of NO, NO_2 and O_3 in forests. Water, Air and Soil Pollution: Focus, 1(5-6):79–88.

Pilegaard, K., Hummelshøj, P., and Jensen, N. (1999). Nitric oxide emission from a norway spruce forest floor. Journal of Geophysical Research: Atmospheres (1984–2012), 104(D3):3433–3445.

Remde, A., Ludwig, J., Meixner, F. X., and Conrad, R. (1993). A study to explain the emission of nitric oxide from a marsh soil. Journal of Atmospheric Chemistry, 17(3):249–275.

Roelle, P., Aneja, V. P., O'connor, J., Robarge, W., Kim, D.-S., and Levine, J. S. (1999). Measurement of nitrogen oxide emissions from an agricultural soil with a dynamic chamber system. Journal of Geophysical Research: Atmospheres (1984–2012), 104(D1):1609–1619.

Roelle, P. A., Aneja, V. P., Gay, B., Geron, C., and Pierce, T. (2001). Biogenic nitric oxide emissions from cropland soils. Atmospheric Environment, 35(1):115–124.

Romain, A.-C. and Nicolas, J. (2010). Long term stability of metal oxide-based gas sensors for e-nose environmental applications: An overview. Sensors and Actuators B: Chemical, 146(2):502–506.

Romain, A.-C., Nicolas, J., and Andre, P. (1997). In situ measurement of olfactive pollution with inorganic semiconductors: Limitations due to humidity and temperature influence. In Seminars in Food analysis, volume 2, pages 283–296.

Schwede, D., Zhang, L., Vet, R., and Lear, G. (2011). An intercomparison of the deposition models used in the castnet and capmon networks. Atmospheric Environment, 45(6):1337–1346.

Seinfeld, J. H. and Pandis, S. N. (2006). Atmospheric Chemistry and Physics. Wiley, 2 edition.

Shum, L. V., Rajalakshmi, P., Afonja, A., McPhillips, G., Binions, R., Cheng, L., and Hailes, S. (2011). On the development of a sensor module for real-time pollution monitoring. In Information Science and Applications (ICISA), 2011 International Conference on, pages 1–9. IEEE.

Skiba, U., Smith, K., et al. (1993). Nitrification and denitrification as sources of nitric oxide and nitrous oxide in a sandy loam soil. Soil Biology and Biochemistry, 25(11):1527–1536.

Slemr, F. and Seiler, W. (1984). Field measurements of NO and NO_2 emissions from fertilized and unfertilized soils. Journal of Atmospheric Chemistry, 2(1):1–24.

Smola, A. J. and Schölkopf, B. (2004). A tutorial on support vector regression. Statistics and computing, 14(3):199–222.

Sohn, J. H., Atzeni, M., Zeller, L., and Pioggia, G. (2008). Characterisation of humidity dependence of a metal oxide semiconductor sensor array using partial least squares. Sensors and Actuators B: Chemical, 131(1):230–235.

Sparks, J. P., Monson, R. K., Sparks, K. L., and Lerdau, M. (2001). Leaf uptake of nitrogen dioxide(NO_2) in a tropical wet forest: implications for tropospheric chemistry. Oecologia, 127(2):214–221.

Stella, P., Loubet, B., Laville, P., Lamaud, E., Cazaunau, M., Laufs, S., Bernard, F., Grosselin, B., Mascher, N., Kurtenbach, R., et al. (2012). Comparison of methods for the determination of no-o 3-no 2 fluxes and chemical interactions over a bare soil. Atmospheric Measurement Techniques, 5(6):1241–1257.

Sundgren, H., Winquist, F., Lukkari, I., and Lundstrom, I. (1991). Artificial neural networks and gas sensor arrays: quantification of individual components in a gas mixture. Measurement Science and Technology, 2(5):464.

Tibshirani, R. (1996). Regression shrinkage and selection via the lasso. Journal of the Royal Statistical Society. Series B (Methodological), pages 267–288.

Tong, D. Q. and Mauzerall, D. L. (2006). Spatial variability of summertime tropospheric ozone over the continental united states: Implications of an evaluation of the cmaq model. Atmospheric Environment, 40(17):3041–3056.

Turner, D. (1969). Workbook of atmoshpheric diffusion estimates.

Turnipseed, A., Burns, S., Moore, D., Hu, J., Guenther, A., and Monson, R. (2009). Controls over ozone deposition to a high elevation subalpine forest. Agricultural and Forest Meteorology, 149:1447–1459.

Unsworth, M., Heagle, A., and Heck, W. (1984). Gas exchange in open-top field chambers-I. Measurement and analysis of atmospheric resistances to gas exchange. Atmospheric Environment, 18(2):373–380.

Vapnik, V., Golowich, S. E., and Smola, A. (1996). Support vector method for function approximation, regression estimation, and signal processing. In Advances in Neural Information Processing Systems 9. Citeseer.

Vergara, A., Fonollosa, J., Mahiques, J., Trincavelli, M., Rulkov, N., and Huerta, R. (2013). On the performance of gas sensor arrays in open sampling systems using inhibitory support vector machines. Sensors and Actuators B: Chemical, 185:462–477.

Wesely, M. (1989). Parameterization of surface resistances to gaseous dry deposition in regional-scale numerical models. Atmospheric Environment, 23:1293–1304.

Wesely, M. and Hicks, B. B. (2000). A review of the current status of knowledge on dry deposition. Atmospheric Environment, 34:2261–2282.

Williams, D. E., Salmond, J., Yung, Y. F., Akaji, J., Wright, B., Wilson, J., Henshaw, G. S., Wells, D. B., Ding, G., Wagner, J., et al. (2009). Development of low-cost ozone and nitrogen dioxide measurement instruments suitable for use in an air quality monitoring network. In Sensors, 2009 IEEE, pages 1099–1104. IEEE.

Williams, E. and Davidson, E. (1993). An intercomparison of two chamber methods for the determination of emission of nitric oxide from soil. Atmospheric Environment. Part A. General Topics, 27(14):2107–2113.

Williams, M. and Tonnessen, K. (2000). Critical loads for inorganic nitrogen deposition in the colorado front range, usa. Ecological Applications, 10:1648–1665.

Wolfrum, E. J., Meglen, R. M., Peterson, D., and Sluiter, J. (2006). Metal oxide sensor arrays for the detection, differentiation, and quantification of volatile organic compounds at sub-parts-per-million concentration levels. Sensors and Actuators B: Chemical, 115(1):322–329.

Wu, W., Zhang, G., and Kai, P. (2012). Ammonia and methane emissions from two naturally ventilated dairy cattle buildings and the influence of climatic factors on ammonia emissions. Atmospheric Environment, 61:232–243.

Wu, Z., Wang, X., Chen, F., Turnipseed, A. A., Guenther, A. B., Niyogi, D., Charusombat, U., Xia, B., William Munger, J., and Alapaty, K. (2011). Evaluating the calculated dry deposition velocities of reactive nitrogen oxides and ozone from two community models over a temperate deciduous forest. Atmospheric Environment, 45(16):2663–2674.

Yamulki, S., Goulding, K., Webster, C., and Harrison, R. M. (1995). Studies on NO and N_2O fluxes from a wheat field. Atmospheric Environment, 29(14):1627–1635.

Zahn, A., Weppner, J., Widmann, H., Schlote-Holubek, K., Burger, B., H., T. K., and Franke (2012). A fast and precise chemiluminescence ozone detector for eddy flux and airborne application. Atmos. Meas. Tech., 5:363–375.

Zampolli, S., Elmi, I., Ahmed, F., Passini, M., Cardinali, G., Nicoletti, S., and Dori, L. (2004). An electronic nose based on solid state sensor arrays for low-cost indoor air quality monitoring applications. Sensors and Actuators B: Chemical, 101(1):39–46.

Zhang, L., Moran, M., and Brook, J. (2001). A comparison of models to estimate in-canopy photosynthetically active radiation and their influence on canopy stomatal resistance. Atmospheric Environment, 35:4463–4470.

Zhang, L., Moran, M. D., Makar, P. A., Brook, J. R., and Gong, S. (2002). Modelling gaseous dry deposition in aurams: a unified regional air-quality modelling system. Atmospheric Environment, 36(3):537–560.

Zhang, L., Vet, R., and Brook, J. (2003). A revised parameterization for gaseous dry deposition in air-quality models. Atmospheric Chemistry and Physics, 3:2067–2082.